

# THESIS

## **Development of Adaptive Compensation of Heavy Beam Loading for J-PARC LINAC**

**J-PARC リニアックにおける自動補正のビーム  
負荷補償の開発**

LI SONG

DOCTOR OF PHILOSOPHY

Department of Accelerator Science

School of High Energy Accelerator Science

SOKENDAI (The Graduate University for Advanced Studies)

2019

Supervisor:	Prof. Zhigao Fang
Reviewer:	Prof. Toshihiro Matsumoto
	Prof. Tetsuya Kobayashi
	Prof. Kenta Futatsukawa
	Prof. Feng Qiu
	Prof. Yasuhiro Kondo
Day of Submission:	8 <sup>th</sup> of June 2019

*For my family  
and all the people who helped my Ph.D work.*

# Abstract

Japan Proton Accelerator Research Complex (J-PARC) consists of a 400 MeV linear accelerator (LINAC), a 3 GeV rapid cycling synchrotron (RCS) and a 50 GeV main ring (MR). The LINAC is a 248 m normal conducting linear accelerator, which accelerates the negative hydrogen ions (H-) to up to 400 MeV at a repetition rate of 25 Hz with a pulse beam width of 500  $\mu$ s. From 2018, the peak beam current of the LINAC was increased from 40 to 50 mA. According to the J-PARC accelerator technical design report, until now, the goal of J-PARC project in Phase I has already been realized which is to achieve 1 MW beam power at the RCS and 0.75 MW beam power at the MR. And now, one of the targets in phase II is to increase the beam power at the RCS from 1 MW to 1.5 MW. In order to realized it, more than 20% increment is needed for both the beam current and beam pulse length at the LINAC, which will be about 60 mA and 600  $\mu$ s, respectively. Such strong beam current will bring heavy beam loading effect to all the cavities in the LINAC, which will lead to a significant drop of accelerating gradient.

In the current LLRF (Low-Level Radio Frequency) control system, a static feedforward control method was used to compensate for the beam loading effect. Since the beam current has increased to 50 mA, current beam loading compensation method faces significant challenges. In terms of performance, the current stability can barely reach from -0.5% to +1.9% in amplitude and from -0.2° to +1.2° in phase, and this value will deteriorate during the long-term operation. In addition, static feedforward needs people to adjust the compensation amplitude, phase and the delay of trigger signal manually. For the large accelerator like J-PARC LINAC, it is usually need two people to takes 5 ~ 6 hours to finish the adjustment work for all the RF stations.

To solve these problems, an Iterative Learning Control (ILC) method was put forward and developed in the J-PARC LINAC. ILC as a open loop control has been adopted by several research institutes to improve the transient response performance of the LLRF system. Compared to the static feedforward, it not only further enhances the performance of the system, but also automatically completes all compensation processes.

In order to verify the effectiveness of ILC for beam compensation, an ILC simulation module was built in MATLAB. The simulation results show that with the increase of iteration times, the tracking error is monotonic convergence and the deformation caused

by the beam was well compensated. The amplitude peak to peak stability was improved from  $\pm 7.5\%$  to  $\pm 0.25\%$ . And phase peak to peak stability is from  $\pm 2^\circ$  to  $\pm 0.07^\circ$ .

For the sake of not to influence the normal operation of the current system, the ILC controller was developed in the new generation LLRF control prototype system. To build ILC control loop, the PyEpics plug-in was installed in the computer, then the EPICS records in the IOC (Input Output Controller) can be called in real time by the ILC controller, which as a CA (Channel Access) client was developed by Python. The beam loading compensation experiment was conducted in the SDTL01 station. The experiment results show that under 50 mA beam current, the inclusion of ILC controller improved the peak to peak stability to  $\pm 0.28\%$  in amplitude and  $\pm 0.15^\circ$  in phase, which satisfied the requirement of J-PARC LINAC,  $\pm 0.5\%$  in amplitude and  $\pm 0.5^\circ$  in phase. What's more, when the repetition rate of beam is set to 25 Hz, the beam loading compensation process can be completed automatically in several seconds. For the J-PARC LINAC, which has dozens of RF stations that require feedforward compensation, ILC greatly reduces the time consumption and workload, thus improves the work efficiency significantly.

# Content

<b>Abstract .....</b>	<b>I</b>
<b>Content.....</b>	<b>III</b>
<b>1. Introduction.....</b>	<b>1</b>
1.1 Japan Proton Accelerator Research Complex .....	1
1.2 J-PARC LINAC .....	2
1.3 Motivation of The Study .....	4
1.4 Structure of The Thesis.....	8
<b>2. Overview of Beam Loading Compensation Method for the LLRF System .....</b>	<b>10</b>
2.1 European XFEL .....	10
2.2 Los Alamos Neutron Science Center.....	15
2.3 FLASH.....	19
2.4 Comparison of Scheme.....	27
<b>3. The Upgrade of J-PARC LINAC LLRF System .....</b>	<b>28</b>
3.1 Current LLRF System .....	28
3.2 New LLRF System Under Development.....	30
<b>4. Iterative Learning Control.....</b>	<b>34</b>
4.1 ILC Basic Theory .....	35
4.2 ILC Scheme for J-PARC LINAC .....	38
4.3 Norm-Optimal Iterative Learning Control .....	39
<b>5. ILC Simulation Test on MATLAB.....</b>	<b>43</b>
5.1 Design Scheme of ILC Simulation Model .....	43
5.2 Analysis of Simulation Results .....	47
5.3 Conclusion for ILC Simulation.....	54
<b>6. The Hardware and Software Setup for Beam Loading Compensation Experiment .....</b>	<b>56</b>

6.1 Introduction of ILC Based Beam Loading Compensation Experiment .....	56
6.2 Software Setup.....	57
6.3 Hardware Setup.....	60
<b>7. Experimental Results for Beam Loading Compensation .....</b>	<b>62</b>
7.1 Experimental Results in SDTL01 Station .....	62
7.2 Effect of Time Shift of Error .....	69
7.3 Effect of ILC Gain .....	70
7.4 Effect of Moving Average.....	72
<b>8. Mathematical Analysis of LLRF System with an ILC Based Feedforward .....</b>	<b>74</b>
8.1 Mathematical Model of the LLRF System with an ILC based Feedforward Function .....	74
8.2 Stability and Convergence Analysis .....	75
<b>9. Conclusion and Future plan .....</b>	<b>77</b>
9.1 Conclusion .....	77
9.2 Future Plan .....	78
<b>Appendix A .....</b>	<b>79</b>
<b>Abbreviations .....</b>	<b>80</b>
<b>Symbol .....</b>	<b>82</b>
<b>List of Figures.....</b>	<b>83</b>
<b>List of Tables .....</b>	<b>85</b>
<b>Bibliography .....</b>	<b>86</b>
<b>Acknowledgment .....</b>	<b>88</b>
<b>Declaration .....</b>	<b>89</b>





# Chapter 1

## Introduction

This chapter mainly introduce the research background and motivation of this study. In the first two sections, the introduction of Japan Proton Accelerator Research Complex (J-PARC) and J-PARC linear accelerator (LINAC) will be given. Then the motivation of this study will be discussed. In the last section, the structure of this dissertation will be shown.

### 1.1 Japan Proton Accelerator Research Complex

Japan Proton Accelerator Research Complex (J-PARC), which located in Tokai, Ibaraki Prefecture, consists of a 400-MeV proton linear accelerator (LINAC), a 3-GeV Rapid Cycling Synchrotron (RCS), a 30-GeV Main Ring synchrotron (MR) and three experimental facilities that make use of the high-intensity proton beams. An overall arrangement of the J-PARC facilities is shown in the [Fig. 1.1](#).

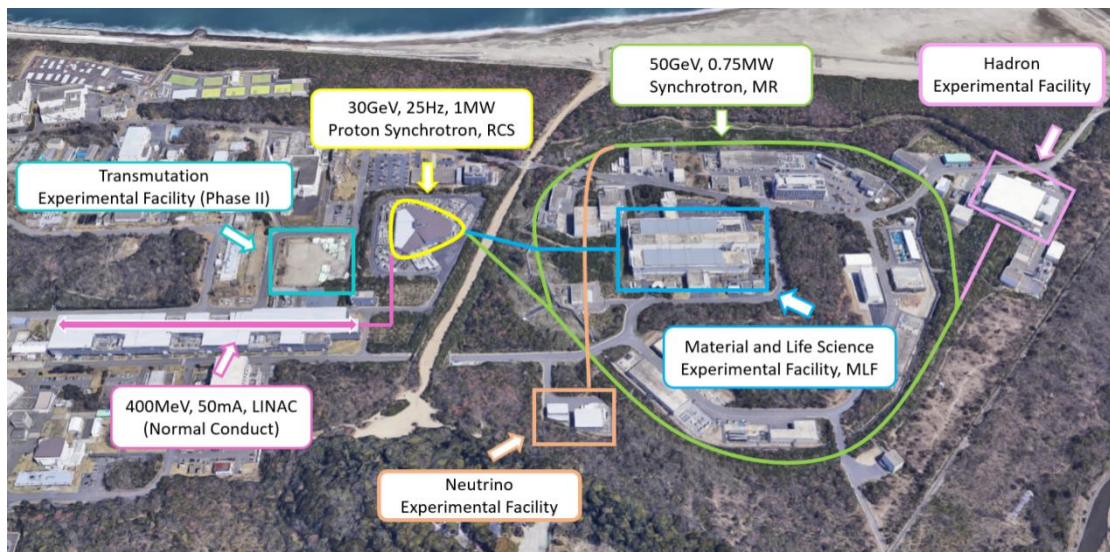


Figure 1.1. A layout of J-PARC facilities.

In normal operation mode, over 90% protons accelerated in the RCS is directed to Materials and Life science experimental Facility (MLF) for neutron and muon experiments. The remaining protons are transported to the Main Ring synchrotron for further acceleration. In Main Ring, there are two beam extraction modes. In Fast Extraction (FX) mode, protons are guided to the pion production target by using superconducting magnetic array. Then the neutrinos that generated in pion decay processes are sent to the super-kamiokande facility for Tokai-to-Kamioka (T2K) experiment by neutrino beam line (NU). In Slow Extraction (SX) mode, high energy proton beam is sent to Hadron Experimental facility (HD) to carry out various nuclear physics experiments [1].

## 1.2 J-PARC LINAC

J-PARC LINAC is a proton linear accelerator which accelerates the negative hydrogen particle to 400 MeV and operates at the repetition rate of 25Hz with a pulse beam width of 500  $\mu$ s. The configuration and main parameters of the J-PARC linac is shown in the Fig. 1.2. The linac consists of an ion source, a 3 MeV Radio Frequency Quadrupole (RFQ), a 50 MeV Drift Tube Linacs (DTL), a 191 MeV Separated Drift Tube Linacs (SDTL) and a 400 MeV Annular Coupled Structure (ACS). There are 64 cavities and 48 RF stations in total, which is mainly divided into two parts. In 324-MHz low  $\beta$  accelerator section, there are 23 RF stations, including RFQ, two bunchers, one chopper, three DTL and 16 SDTL. After coming out of the ion source, the proton beam was accelerated from 50 keV to 191 MeV. Then in 972-MHz high  $\beta$  accelerator section, the energy of beam was further upgraded to 400 MeV by the remaining 25 stations, which consists of 2 bunchers, 21 ACS acceleration cavities and 2 debunchers [2]. Figure 1.3 & 1.4 show the schematic layout of 324-MHz low  $\beta$  accelerator section and 972-MHz high  $\beta$  accelerator section, respectively.

In J-PARC LINAC, each RF station has its own RF power source. In 324-MHz low  $\beta$  accelerator section, 4 solid state amplifiers are used to feed RF power to buncher 1, 2 and two chopper cavities. For RFQ, DTL and SDTL stations, their RF power source are 324-MHz klystrons. At the SDTL stations, RF power from one klystron are fed to two cavities by using a hybrid divider. In 972-MHz high  $\beta$  accelerator section, all the stations use 972-MHz klystron as its RF power source. In addition, all the stations both in low and high  $\beta$  section are equipped with an independent LLRF control system to ensure the stable operation of linac [3]. As far as the LLRF systems currently in use are

concerned, there is no significant difference between the systems used in low  $\beta$  section and those used in high  $\beta$  section.

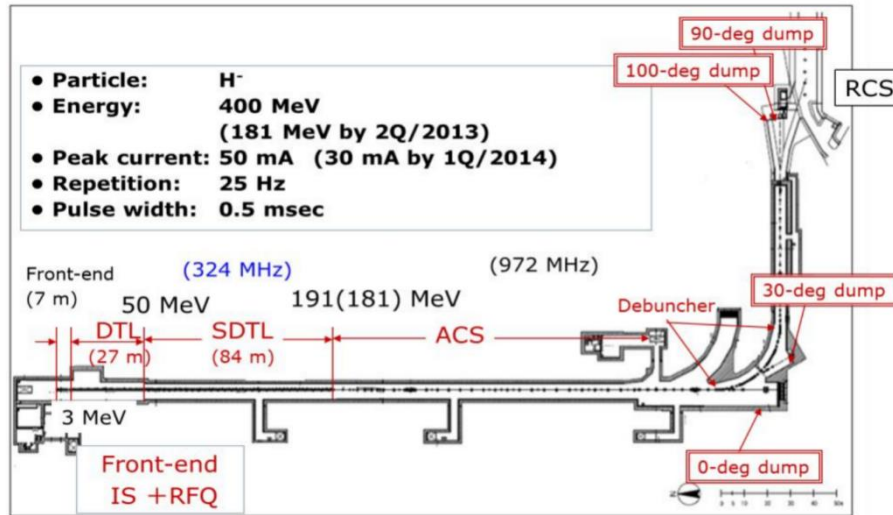


Figure 1.2. Configuration and Main parameter of the J-PARC linac

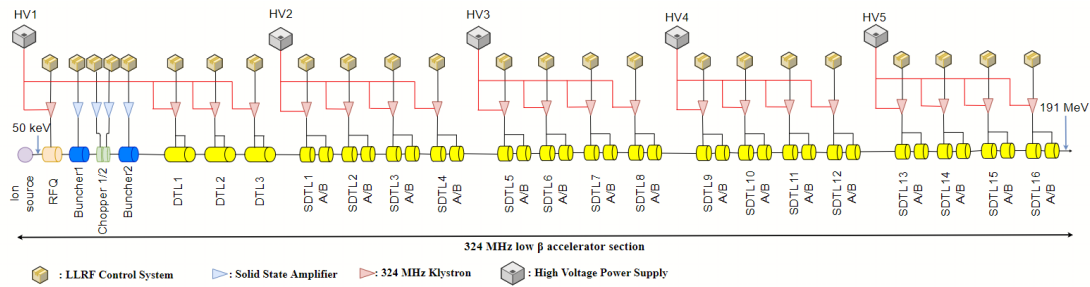


Figure 1.3. Outline of RF Stations and RF Cavities in 324-MHz low  $\beta$  accelerator section.

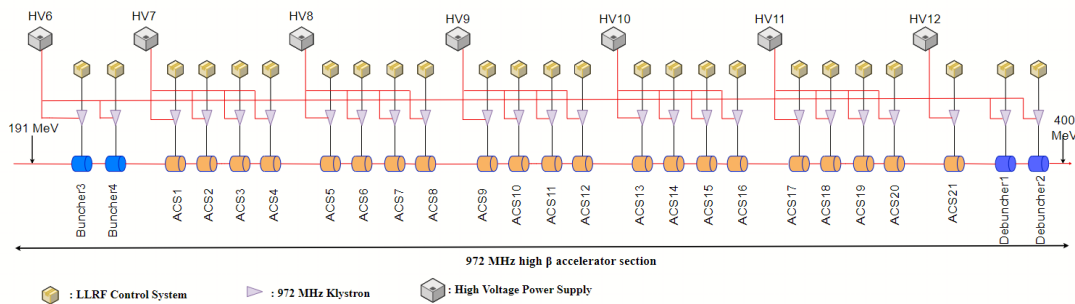


Figure 1.4. Outline of RF Stations and RF Cavities in 972-MHz high  $\beta$  accelerator section.

### 1.3 Motivation of The Study

According to the accelerator technical design report of J-PARC, the goal of phase I is to increase the beam power of RCS to 1 MW and 0.75 MW beam power for MR [4]. In order to realize this nominal performance, the linac beam energy was increased to 400 MeV and beam current was also increased from 30 to 50 mA. Currently, the aim of phase I has already been achieved and the user operation power of MLF runs steadily at 500 kW. For phase II, two further upgrade plans are now in consideration. The first plan is to increase the RCS beam power to 1.5 MW for achieving the goal of 1MW at MLF. Second one is to double the linac repetition rate to 50 Hz for a planned accelerator-driven nuclear waste transmutation system (ADS). In order to realize the 1.5 MW beam power from RCS, both the beam current and the pulse length are planned to increase about 20% at the LINAC [3]. At that time, both the beam current and the beam pulse length will be increased to about 60 mA and 600  $\mu$ s, respectively.

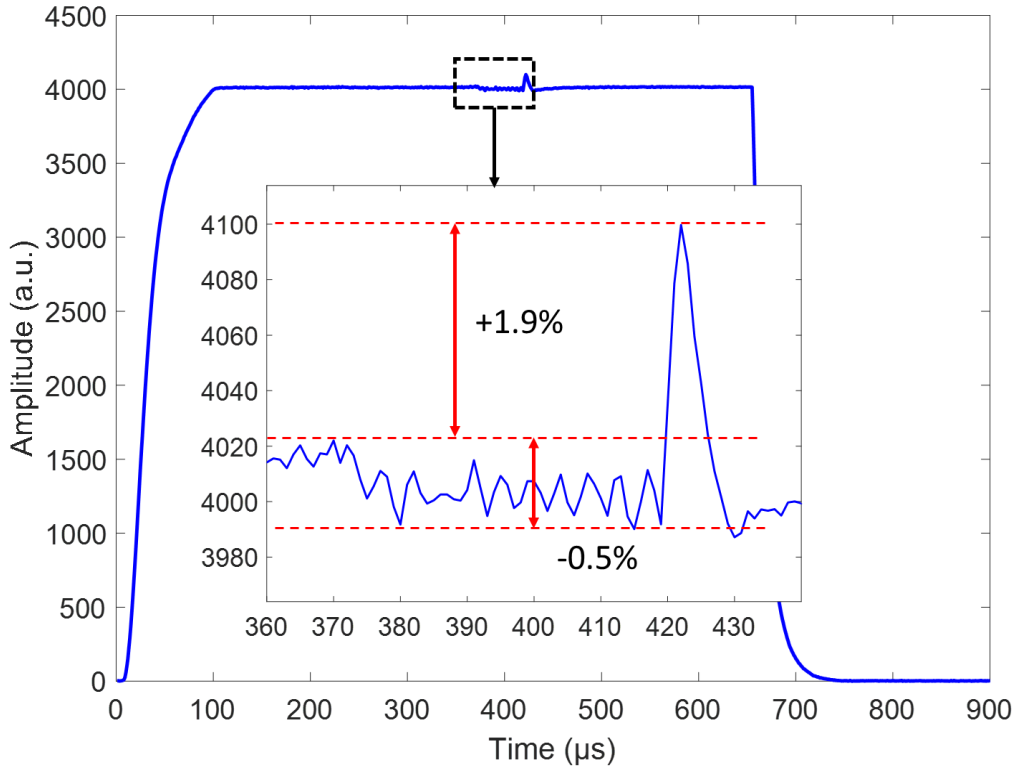


Figure 1.5. ADC amplitude waveform at the flat top in SDTL01 station.

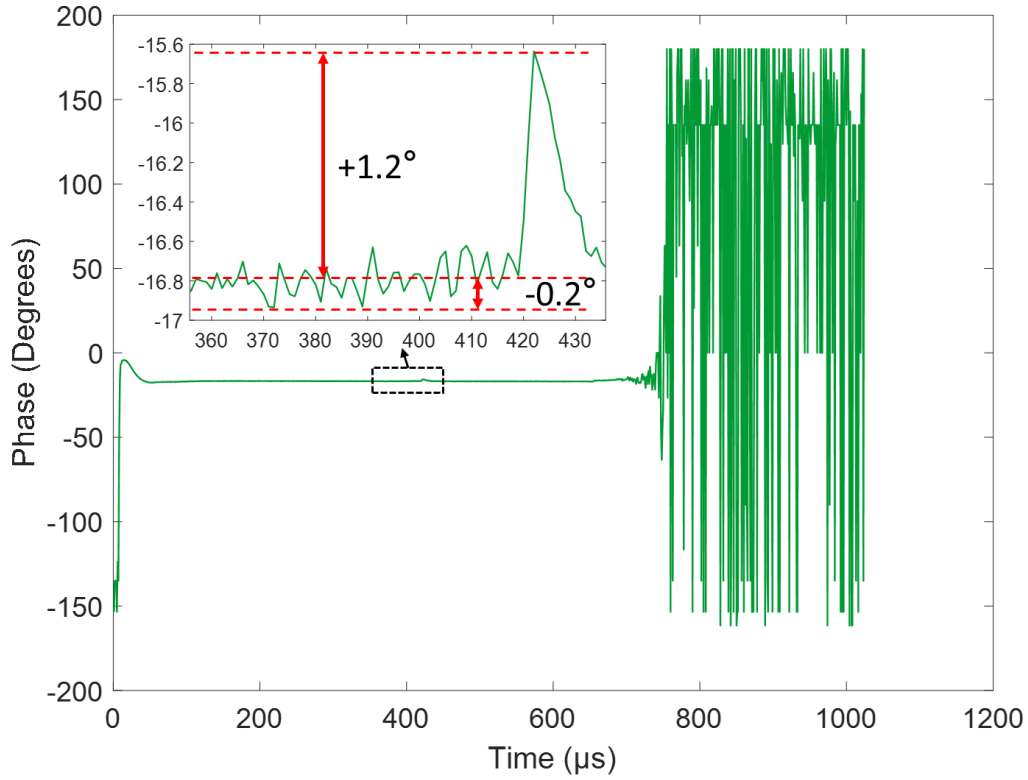


Figure 1.6. ADC phase waveform in SDTL01 station.

The higher beam current will cause a heavier beam loading effect. To compensate such heavy beam loading, both the feedback and the static feed forward control are used. However, due to the difference between the feed forward signal and beam loading current, the static feed forward control is beginning to be difficult to meet compensation requirements. Figure 1.5 shows the amplitude waveform at the flat top of ADC in SDTL 01 station, J-PARC LINAC. The beam current here is 50 mA. Even at the beginning, by adjusting the feedforward manually, we can make the peak to peak stability of ADC amplitude almost equals to  $-0.5\%$  to  $+1.9\%$ . Figure 1.6 shows the phase waveform of ADC in SDTL01 station. The peak to peak stability of phase is from  $-0.2^\circ$  to  $+1.2^\circ$ , which also does not meet the requirement. There are two feedforward compensation mode in the J-PARC LINAC, macro pulse mode and chopper mode, which are shown in the Fig 1.7. In order to keep the output power unchanged, the feedforward amplitude of the chopper mode will be about twice as high as that of the macro pulse mode. For the SDTL station, the compensation method is chopper mode. Figure 1.8 shows the DAC waveform at the SDTL01 station. Due to the effect of feedback control, there is a raise portion at the flat top of DAC waveform. As the input of cavity, the DAC signal include

the information of chopper feedforward which can be found at the raise portion. The amplitude ratio of the raised portion and the flat top is about 45%. The excessive DAC amplitude may exceed the full-scale value, trigger interlock protection. It is better to decrease the amplitude ratio of the raised portion and the flat top.

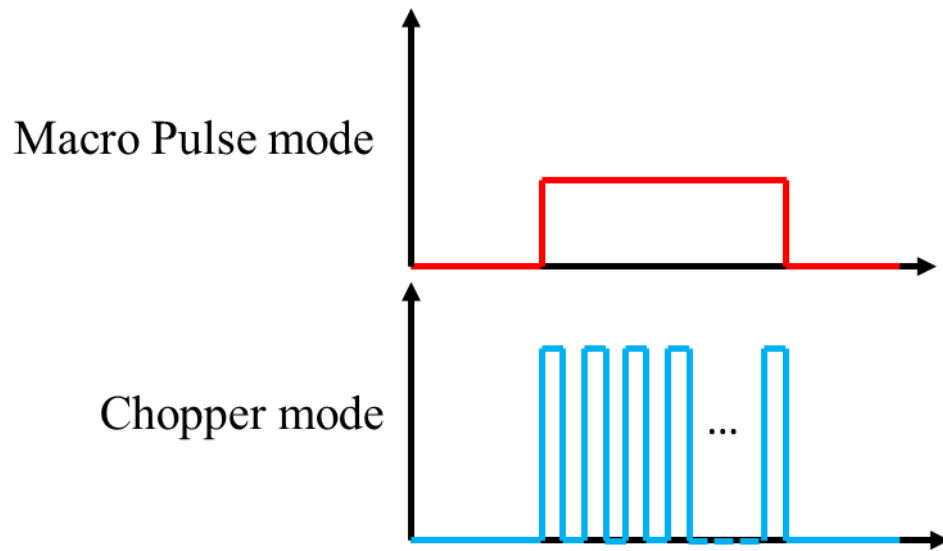


Figure 1.7. Two static feedforward compensation modes in the J-PARC LINAC.

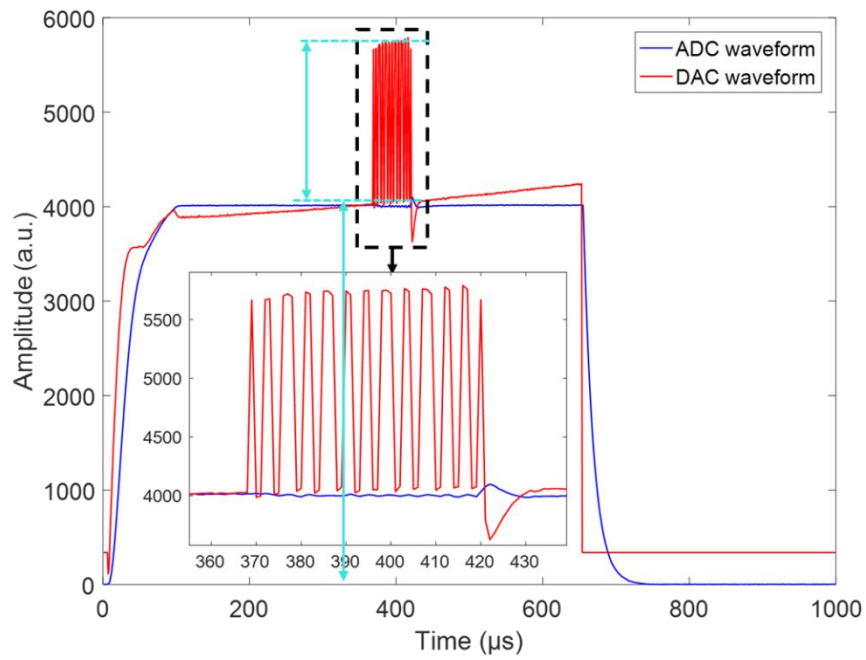


Figure 1.8. DAC amplitude waveform in SDTL01 station.

And in the extreme case which was also observed in the SDTL01 station shown in the Fig. 1.9 & 1.10. During long-term operation of the accelerator, the trigger signal of current beam loading compensation signal was lost, where only feedback works, the peak to peak stability of amplitude became  $\pm 3.62\%$  and phase became  $\pm 1.1^\circ$ . In order to solve this problem, an iterative learning control (ILC) based adaptive feedforward control method was put forward and realized to replace the current normal feedforward control method.

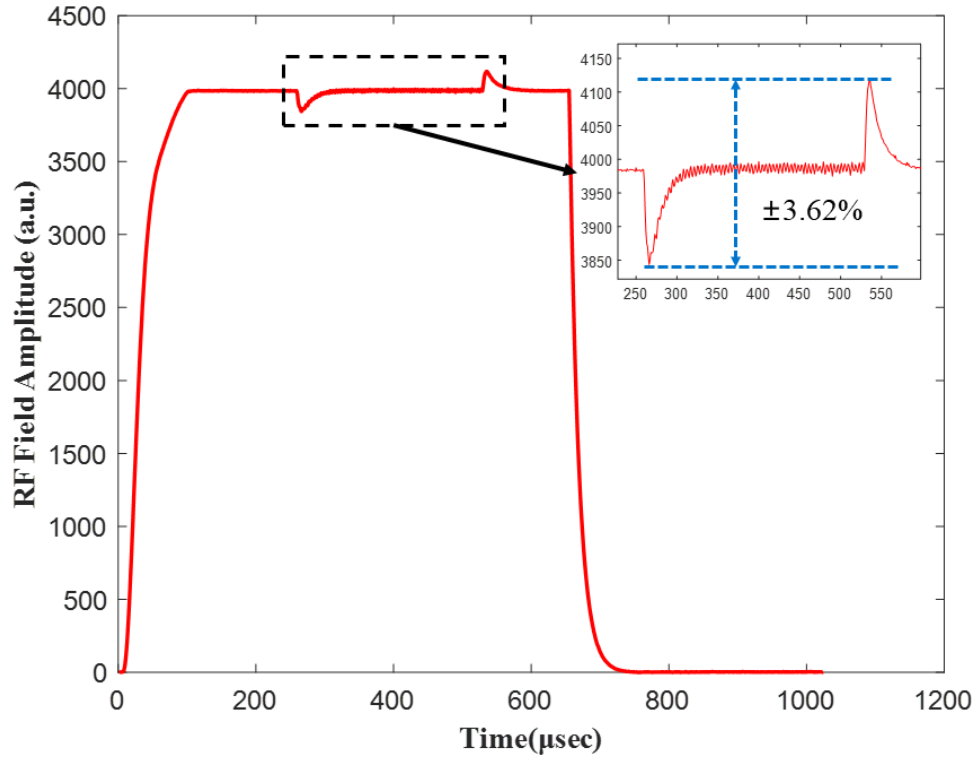


Figure 1.9. Extreme case of amplitude waveform in the SDTL01 station.



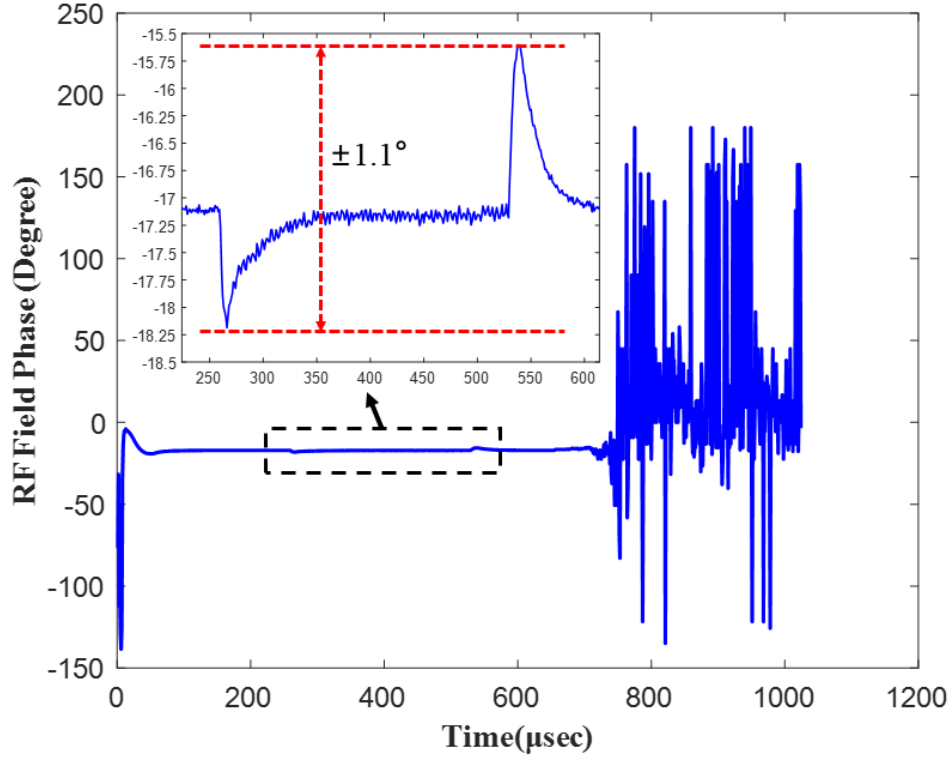


Figure 1.10. Extreme case of phase waveform in the SDTL01 station.

Another significant issue that J-PARC LINAC faced is that the current low-level radio frequency (LLRF) system has been running for more than 10 years. Even it still works well, the supplier didn't produce the same products many years before, nor did they maintain. And existing systems cannot meet the needs of future upgrades due to resource limitations. To ensure the normal operation of J-PARC LINAC, a new LLRF control system was developed which core part is a MTCA based digitizer [5].

## 1.4 Structure of The Thesis

The thesis consists of eight chapters. A brief introduction to each chapter is given below.

- Chapter 2 gives an overview of beam loading compensation methods in digital low-level radio frequency (LLRF) system for different large facilities. Their schemes and performance are summarized and compared.



- Chapter 3 introduce the J-PARC LINAC LLRF system. The information of current LLRF system will be introduced. The status of development of the new system in the J-PARC LINAC LLRF is presented.
- Chapter 4 introduce the Iterative Learning Control (ILC) theory. In this chapter, the principle of ILC will be illustrated. The ILC control scheme for the J-PARC LINAC is presented. Norm-Optimal ILC methods will also be discussed.
- Chapter 5 introduces the implementation of ILC simulation design for LLRF system on MATLAB, Simulink. The results of simulation test will be shown and discussed.
- Chapter 6 details the software and hardware setup work for ILC based beam loading compensation experiment.
- Chapter 7 shows the ILC based beam loading compensation experimental results.
- Chapter 8 gives a mathematical analysis on the LLRF system with an ILC based feedforward. The stability and convergence of the system will be discussed.
- Chapter 9 summarizes the thesis. The possible future upgrade plan for ILC based feedforward method will be discussed.

## Chapter 2

# Overview of Beam Loading Compensation Method for the LLRF System

This chapter mainly discusses the beam loading compensation method that used in European XFEL, Los Alamos Neutron Science Center and FLASH. Both the LLRF system and the realization method will be introduced. The performance will be shown and evaluated.

### 2.1 European XFEL

The European X-Ray Free Electron Laser (XFEL) is a 17.5 GeV coherent light source, which operates in pulse mode, providing laser pulses of tunable wavelength by the SASE process. It provides 27,000 flashes per second with a wavelength as low as 0.05 nm and a peak brilliance of  $5 \times 10^{33}$  photon/s/mm<sup>2</sup>/mrad<sup>2</sup>/0.1% bandwidth [6]. The main components of the accelerator chain are shown in the [Figure 2.1](#). The main superconducting linac in XFEL has been divided into 25 RF stations. Each of the RF stations consist of four cryogenics accelerating modules (CM), which is powered by a 10 MW klystron and a dedicated LLRF system that is split into master and slave subsystems.

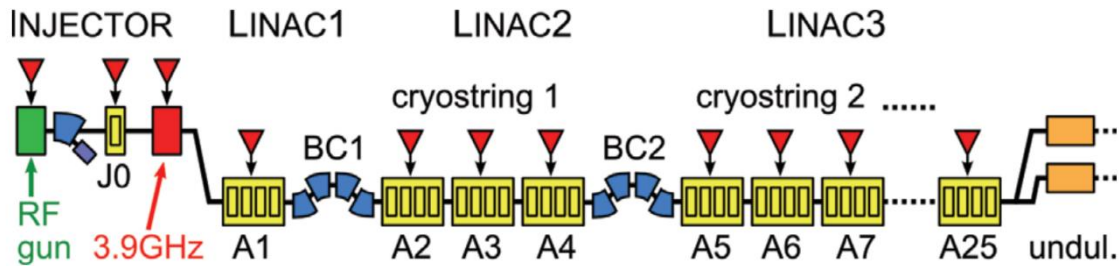


Figure 2.1. XFEL accelerator overview

[Figure 2.2](#) shows the LLRF system installed at one RF station in XFEL. Two

MTCA.4 crates were installed at each of the RF stations, one crate in the master and one crate in the slave LLRF subsystems. There are six pairs of down-converter (uDWC) - digitizer (uADC) boards, LLRF controller (uTC), CPU, crate management module (MCH), timing card (x2timer) for both master and slave LLRF MTCA.4 crate. The different place is that there is a vector modulator (uVM) only in the master crate. RF signals from two cryo-modules will be sent into the LLRF system. After processing, the master crate will provide the drive signal to the klystron. The uTC board in the master subsystem is the core part of LLRF system which contains the main LLRF controller. All the algorithms are implemented in the FPGA chip located on the uTC board. The data are transmitted over optical links or over differential lines within the crate and are received by the main controller using Multi-Gigabit Transceivers (MGTs).

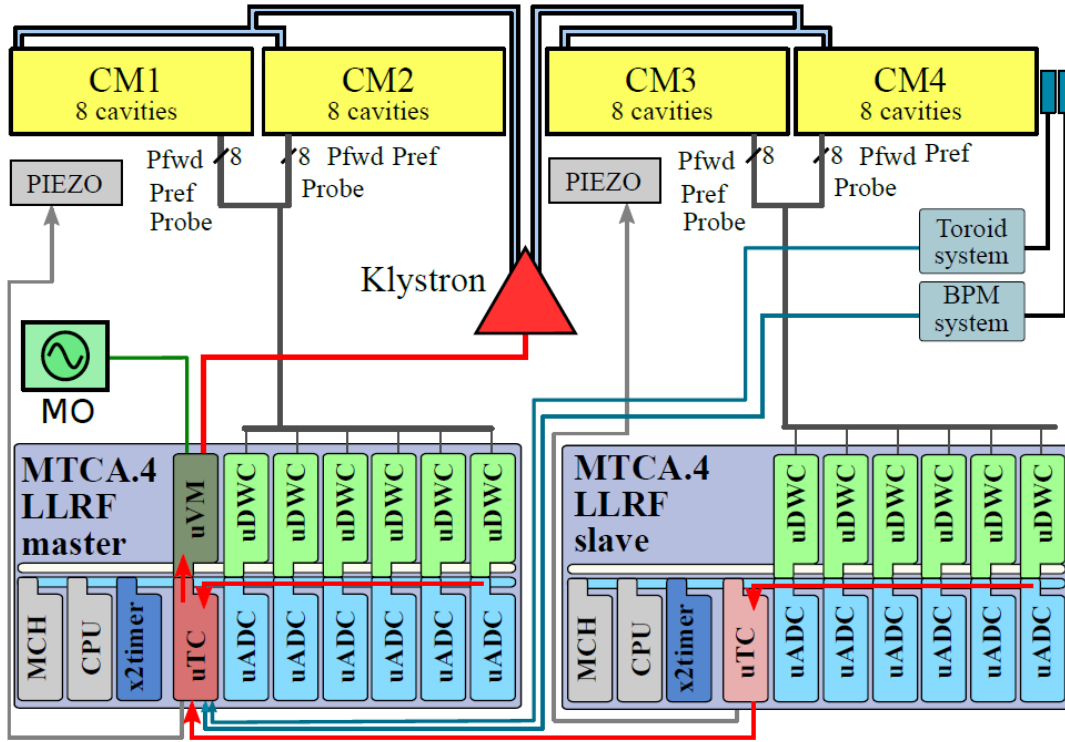


Figure 2.2. Simplified block diagram of the LLRF system installed at one RF station in European-XFEL.

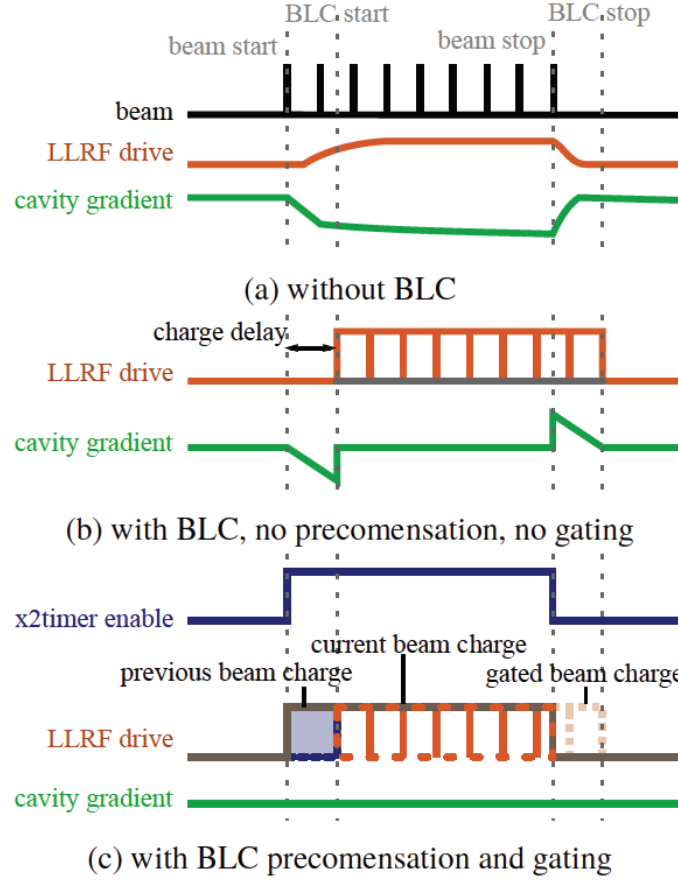


Figure 2.3. Beam loading compensation and cavity gradient.

To compensate the deformation of cavity gradient, the scaled beam charge information was added into the feedforward signal. Due to the influence of delay resulting from the detection of bunches and data transmission, the first bunches see a different cavity gradient and at the last electron bunch there is an overcompensation shown in the Fig. 2.3 (b). To solve this problem, a pre-compensation and gating algorithm is used. In this algorithm, before the charge information from the current pulse arrives, the beam charge information from previous pulse was inserted. And when no beam comes, invalidate the beam loading compensation function. Because the algorithm requires the expected time of the beam, a module that receive the data from the timing system was used to generate the indication of the expected beam and supply rough amplitude value of he expected beam charge.

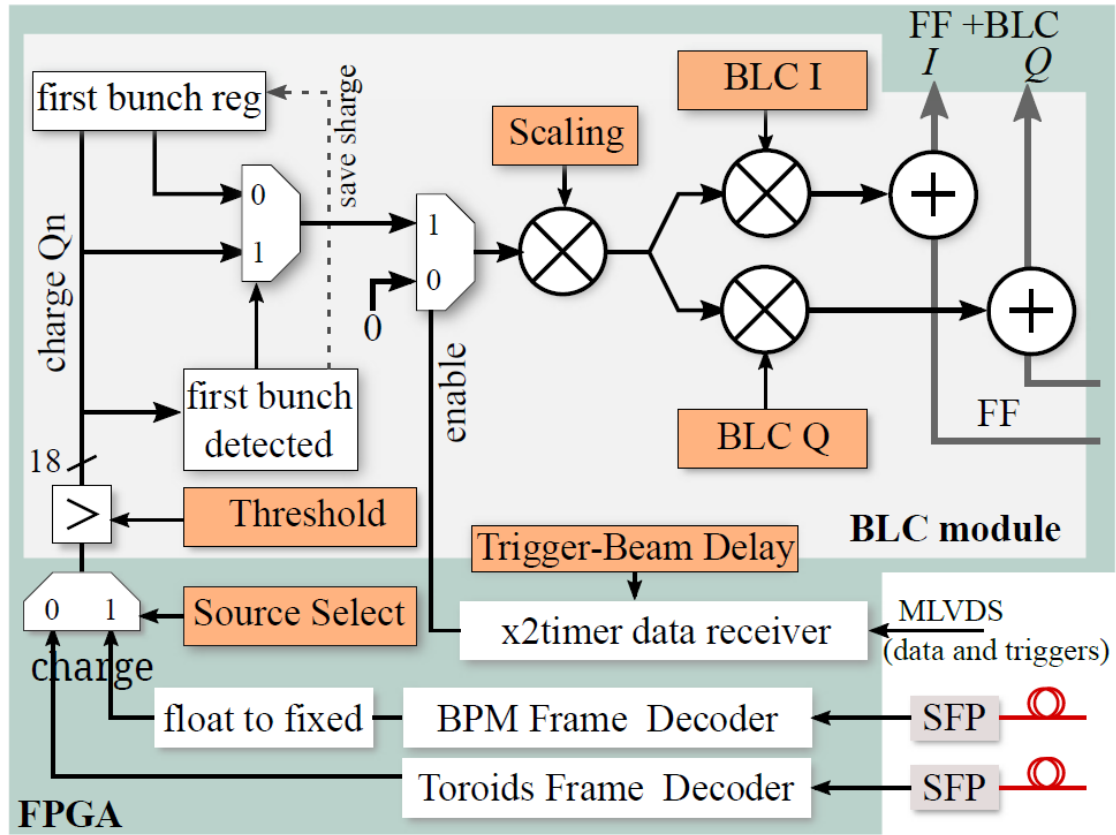


Figure 2.4 Block diagram of Beam Loading Compensation module.

Figure 2.4 shows the block diagram of beam loading compensation module. The information of beam charge can be select between the BPM and Toroids. The orange blocks in the figure indicate the registers that are set by the user. Among of them, the scaling of the beam charge and the rotation of the correction vector are the two important parameters that have to be set.

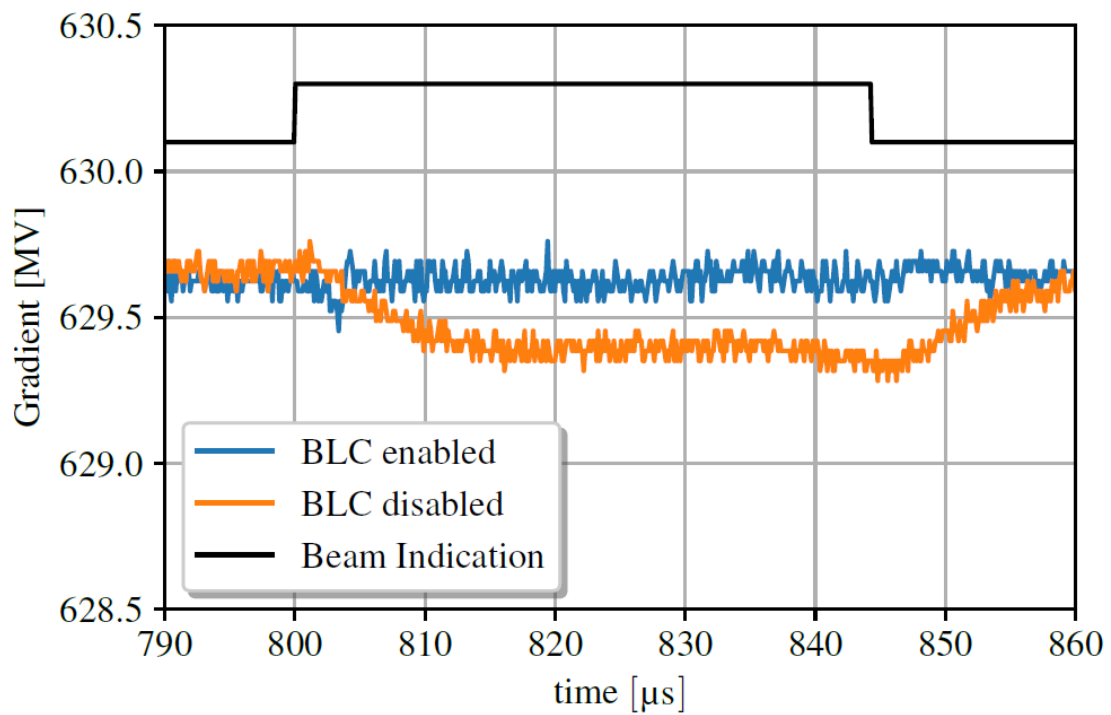


Figure 2.5. Cavity gradient with BLC enabled and disabled for beam with 50 bunches with 0.25 nC @1MHz repetition rate.

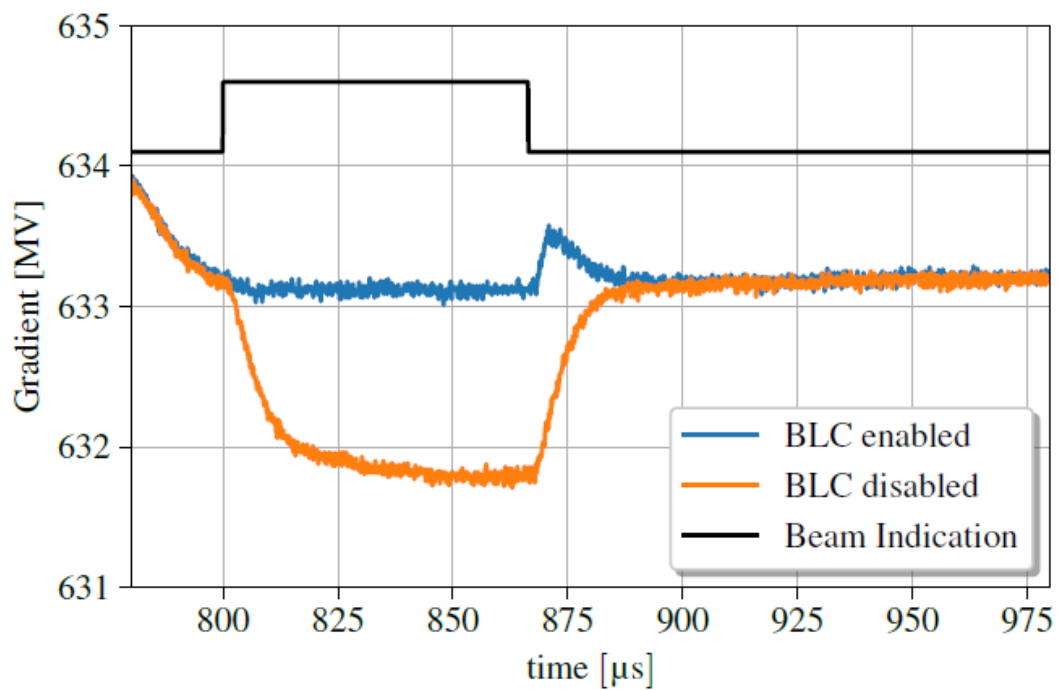


Figure 2.6. Cavity gradient with BLC enabled and disabled for beam with 300 bunches with 0.25 nC @4.5MHz repetition rate.

The results of BLC working for a bunch pattern with 0.25 nC and 1MHz repetition rate are shown in the Fig. 2.5. And the results for the situation of 0.25 nC and 1MHz repetition rate are presented in the Fig. 2.6. Both of them are under the effect of feedback control. The gradient disturbance caused by the beam was compensated when the beam loading compensation module work.

## 2.2 Los Alamos Neutron Science Center

At LANSCE, to handle the exotic beam loading conditions which may have in the MaRIE (Matter-Radiation Interactions in Extremes) free electron laser (FEL), a model-independent iterative Extremum Seeking (ES) method for automatic beam loading compensation was developed [7].

The  $I(t)$  and  $Q(t)$  components of the cavity voltage signal were sampled at a rate of 100 MS/s during a 1000  $\mu$ s RF pulse. The detected RF signal was then broken down into 10  $\mu$ s long sections and feed forward  $I_{ff,j}(n)$  and  $Q_{ff,j}(n)$  control outputs were generated for each 10  $\mu$ s long section, as shown in the Fig. 2.7. Here,  $j$  denotes the iteration index and  $n$  represents the discrete time index.

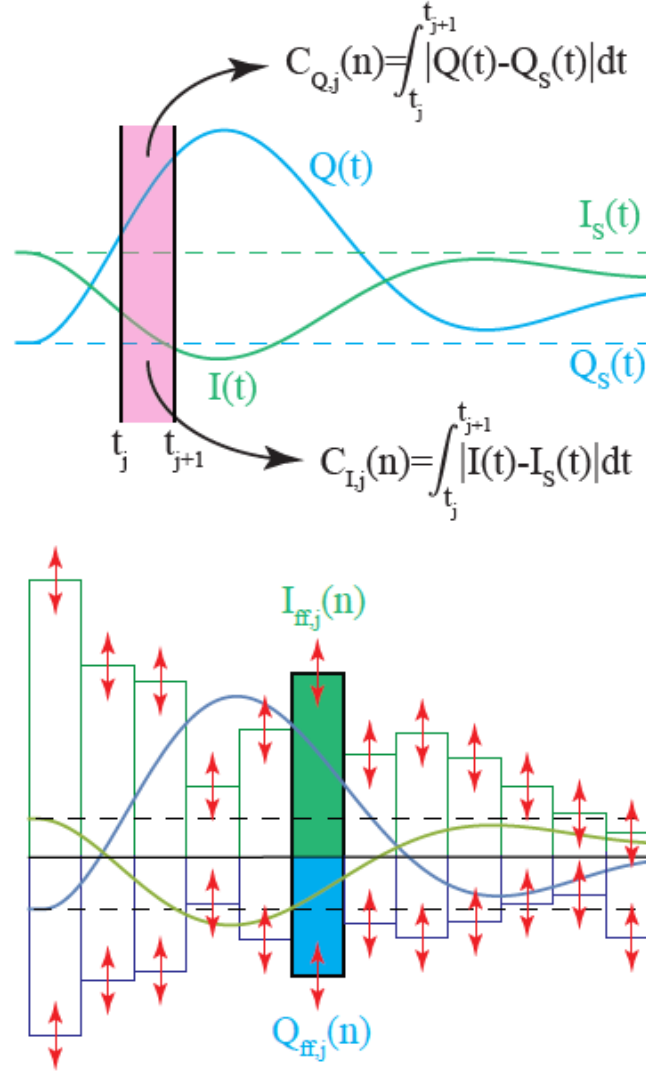


Figure 2.7. **Top**: Iterative scheme for determining I and Q costs during 1-10  $\mu$ s intervals. **Bottom**: ES-based feedforward outputs for beam loading transient compensation.

The iterative extremum seeking was performed via finite difference approximation of the ES dynamics:

$$\frac{x(t+dt) - x(t)}{dt} \approx \frac{dx}{dt} = \sqrt{\alpha\omega} \cos(\omega t + kC(x, t)) \quad (2.1)$$

The updating algorithm of iterative extremum seeking is given below,



$$I_{ff,j}(n+1) = I_{ff,j}(n) + \Delta\sqrt{\alpha\omega} \cos(\omega n\Delta + kC_{I,j}(n)) \quad (2.2)$$

$$Q_{ff,j}(n+1) = Q_{ff,j}(n) + \Delta\sqrt{\alpha\omega} \sin(\omega n\Delta + kC_{Q,j}(n)) \quad (2.3)$$

Where the addition of the  $w$  as a gain of the dithering signal,  $\alpha$  and  $k$  are the gain of ES algorithm. The individual I and Q costs were calculated as

$$C_{I,j}(n) = \int_{t_j}^{t_{j+1}} |I(t) - I_s(t)| dt \quad (2.4)$$

$$C_{Q,j}(n) = \int_{t_j}^{t_{j+1}} |Q(t) - Q_s(t)| dt \quad (2.5)$$

although the  $I_j$  and  $Q_j$  parameters were updated on separate costs, they were still dithered with different functions,  $\sin(\cdot)$  and  $\cos(\cdot)$ , to help maintain orthogonality in the frequency domain.

Then the feed forward signals were added to the PI and static feed forward controller outputs. Running at a repetition rate of 120 Hz, the feedback converges within several hundred iterations or a few seconds. The experimental results are shown in the [Fig. 2.8](#) and summarized in the [Table 1](#). The maximum, rms, and average values are all calculated during a 150  $\mu$ s window which includes the beam turn on transient to capture the worst case scenario. Compared to the static feedforward, the performance of iterative ES improves the amplitude stability is increased by two times and the phase stability is increased by three times.

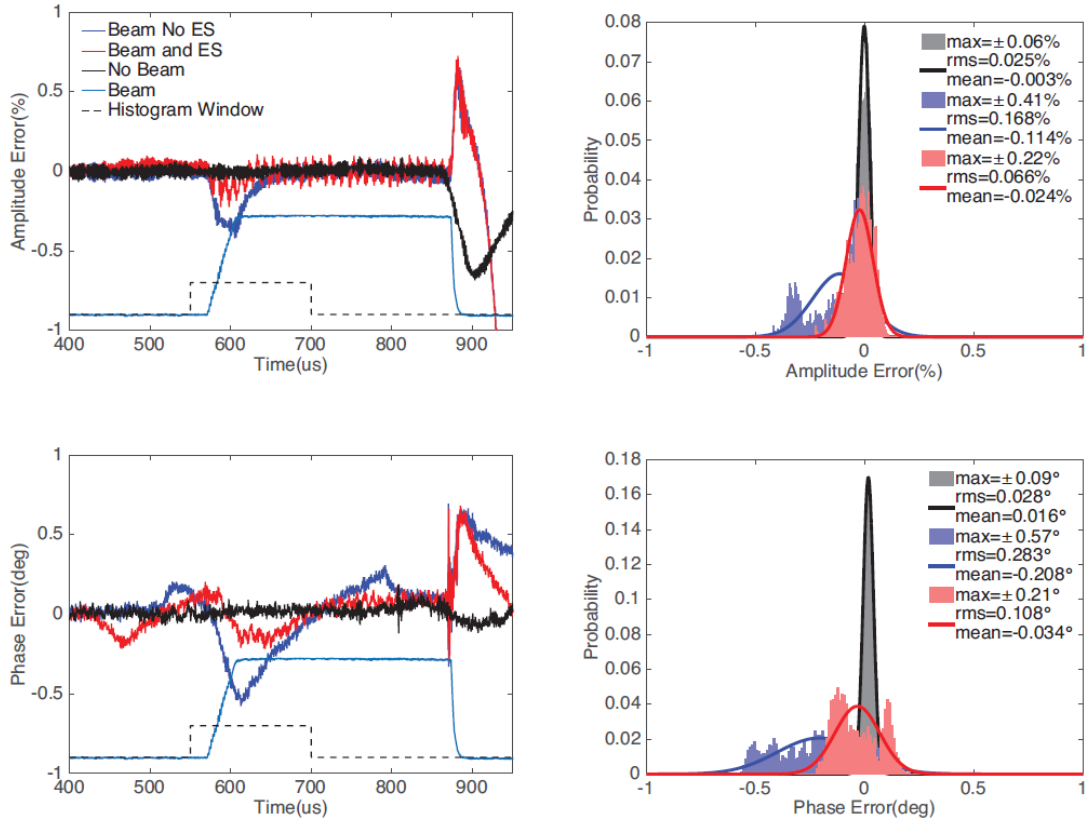


Figure 2.8. Phase and amplitude errors shown before, during, and after beam turn-on transient. The histogram data shown is collected during the dashed histogram window and cleaned up via 100 point moving average after raw data was sampled at 100 MS/s. **Black**: Beam OFF. **Blue**: Beam ON, feedback, and static feed-forward only. **Red**: Beam ON, feedback, static feed-forward, and iterative ES feed-forward.

Table 1: ES performance during beam turn on transient

	No beam	Beam, No ES	Beam & ES
Max A error (%)	$\pm 0.06$	$\pm 0.41$	$\pm 0.22$
RMS A error (%)	0.025	0.168	0.066
Mean A error (%)	-0.003	-0.114	-0.024
Max $\theta$ error (%)	$\pm 0.09$	$\pm 0.57$	$\pm 0.21$
RMS $\theta$ error (%)	0.028	0.283	0.108
Mean $\theta$ error (%)	0.016	-0.208	-0.034

## 2.3 FLASH

At DESY, Free Electron Laser FLASH, an iterative learning control was used to suppress the repetitive disturbance, which mainly Lorentz detune and beam loading, in the cavity [8]. The block diagram of RF system is shown in the Fig. 2.9. In their case, one high power klystron supplies all 8 – 32 cavities of an RF station, thus RF fields can not be influenced in each cavity individually namely the system is underactuated. After measuring the actual RF-field by pickup antennas, the signals are down converted to an intermediate frequency of 250 kHz. The real (I) and imaginary (Q) field measurement signals go through analog-digital-converters (ADC) with a sampling frequency of 1 MHz. And then a calibration of the measurement signals is done. Due to the lack of individual actors for each cavity, the control algorithm uses the vector sums of all calibrated measurement signals of the individual cavities as signals to be controlled.

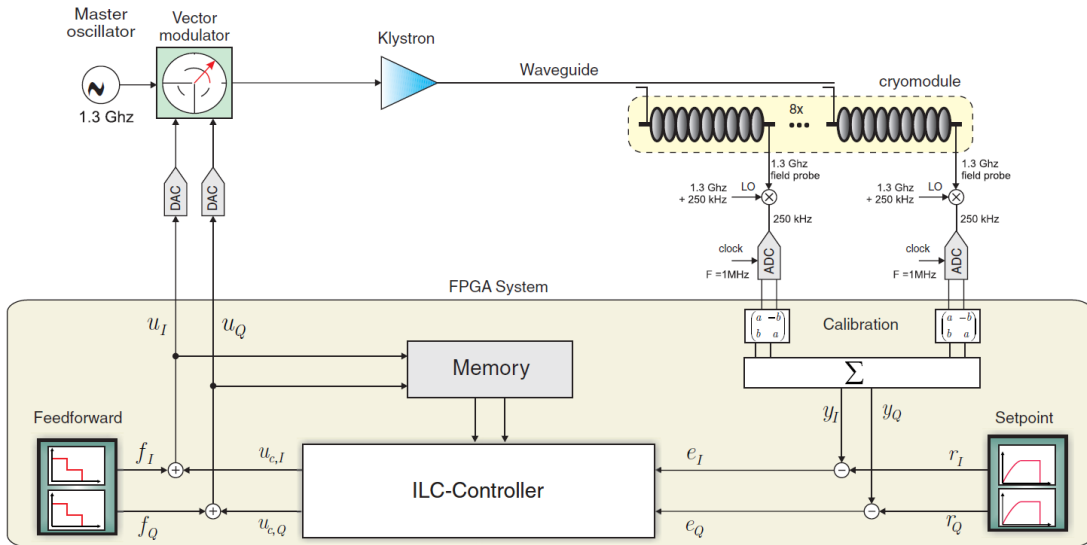


Figure 2.9. Structure of the RF system with master oscillator, vector modulator, klystron, cryomodule, measurement, and calibration system and the FPGA implemented control system.

The signals shown in the Fig. 2.9 are summarized below:

- Input signals  $u_I, u_Q$ : Control signals of the actuator system are directly acting on the vector modulator.

- Output signals  $y_I, y_Q$ : The real and imaginary part of the sum of the RF-field voltage vectors of eight cavities.
- Reference signals  $r_I, r_Q$ : Reference signals of the real and imaginary part of the vector sum of the RF-field's voltage vectors given by look-up tables for the specified field gradient.
- Feedforward signals  $f_I, f_Q$ : Part of the control signals determined by open loop control.
- Control signals  $u_{cI}, u_{cQ}$ : The learning controller output signals, updating the previous iteration input signals
- Control error signals  $e_I, e_Q$ : Deviations in real and imaginary part of the output signals from the reference signals.

Due to Lorentz force detuning and beam loading are repetitive disturbances, and desired setpoint could be reached with pure feedforward control if the input signals are sufficiently adapted to the disturbance sources. In this case, Iterative learning control (ILC) is a very good choice. The goal of ILC is to generate a new feedforward data which can make the output value keep approaching to the ideal value by using the information from previous input and error as the number of iteration increases. Then the output I & Q signals go through the digital-analog-converters (DAC) and sent to the vector modulator to do the adjustment of amplitude and phase.

The ILC scheme is the Fast-Norm-Optimal Iterative Learning Control (F-NOILC). The objective of an ILC can be described by

$$\|e_k\| \rightarrow 0 \text{ as } k \rightarrow \infty, k \in \mathbb{N} \quad (2.6)$$

where  $e_k = (e_I \ e_Q)^T$  denotes the tracking error vector signal of the desired trajectory of the  $k$ th trail. In order to be able to compute an optimal input signal, a criterion has to be determined that reflects the goal of the control task and thus, the quality of the input. This is done by solving the following minimum-norm optimization problem:

$$u_{k+1} = \operatorname{argmin}\{J_{k+1}(u_{k+1}): e_{k+1} = r - y_{k+1}, y_{k+1} = Gu_{k+1}\}, \quad (2.7)$$

with the performance index

$$J_{k+1}(u_{k+1}) = \|e_{k+1}\|^2 + \|u_{k+1} - u_k\|^2, \quad (2.8)$$

where the norms  $\|\cdot\|$  are defined as  $\|u\|^2 = u^T w_2 u$ , and  $\|y\|^2 = y^T w_1 y$  for input and output, respectively. Consider the state space model of controlled system:

$$\begin{aligned} \dot{x}(t) &= Ax(t) + Bu(t) \\ y(t) &= Cx(t) + Du(t) \end{aligned}$$

where  $u = (u_I \ u_Q)^T$ ,  $y = (y_I \ y_Q)^T$  denote the system input and output vector, respectively and  $x$  is the state vector of the system. The performance criterion described in (2.3.3) can be rewritten as

$$\begin{aligned} J_{k+1} &= \sum_{t=1}^N [r(t) - y_{k+1}(t)]^T w_1(t) [r(t) - y_{k+1}(t)] \\ &+ \sum_{t=0}^N [u_{k+1}(t) - u_k(t)]^T w_2(t) [u_{k+1}(t) - u_k(t)] \end{aligned} \quad (2.9)$$

The quantities  $w_1(t)$  and  $w_2(t)$  represent time varying weighting matrices which have to be symmetric and positive definite for all  $t$ . The  $k+1$  trial control input is determined such that it reduces the tracking error  $e$  while keeping the deviation from the control input used in the  $k$ th trial small.

The F-NOILC updating algorithm can be found in the [Table 2](#). The algorithm is divided into three levels. In the first level the algorithm is initialized. In the second level computations are carried out between trials, such as the calculation of a predictive component. The input signals with a state feedback component are computed in the third level, which represents computations between the sampling instants of a trial.

Table 2: Control Algorithm F-NOILC

First level (before operation):

$$\begin{aligned}
K(t) &= A^T K(t+1)A + C^T W_1(t+1)C \\
&\quad - [A^T K(t+1)B \{B^T K(t+1)B + W_2(t+1)\}^{-1} B^T K(t+1)A] \\
\alpha(t) &= \{I + K(t)B W_2^{-1}(t)B^T\}^{-1} \\
\beta(t) &= \alpha(t)A^T \\
\gamma(t) &= \alpha(t)C^T W_1(t+1) \\
\omega(t) &= W_2^{-1}(t)B^T \\
\lambda(t) &= \{B^T K(t)B + W_2(t)\}^{-1} B^T K(t)A
\end{aligned}$$

Second level (between trials):

$$\xi_{k+1}(t) = \beta(t)\xi_{k+1}(t+1) + \gamma(t)e_k(t+1)$$

Third level (between sampling instants):

$$u_{k+1}(t) = u_k(t) - \lambda(t)\{x_{k+1}(t) - x_k(t)\} + \omega(t)\xi_{k+1}(t)$$

Fast and efficient computation is important when computing the updated input signal. The time interval between two consecutive RF pulses is approximately 0.1 s. Furthermore, a state feedback control input has to be computed in each sampling period of 1 $\mu$ s. Using a workstation computer with an Intel Pentium 4 processor with a clock speed of 3 GHz, the computation time needed for the three different time levels is given in the [Table 3](#).

Table 3: Available and required computation time for different levels

	1 <sup>st</sup> level	2 <sup>nd</sup> level	3 <sup>rd</sup> level
Needed time [s]	24.71	0.0147	0.0047
Available time [s]	$\infty$	0.1	0.000001

The time needed between samples exceeds the time that is available. Consequently, the third level computations are executed in the second level for the results below. The input signals are then computed for the whole trial at once, instead of for every sample separately. To prevent damage to system components when the algorithm is implemented on the real plant, the input

signals are limited as shown in the [Fig. 2.10](#). The limits are set to the maximum and minimum values of the input signals during the filling and the decay phase.

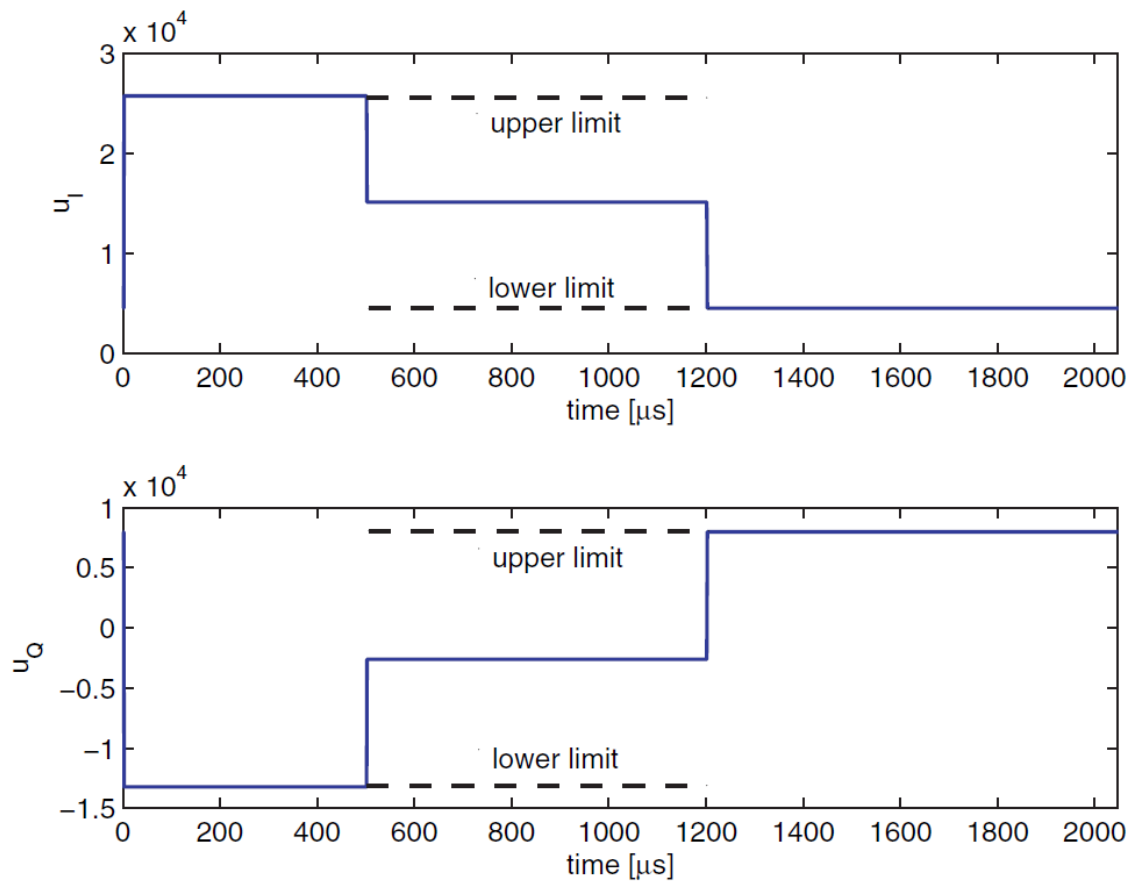


Figure 2.10. Limits on input signals.

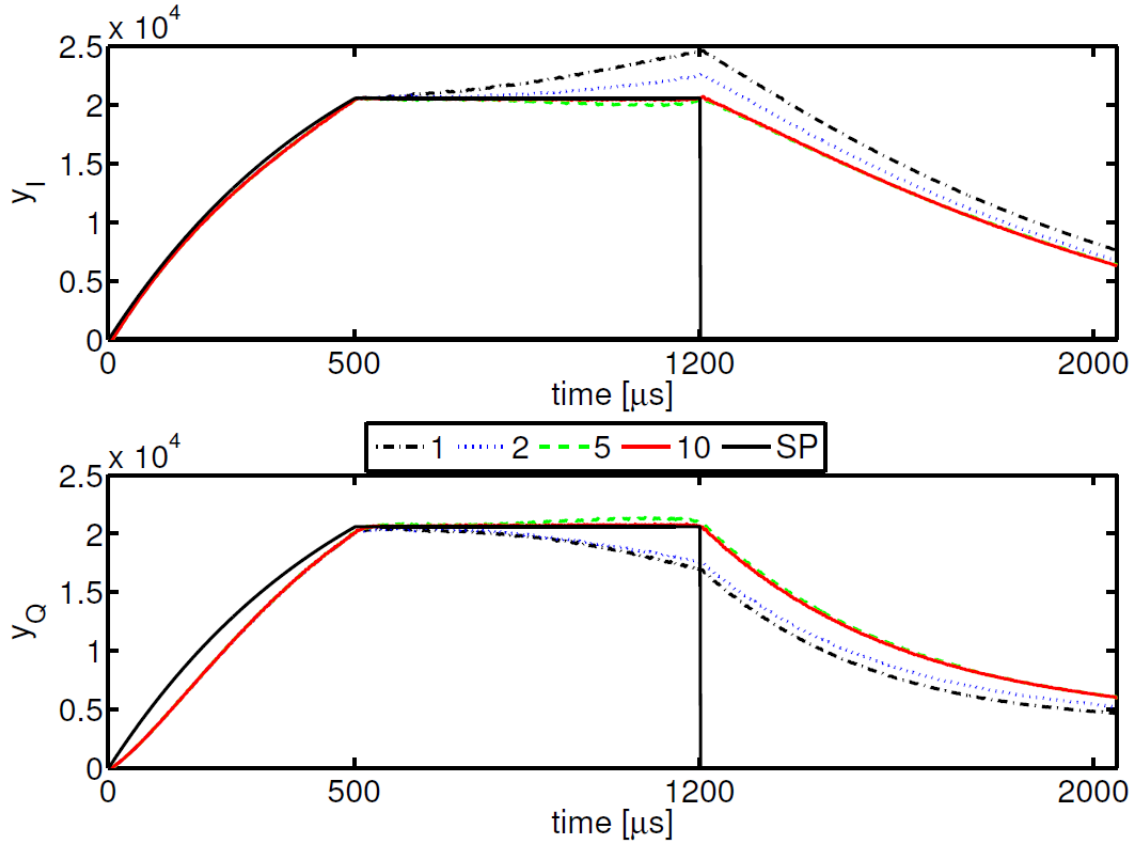


Figure 2.11. Measured output signals.

The real experimental results are shown in Fig. 2.11 and 2.12. [Figure 2.11](#) shows an increasing and decreasing trend of the output signal, respectively. This is the general behavior caused by the detuning effects. However, increasing the number of trials, both output signals approach the desired setpoint. After 10 iterations, the output signals show only small deviations from the reference trajectory. Since only the signals during the flat top phase are controlled, the input signals of the filling and the decay phase are kept constant as illustrated in the [Fig. 2.12](#).



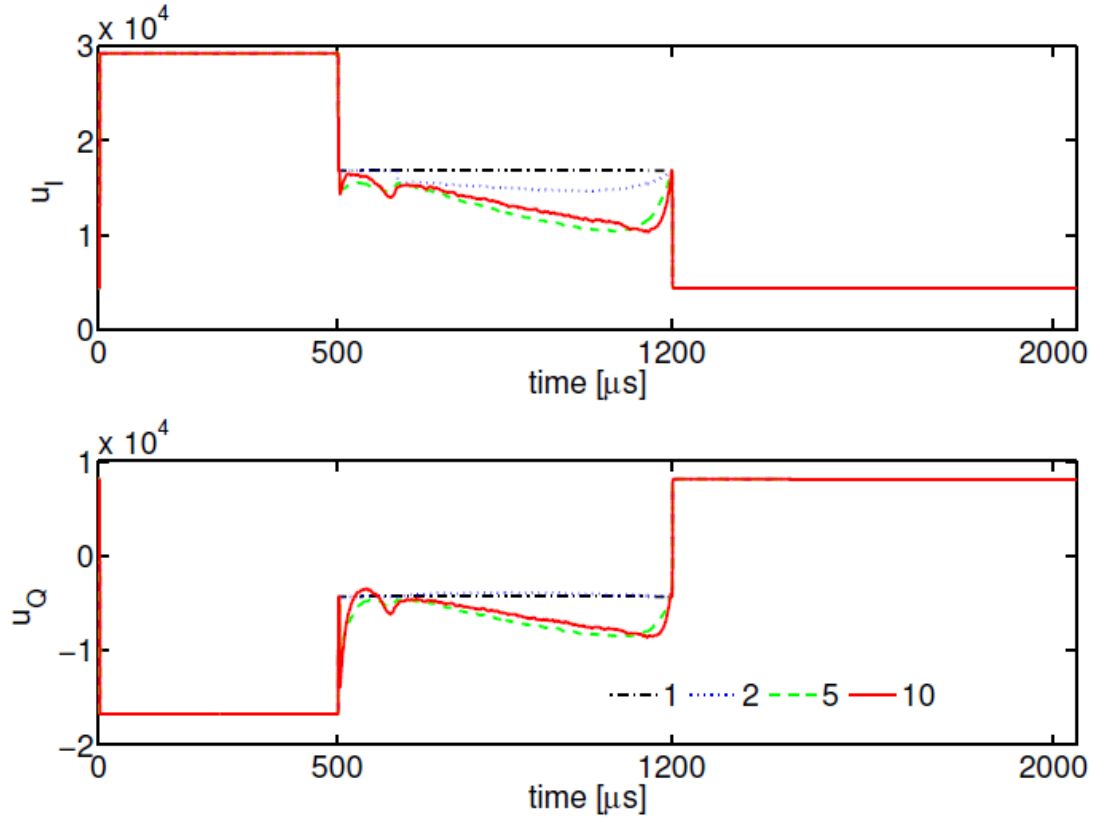


Figure 2.12. Measured input signals.

In order to emphasize the improvements in the field regulation gained by application of NOILC, [Figure 2.13](#) gives a comparison to the decentralized proportional controller previously used for field regulation and a MIMO feedback controller. The MIMO feedback controller improves both effects but by itself is not able to fully compensate for them. Applying the norm-optimal ILC significantly reduces the control error to a level which is required to give an appropriate beam energy gain. In summary, the experimental results show performance improvements are possible with norm-optimal ILC applied, even though only tests with a small number of trials could be executed.

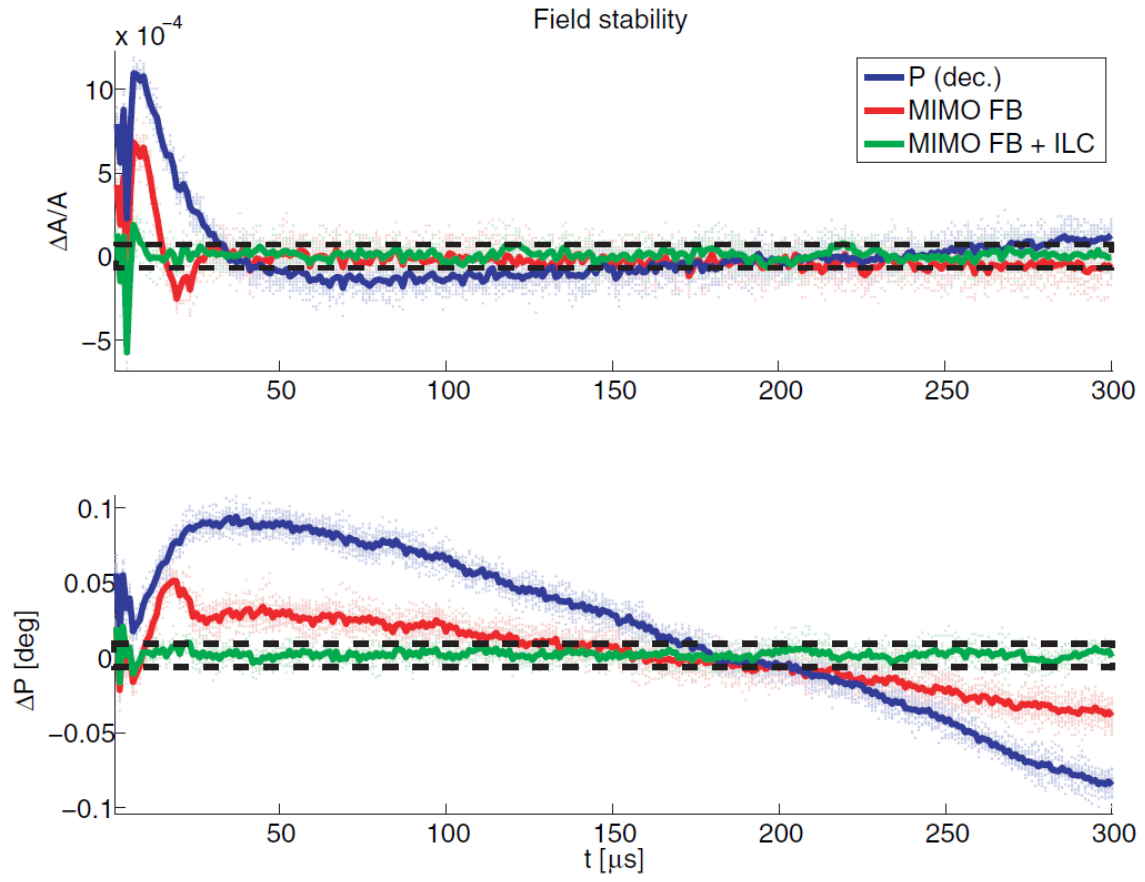


Figure 2.13. Performance comparison between proportional feedback, MIMO feedback only, and the combination with NOILC.

## 2.4 Comparison of Scheme

In this chapter, we introduce three beam loading compensation methods that used in European XFEL, Los Alamos Neutron Science Center and FLASH, respectively.

In European XFEL, the beam loading compensation method is the upgrade version of static feedforward control which is similar to the current J-PARC compensation method. In LANSCE, MaRIE, an iterative extremum seeking methods was used to do the beam loading compensation. ES is a good method to improve the transient response performance of system. However, for the best performance it still needs the help of normal static feedforward and feedback instead of replacing feedforward. In FLASH, a norm optimal iterative learning control were used to suppress the repetitive disturbance include beam loading in the cavity. The experimental results show that the compensation performance of NOILC combine with MIMO feedback is very good. But the method is a little complicate and occupy a lot of FPGA resources. What's more, the time interval between pulse to pulse is a little longer for J-PARC LINAC.

In the J-PARC LINAC, we wish to find a beam loading compensation method which performance is better than static feedforward, won't occupy much resource and can complete compensation in a short time. As the method to satisfy all the condition above, the first order P-type iterative learning control was chosen to be used in the J-PARC LINAC.

## Chapter 3

# The Upgrade of J-PARC LINAC LLRF System

In this chapter, both the current and new LLRF system will be introduced. Two system will be fully compared. The performance of the new system will be evaluated.

### 3.1 Current LLRF System

J-PARC LINAC started operation in 2006. At that time, the J-PARC LINAC was operated at a proton beam energy of 181 MeV by using the 324-MHz low- $\beta$  accelerator section. It was in 2014, after installing 972-MHz high- $\beta$  accelerator section, the beam was successfully accelerated to 400 MeV. The LLRF system in the 324-MHz low- $\beta$  accelerator section has been running for more than 12 years. [Figure 3.1](#) shows the block diagram of LLRF control system currently in use. The information of two cavities is collected by two RF signals. For subsequent digital processing, these two signals are down-converted to 12 MHz IF (Intermediate Frequency) signals by mixers and then sent to 14-bits ADCs in FPGA board with 48 MHz sampling clock.

In the processing stage of FPGA, firstly the original digital signals need to be converted into IQ signals through IQ detector, where I represent the “In-phase” component of the waveform and Q represents the “Quadrature” component. Then considering that the cavity field waveform needs to be calibrated before the feedback is turned on, the rotation modules are added behind IQ detector to adjust the amplitude and phase of waveform. Selector module allows us to choose the signals of desired cavity, which can be the signal from cavity one, cavity two or the average of them. In order to get the error of feedback control, the data of reference waveform will be stored in the reference table in the form of IQ components. When the feedback switch is turned on, the error between the reference and ADC will be calculated and send to PI (Proportion and Integral) controller. PI controller is the core part of LLRF feedback control, choosing appropriate PI parameters will help us get a stable and flat RF pulse

waveform. FF\_base and FF\_beam are two feed forward tables which independently triggered by RF and Beam gates, respectively. The goal of FF\_base is to form a basic accelerating field. Waveform data saved in FF\_base table is almost the same as reference waveform. The only difference is that the rise time of FF\_base waveform is shorter than that of the reference waveform due to the system loop delay. The aim of FF\_beam is to compensate for the beam loading. For current system, the feed forward data in FF\_beam table is a fixed rectangular waveform which height is consistent with the depth of the depression caused by beam loading. By adjusting the timing of FF\_beam, namely, the rising-edge of Beam gate pulse signal, the feed-forward waveform can be aligned with the depression caused by beam loading. In addition, IQ modulator was found to generate an undesired output even with the I and Q components of DAC outputs set to 0 during the RF control system operation with FB (feedback) OFF. Therefore, the I and Q offset tables were added to the feedback calculation loop in the front of the DACs to eliminate its effects.

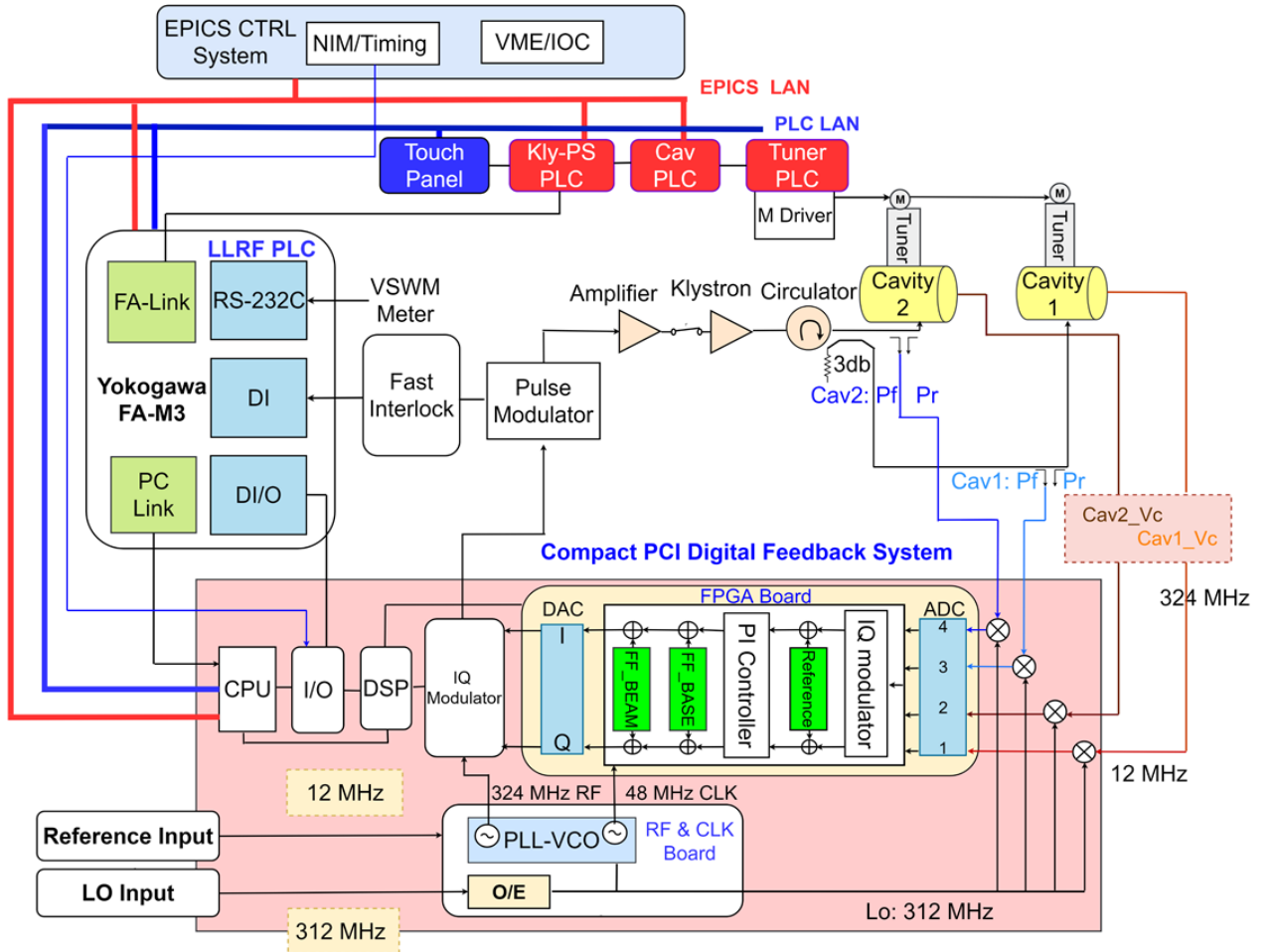


Figure 3.1. Block diagram of LLRF control system.

The output signals of FPGA will be sent into IQ modulator through 16 bits DAC. In IQ modulator, the IQ signal will change back to the normal signal and up convert to the 324 MHz or 972MHz high frequency signal. Due to sometimes the output signal of IQ modulator was CW (Continuous Wave), so there is a pulse modulator to change the CW signal to Pulse signal. After that, the signal will be amplified twice by solid-state amplifier and klystron, and finally fed into the cavity.

### 3.2 New LLRF System Under Development

Since the version of the current device is too old, the manufacturer no longer sells the same products and there is no related maintenance. What's more, the limited resources of the current system cannot meet the needs of future upgrades. Considering the above two points, a new LLRF control system was developed for J-PARC LINAC.

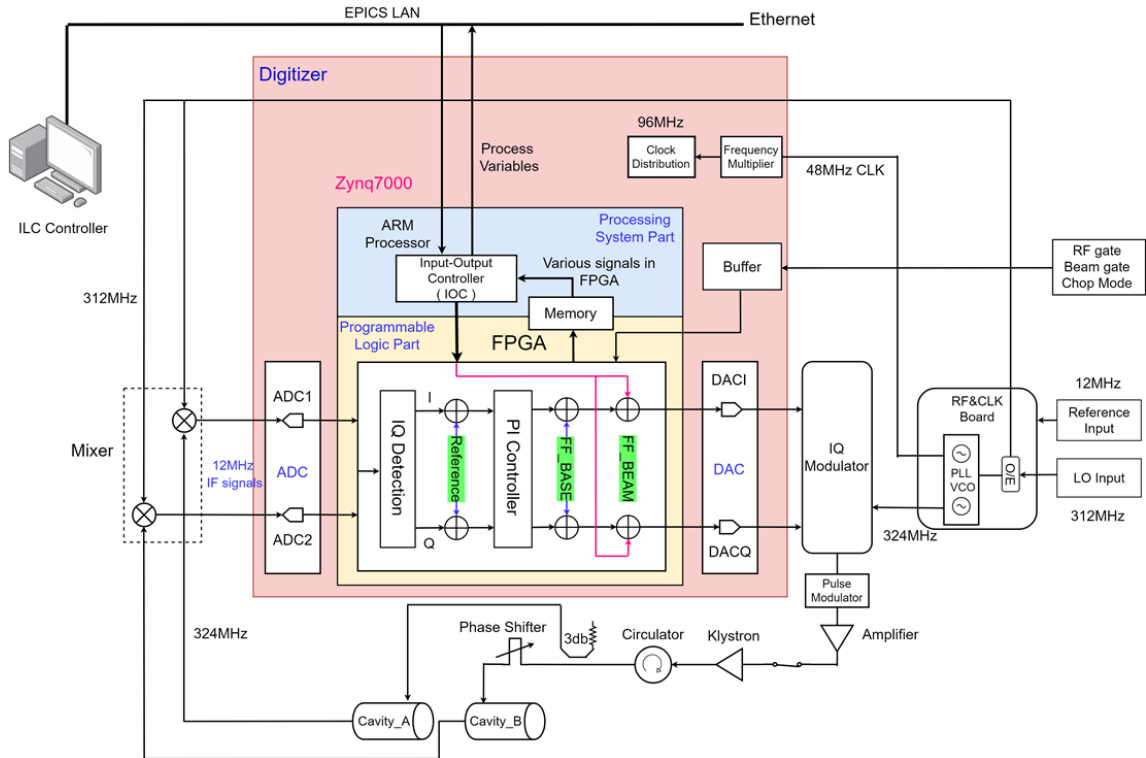


Figure 3.2. Block diagram of new LLRF control system

Figure 3.2 shows the block diagram of new LLRF control system. The biggest difference between the current system and the new system is that FPGA board is no

longer placed in the Compact PCI chassis but inside the digitizer which adopted MTCA.4 architecture. In digitizer, the board is mainly divided into two parts, Rear Transition Module (RTM) and Advanced Mezzanine Card (AMC). In RTM, except ADC input circuit, DAC output circuit and power supply circuit, there is a Phase-Locked Loop frequency multiplier that turns 48 MHz external clock signal into 96 MHz internal clock signal. A LVCMOS buffer converts +5V TTL gate signals into +2.5V LVCMOS signals for use by the FPGA. In AMC, there are a Zynq-7000 SoC (System on Chip), 8 ADC modules, 2 DAC modules and a clock distribution circuit. Zynq-7000 SoC mainly composed of two parts, processing system and programmable logic. Processing system part features an ARM Cortex-A9 processor, we use it to implement the IOC (Input Output Controller) of EPICS (Experimental Physics and Industrial Control System). And the Artix-7 based programmable logic part implements the same functionality as the current FPGA board.

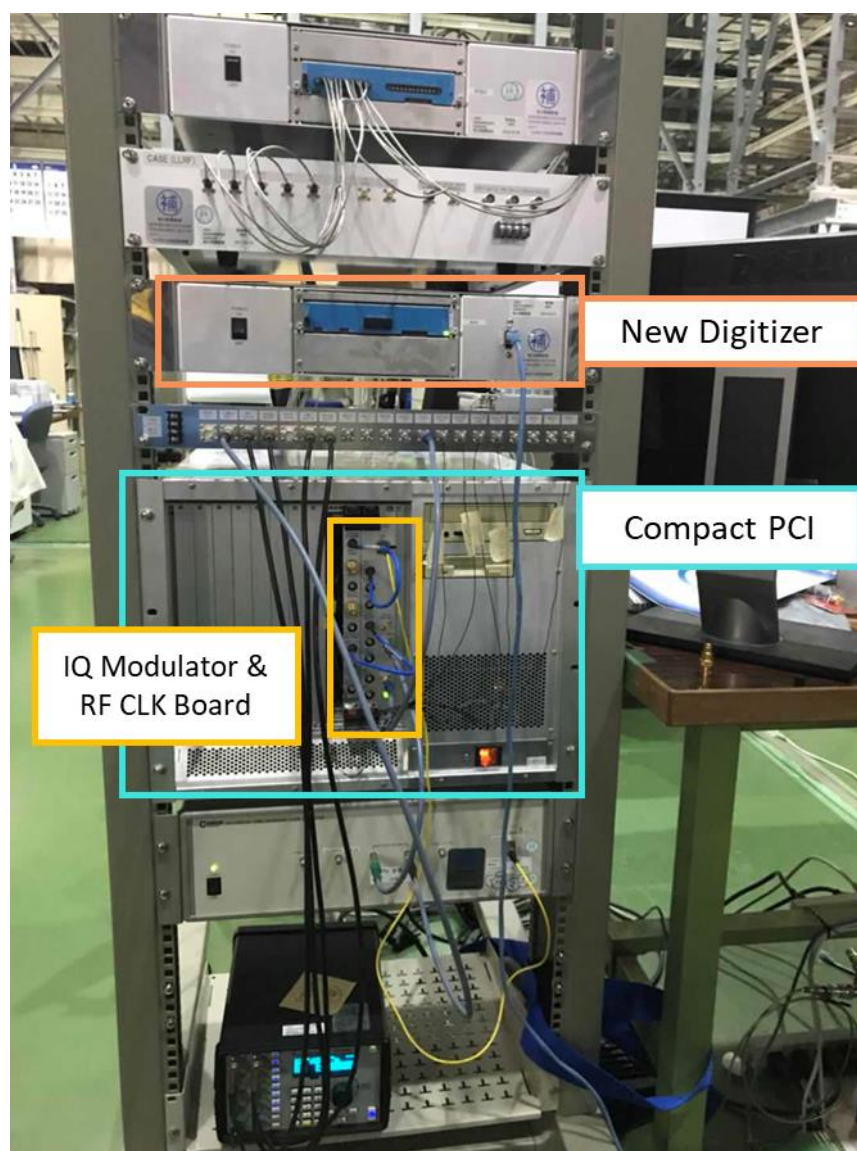


Figure 3.3. Prototype system for new J-PARC LINAC LLRF system.



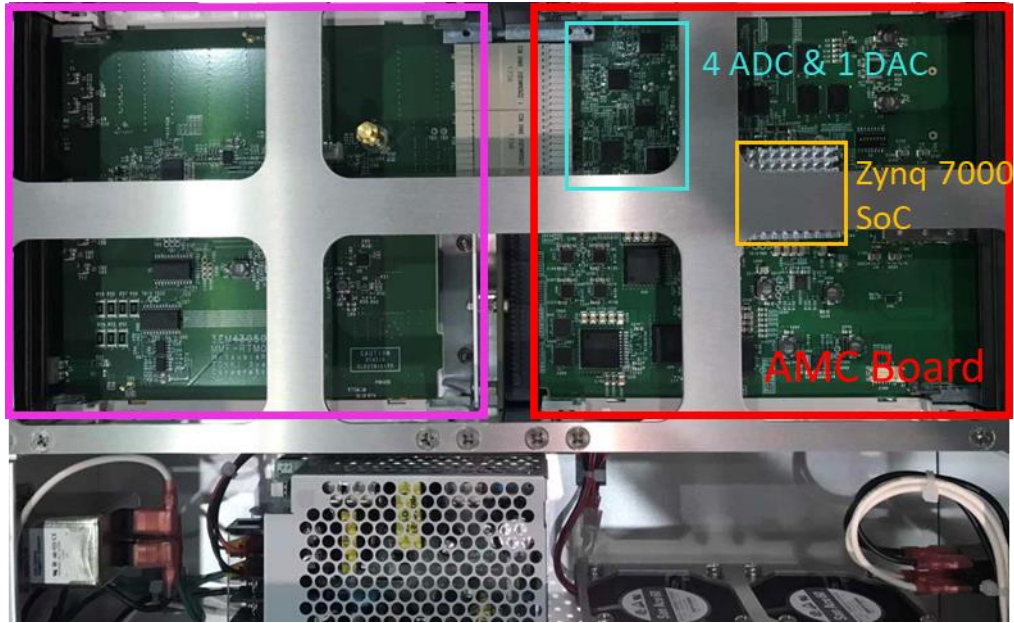


Figure 3.4. Digitizer Board

Various real-time signals in FPGA are sampled and sent to memory. These digital signals not only contain real-time process signals such as ADC input signals, vector sum signals, feed forward signals and DAC output signals but also parameter data such as rotation parameters, proportional integral parameters and IQ (In-phase and Quadrature) offset parameters and so on. In EPICS, the basic data element is PV (Process Variable). The Channel Access Protocol defines how process variable data is transferred between a server and a client. After coming out of low & medium speed monitor, these process variables are sent to CA (Channel Access) Server, namely IOC. The information of these process variables is stored in the EPICS database of IOC in the form of records. By calling these records using CA Clients, such as CSS (Control System Studio) software, we can monitor the FPGA signals in real time and change those parameters when we needed. In order to build an ILC loop, we install PyEpics software on Computer. PyEpics is a python EPICS package which provides several function, modules and classes to interact with EPICS Channel Access. By importing the PyEpics modules into the ILC program of python language, we can obtain and output the data of EPICS process variables in real time [9].

# Chapter 4

## Iterative Learning Control

This chapter mainly introduces the basic ILC theory to facilitate readers to understand the follow-up design scheme. What's more, two popular ILC method in LLRF control field, Norm-Optimal ILC and Iterative Extremum Seeking, will also be introduced.

Iterative Learning Control (ILC) is a powerful control tool for the dynamic systems with good repeatability. It can effectively improve the transient response of system even if the information of the controlled system is incomplete. The core idea of ILC is to continuously optimize the current system input by rationally using the information from the previous iterations and finally make the system output keep approaching the target value [10]. This requires the system to be controlled must be stable enough, so that the input and output information of past trials can be correctly used to formulate the input signal for the next trial. Obviously, this is not a difficult task for modern LLRF system with digital feedback control.

After more than three decades of development, ILC has already been a well-established area of study in control theory. There are many great ILC algorithms was put forward, such as High Order ILC (HOILC), Stochastic ILC (SILC), Norm Optimal ILC (NOILC) and  $H_\infty$ -ILC, etc. However, in this paper, we didn't use these ILC algorithms mentioned above but choose the first order P-type algorithm, or called classical "Arimoto-type", as the ILC scheme, in which P denotes proportion. The reasons for choosing this option are as follow: Firstly, after years of research, the first order P-type algorithm has more abundant theoretical basis than other algorithms, which is conducive to the analysis of experimental results. Secondly, as the simplest algorithm, it is very easy to implement, thus effectively shortening the project development cycle. At last, considering that the algorithm may be updated in the future, Arimoto-type as the most basic algorithm, its experimental results will be a very important reference object for future experimental results. In the following section, we will briefly introduce the characteristics of the first order P-type ILC.

## 4.1 ILC Basic Theory

Consider the following discrete-time linear time-invariant (LTI) system:

$$x_j(k+1) = Ax_j(k) + Bu_j(k) \quad (4.1)$$

$$y_j(k) = Cx_j(k) \quad (4.2)$$

where the subscript  $j$  denotes the iteration index, and  $k$  labels the time instant in an iteration trial, where  $k \in [0, N]$ , and  $N$  is the trial length.  $x_j(k)$ ,  $y_j(k)$  and  $u_j(k)$  represent the system state, output and input, respectively. Matrices  $A$ ,  $B$ , and  $C$  are system state matrix, input matrix, and output matrix respectively, with appropriate dimensions. And the relationship between input and output of a single input single output (SISO) system can be described by the following equation:

$$y_j(k) = h(q)u_j(k) + d(k) \quad (4.3)$$

where  $q$  is the forward time-shift operator with  $qx(k) \equiv x(k+1)$ , and  $d$  is an exogenous signal that is related to the initial state of the system and repeats every iteration [11]. The plant  $h(q)$  is a proper rational function of  $q$  with an equivalently relative degree of  $m$ . Assume for all  $j$ , the initial condition  $x_j(0) = x_0$ , then the equation (3) can be written as:

$$y_j(k) = C(qI - A)^{-1}Bu_j(k) + CA^kx_0 \quad (4.4)$$

here, we can easily get that,  $h(q) = C(qI - A)^{-1}B$  and  $d(k) = CA^kx_0$ .

For discrete-time ILC, each iteration signal consists of a finite number of discrete-time points. By using the lifting technique, those signals can be changed to the form of “supervectors”. Consider the following  $N$ -sampled sequence of inputs, outputs, references and errors at the  $j$ th iteration:

$$\begin{aligned} U_j &= [u_j(0), u_j(1), u_j(2), \dots, u_j(N-1)]^T \\ Y_j &= [y_j(m), y_j(m+1), y_j(m+2), \dots, y_j(N-1+m)]^T \\ Y_d &= [y_d(m), y_d(m+1), y_d(m+2), \dots, y_d(N-1+m)]^T \\ E_j &= Y_d - Y_j = [e_j(m), e_j(m+1), e_j(m+2), \dots, e_j(N-1+m)]^T \end{aligned}$$

where  $m$  is the delay, or relative degree of the system. With these definitions, the equation (3) can be described as:

$$Y_j = HU_j + D \quad (4.5)$$

where  $H$  is the system impulse response matrix, given by

$$H(A, B, C) = \begin{bmatrix} CB & 0 & 0 & \cdots & 0 \\ CAB & CB & 0 & \cdots & 0 \\ CA^2B & CAB & CB & \cdots & \vdots \\ \vdots & \vdots & \vdots & \ddots & 0 \\ CA^{N-1}B & CA^{N-2}B & CA^{N-3}B & \cdots & CB \end{bmatrix} \quad (4.6)$$

and the matrix

$$D(C, A, x_0) = \begin{bmatrix} Cx_0 \\ CAx_0 \\ CA^2x_0 \\ \vdots \\ CA^Nx_0 \end{bmatrix} \quad (4.7)$$

matrix  $H$  is a lower-triangular Toeplitz matrix whose elements are the Markov parameters of the controlled system. Matrix  $D$  shows the effect of system initial condition to the system output. Likewise, the first order P-type ILC update rule can also be expressed in the supervectors framework, such as

$$U_{j+1} = U_j + \Gamma E_j \quad (4.8)$$

where  $\Gamma = \text{diag}(\gamma)$  is Arimoto-like gain, means the learning gains are placed in diagonal terms of  $\Gamma$ . According to the definition of error,  $E_{j+1} = Y_d - Y_{j+1}$  and  $E_j = Y_d - Y_j$ , then combined with equation (5) and (8), we have

$$E_{j+1} - E_j = -Y_{j+1} + Y_j = -HU_{j+1} + HU_j = -\Gamma E_j \quad (4.9)$$

then we can get the error evolution law:

$$E_{j+1} = (I - H\Gamma)E_j \quad (4.10)$$

where, due to  $\Gamma$  is Arimoto-like gain,  $H\Gamma$  is a lower triangular matrix with the diagonal blocks being  $CB\Gamma$ . The error evolution law plays an important role in studying the convergence of ILC.

In ILC theory, two stability concepts are used to judge the convergence of ILC. The first one is Asymptotic Stability (AS), which is mainly concerned with whether the input or output of an ILC algorithm convergence to a limit value when the number of iterations approaches infinity. According to the ILC theory [7], when the ILC gain is Arimoto-type, the asymptotic stability condition is defined as

$$|1 - \gamma_{ii}h_1| < 1, i = 1, 2, \dots, n \quad (4.11)$$

where  $h_1$  is the first non-zero Markov parameter of system impulse response matrix. Obviously, equation (11) can also be written as  $|1 - \gamma_{ii}CB| < 1$ . When  $CB$  is known, it is not hard to find a suitable proportionality coefficient  $\gamma_{ii}$  to make system asymptotically stable.

The second concept is Monotonic Convergence (MC). It is mainly concerned with whether the error will become smaller and smaller as the number of iterations increases. From equation (10), we have

$$\|E_{j+1}\| = \|(I - H\Gamma)E_j\| \leq \|(I - H\Gamma)\| \|E_j\| \quad (4.12)$$

a sufficient condition for Monotonic Convergence is  $\|(I - H\Gamma)\|_i < 1$ , where  $i$  denotes different norm topology. In the 1-norm topology, the MC condition is  $\|(I - H\Gamma)\|_1 < 1$ , in the 2-norm topology is  $\|(I - H\Gamma)\|_2 < 1$ , and in the  $\infty$ -norm topology is  $\|(I - H\Gamma)\|_\infty < 1$ . In practice, since the parameters of the controlled system are difficult to change, in order to make the error convergence, we can only change the gain of the ILC. Because the ILC algorithm we chose is the first order P-type, the gain of ILC  $\gamma_{ii}$  is a proportionality coefficient, the value of  $\gamma_{ii}$  depends on the system transfer function. The experimental results also show that the error of the system can converge gradually with the increase of iteration times, as long as the gain of ILC is within this interval. As one of the most important parameters of ILC algorithm, we will continue to discuss the ILC gain in subsequent paragraphs.

## 4.2 ILC Scheme for J-PARC LINAC

In the J-PARC, the ILC update algorithm that was chosen to be used firstly is the P-type ILC. The reasons for choosing this option are as follow: Firstly, after years of research, the first-order P-type algorithm has more abundant theoretical basis than other algorithms, which is conducive to the analysis of experimental results. Secondly, as the simplest algorithm, it is very easy to implement, thus effectively shortening the project development cycle. At last, considering that the algorithm may be updated in the future, as the most basic algorithm, the experimental results of the first-order P-type ILC will be a very important reference object for future experimental results.

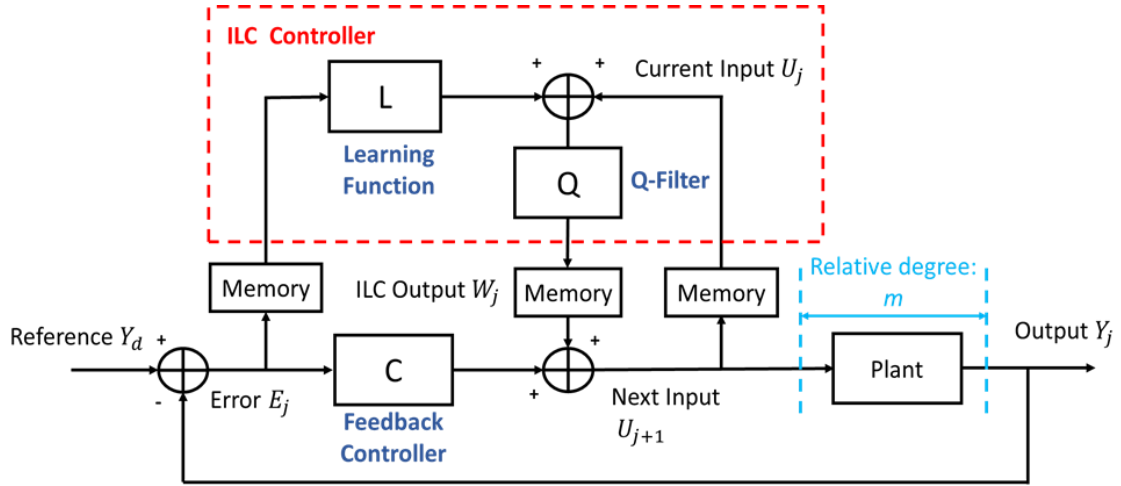


Figure 4.1. overall of ILC scheme for J-PARC LINAC.

The update equation of P-type ILC can be given by

$$u_{j+1} = u_j + k_p * e_j \quad (4.13)$$

where  $k_p$  is a proportional gain which range is between 0 and 1,  $e_j$  is the system error,  $u_j$  is the current input and  $u_{j+1}$  is the next input.

The block diagram of ILC scheme is shown in the Fig. 4.1. The subscript  $j$  denotes the iteration index.  $U_j$  is the system input signal;  $Y_j$  is the system output signal;  $E_j$  is the system error signal, and  $Y_d$  is the reference signal. C, L, and Q denote the feedback controller, learning function, and Q-filter, respectively. To suppress the non-repetitive

disturbances, a feedback control is needed. An ILC controller is thus used to counteract the effect of repetitive disturbance. In addition, during each iteration, the high-frequency noise components in the controlled plant will be accumulated with the system error and then added to the next system input by the ILC. This will degrade the system performance and sometimes result in oscillations. Thus, to address this problem, a low-pass Q-filter was added. The ILC algorithm can be represented as

$$u_{j+1}(k) = w_j(k) + C e_{j+1}(k) = Q[u_j(k) + L e_j(k + m)] + C e_{j+1}(k) \quad (4.14)$$

where  $k$  is the time instant in an iteration,  $m$  is the delay, or equivalently, relative degree of the plant, and this relative degree  $m$  can be compensated by a corresponding time shift of the error vector  $\Delta t_{in-out}$ . The input of the plant includes the feedforward component  $w_j(k)$ , which learns from previous iterations, and the current feedback component  $C e_{j+1}(k)$ . The ILC controller update algorithm is given by

$$w_j(k) = Q[u_j(k) + K_p * e_j(k + m)] \quad (4.15)$$

where  $K_p$  is the proportional gain or ILC gain. A simple moving average module was used as the low-pass Q filter. The window length and alignment position of the simple moving average algorithm are 3 and center, respectively. The algorithm for this simple moving average scheme is as follows

$$y_{sma}(k) = \frac{1}{3} [x_{sma}(k + 1) + x_{sma}(k) + x_{sma}(k - 1)] \quad (4.16)$$

where  $x_{sma}$  is the Q filter input and  $y_{sma}$  is the Q filter output.

### 4.3 Norm-Optimal Iterative Learning Control

In this chapter, we mainly introduce the calculation process of NOILC. For the proof of the convergence of NOILC and the theoretical foundations, please refer to [12].

Considering the state space model of discrete linear time-invariant systems

$$\begin{aligned} x(t + 1) &= Ax(t) + Bu(t), x(0) = x_0, 0 \leq t \leq N \\ y(t) &= Cx(t) \end{aligned} \quad (4.17)$$

where  $N$  is the number of samples,  $x(t)$  is the  $n \times 1$  state vector,  $y(t)$  is the  $m \times 1$  output vector and  $u(t)$  is the  $l \times 1$  control input vector. And because  $N$  is finite, introduce the supervectors

$$y = \begin{bmatrix} y(1) \\ y(2) \\ \vdots \\ y(N) \end{bmatrix}, \quad u = \begin{bmatrix} u(0) \\ u(1) \\ \vdots \\ u(N-1) \end{bmatrix} \quad (4.18)$$

then the system process dynamic can be described as

$$y = Gu + y(0) \quad (4.19)$$

where  $G$  is the  $m \times l$  system transfer matrix given by

$$G = \begin{bmatrix} CB & 0 & \dots & 0 \\ CAB & CB & \dots & 0 \\ \vdots & \vdots & \ddots & \vdots \\ CA^{N-1}B & CA^{N-2}B & \dots & CB \end{bmatrix} \quad (4.20)$$

And

$$y_0 = [(CA)^T \ (CA^2)^T \ \dots \ (CA^N)^T]^T x_0 \quad (4.21)$$

The matrix  $G$  could be of very large dimensions, but this is not a problem as it does not appear in the final calculations. The goal of the NO-ILC is to generate a control signal at the  $k + 1$  iteration  $u_{k+1}$  to minimize the performance index given by

$$J_{k+1}(u_{k+1}) = \|e_{k+1}\|^2 + \|u_{k+1} - u_k\|^2 \quad (4.22)$$

where  $e_{k+1} = r - y_{k+1}$  and  $r$  is the desired trajectory of the output, and  $\|\cdot\|$  represents the appropriate norms. Writing the norms out as sums gives the performance index as



$$J_{k+1}(u_{k+1}) = \frac{1}{2} (\sum_{t=1}^N (r(t) - y_{k+1}(t))^T Q (r(t) - y_{k+1}(t)) + \sum_{t=0}^{N-1} (u_{k+1}(t) - u_k(t))^T R (u_{k+1}(t) - u_k(t))) \quad (4.23)$$

where the weighting matrices  $Q$  and  $R$  is of compatible dimensions, and symmetric positive definite. The control input on trial  $k + 1$  that minimizes the cost function here is obtained from the stationary condition

$$\frac{\partial J_{k+1}}{\partial u_{k+1}} = -G^T Q e_{k+1} + R(u_{k+1}(t) - u_k(t)) = 0 \quad (4.24)$$

or, since  $R$  is invertible,

$$u_{k+1} = u_k + R^{-1} G^T Q e_{k+1}, \forall k \geq 0 \quad (4.25)$$

However, this control law cannot be implemented. To obtain an implementable form of this algorithm, first note that the adjoint (or transpose) for the class of plants considered here involves the operations of time reversal plus an appropriate change of the state-space parameters. Hence in

$$u_{k+1} - u_k = G^* e_{k+1} = R^{-1} G^T Q e_{k+1} \quad (4.26)$$

the adjoint operator  $G^*$  becomes the costate system

$$\begin{aligned} \xi_{k+1}(t) &= A^T \xi_{k+1}(t+1) + C^T Q e_{k+1}(t+1), \\ \xi_{k+1}(N) &= 0 \\ u_{k+1}(t) &= u_{k+1}(t) + R^{-1} B^T \xi_{k+1}(t), 0 \leq t < N \end{aligned} \quad (4.27)$$

This system has a terminal condition at  $t = N$  instead of an initial condition, marking it (as expected) as an anti-causal representation of the solution. It cannot therefore be implemented in this form, but a causal implementation can be found when assuming full state knowledge. The optimal control is transformed by writing for the costate

$$\xi_{k+1}(t) = \left[ -k(t)(I + BR^{-1}B^TK(t))^{-1}A(x_{k+1}(t) - x_k(t)) \right] + \zeta_{k+1} \quad (4.28)$$

and then using these last two equations and standard techniques in optimal control theory to show that the matrix gain  $K(t)$  is the solution of the familiar discrete matrix Riccati equation on the interval  $[0, N - 1]$

$$\begin{aligned} K(t) = & A^TK(t+1)A + C^TQC \\ & - [A^TK(t+1)B(B^TK(t+1)B + R)^{-1}B^TK(t+1)A] \end{aligned} \quad (4.29)$$

with terminal condition  $K(N) = 0$ . Also the predictive or feedforward term is generated by

$$\begin{aligned} \xi_{k+1}(t) = & (I + K(t)BR^{-1}B^T)^{-1}(A^T\xi_{k+1}(t+1) + C^TQe_k(t+1)) \\ \xi_{k+1}(N) = & 0 \end{aligned} \quad (4.30)$$

and the input update equation now is

$$\begin{aligned} u_{k+1}(t) = & u_k(t) - \left[ (B^TK(t)B + R)^{-1}B^TK(t)A(x_{k+1}(t) - x_k(t)) \right] \\ & + R^{-1}B^T\xi_{k+1}(t) \end{aligned} \quad (4.31)$$

This representation of the solution is causal because it can be solved offline, between trials, by reverse time simulation using available previous trial data.

# Chapter 5

## ILC Simulation Test on MATLAB

In order to verify the effectiveness of ILC, firstly, a simulation model of low-level radio frequency system was built in MATLAB. Then, after verifying the reliability of the LLRF module, the ILC control loop was built on its basis. In this chapter, the design scheme of the simulation modules will be introduced. The simulation results will be discussed and evaluated.

### 5.1 Design Scheme of ILC Simulation Model

A classic LLRF control system model, as shown in the Fig. 5.1, mainly consists of the following components: input, output, reference signal module, cavity module, transport delay module, PI controller module and beam loading module. In our case, a pulse signal with a period of 500  $\mu\text{s}$  and pulse width of 200  $\mu\text{s}$  was generated by the input model. The structure of beam loading module and reference signal module are basically the same as the input module, which has a pulse generator in it. Beam loading model will make a rectangular depression at the flat top of the input pulse waveform.

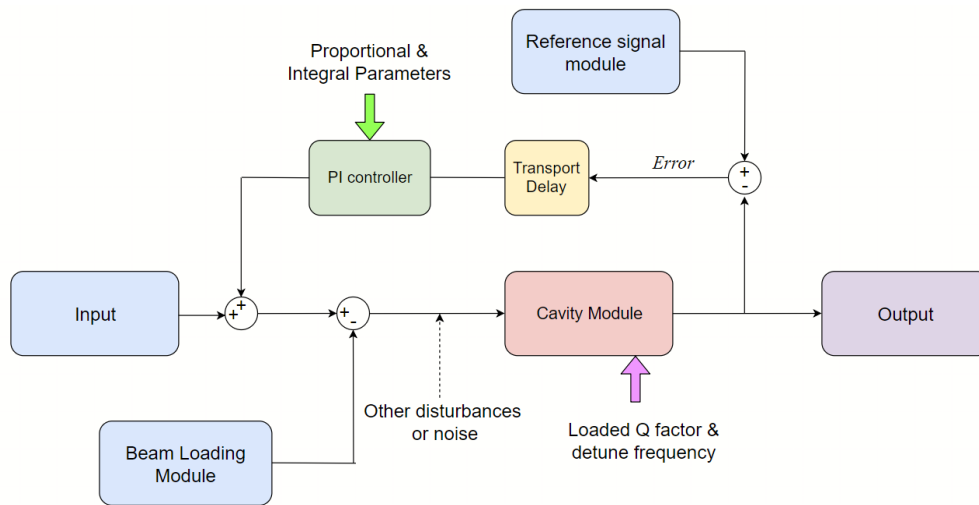


Figure 5.1. Block diagram of LLRF system model

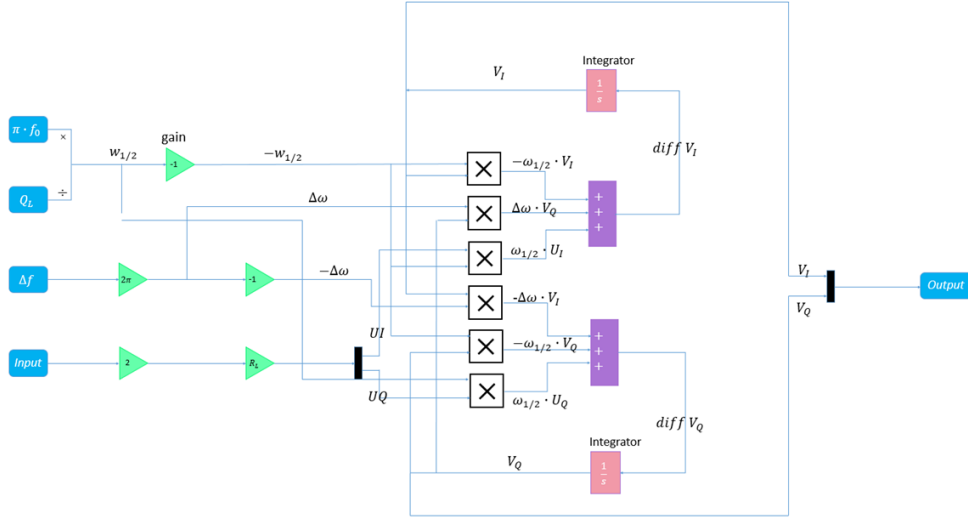


Figure 5.2. The architecture of cavity model.

The architecture of cavity model is shown in the Fig. 5.2. The design of cavity module is according to the following state space equation,

$$\frac{d}{dt} \begin{bmatrix} V_{cr} \\ V_{ci} \end{bmatrix} = \begin{bmatrix} -\omega_{1/2} & -\Delta\omega \\ \Delta\omega & -\omega_{1/2} \end{bmatrix} \begin{bmatrix} V_{cr} \\ V_{ci} \end{bmatrix} + \omega_{1/2} R_L \begin{bmatrix} I_r \\ I_i \end{bmatrix} \quad (5.1)$$

where  $V_c$  is the cavity voltage,  $I$  is the driving current,  $\Delta\omega$  is the detune frequency,  $\omega_{1/2}$  is the half bandwidth of the cavity and  $R_L$  is the equivalent resistance of the cavity [13]. And half bandwidth  $\omega_{1/2} = \frac{\omega_0}{2Q_L} = \frac{1}{\tau}$ ,  $\omega_0$  is the resonance angular frequency,  $Q_L$  is the loaded quality factor and  $\tau$  is the time constant of cavity. By entering different loaded Q factor and detune frequency we can get different cavity models. For our normal conducting cavity, detune frequency is almost zero. And in this simulation test, the loaded quality factor is set to 13970, which is the measured value of a cavity that only for testing. Output model can help us check the experiment results. In feedback control loop, since the actual feedback loop has a certain delay, we added a delay module to the simulation loop to simulate the actual situation. Error  $e(t)$  was calculated by subtracting the output value from the reference value. Then this error will pass through the PI controller model, which control function can be expressed mathematically as

$$u_t = k_p * e(t) + k_i \int_0^t e(t) dt \quad (5.2)$$

where  $k_p$  is the proportional coefficient and  $k_i$  is the integral coefficient. We can compensate for the deformation caused by the beam loading effect well by choosing the appropriate  $k_p$  and  $k_i$  parameters. In the Fig 5.3, (a) and (b) show the output waveforms when the feedback is turned off and on, respectively. The simulation results are very similar to the actual results both in amplitude and phase. This means that we can start to build an ILC control loop on this basis.

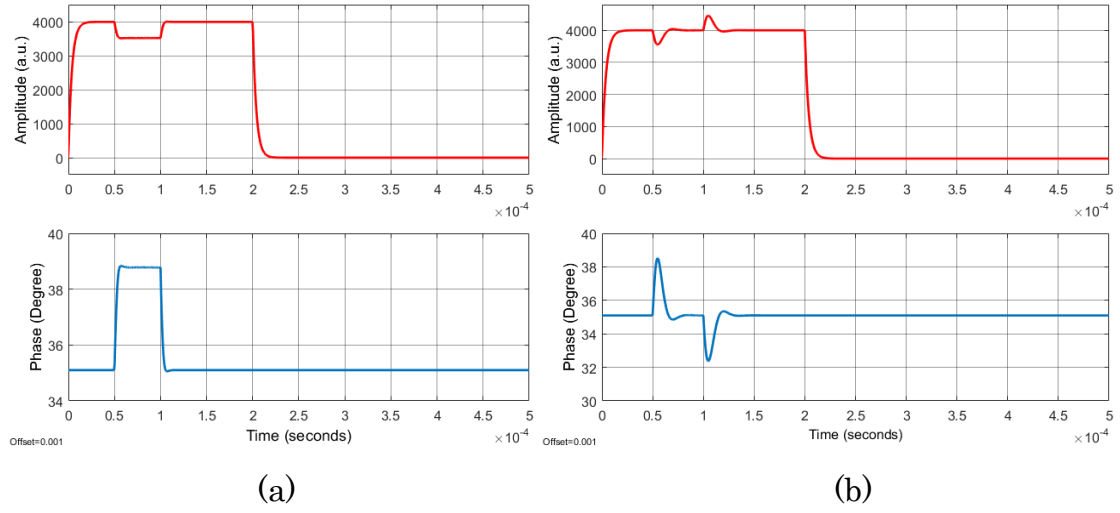


Figure 5.3. Amplitude & Phase Waveform of the simulation system output with beam loading when feedback is off (a) and on (b).

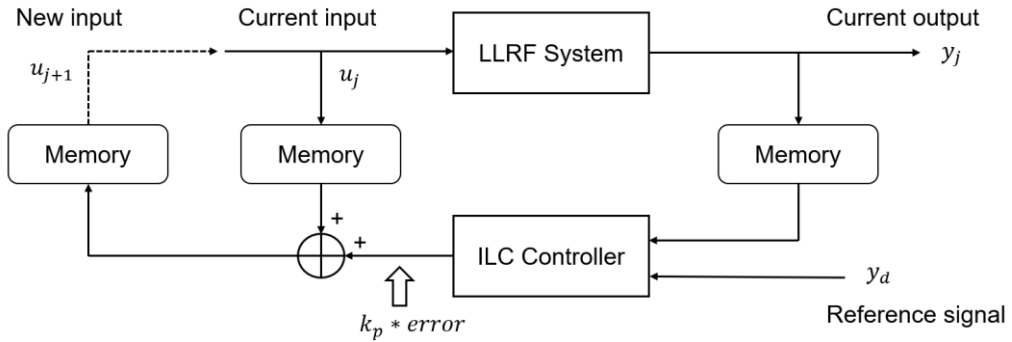


Figure 5.4. Block diagram of ILC loop.

According to the definition of ILC algorithm, the design scheme of ILC loop is shown in the Fig 5.4. The original LLRF system model is packaged into a submodule of the ILC loop, as the plant of ILC algorithm. The original input in the LLRF system model remains unchanged during ILC operation. The goal of this input is to build a basic accelerating field in cavity. In the actual LLRF system, such data is stored in a feedforward table called FF\_BASE. For the input of ILC algorithm, its goal is to compensate for the depression caused by the beam loading effect.

The architecture of ILC scheme model is shown in the Fig 5.5. As the number of iterations increases, the input of ILC is constantly updated until the tracking error is reduced to an acceptable range. We store this dynamic input in a feedforward table called FF\_BEAM. The sum of FF\_BASE, FF\_BEAM, output of PI controller and the beam loading module are the actual input of the cavity. The error signal used in the ILC loop is consistent with the error signal used in the feedback loop. In the simulation process, all input and output data are stored in the workspace of MATLAB. The function of the workspace is the same as the memory in the actual system.

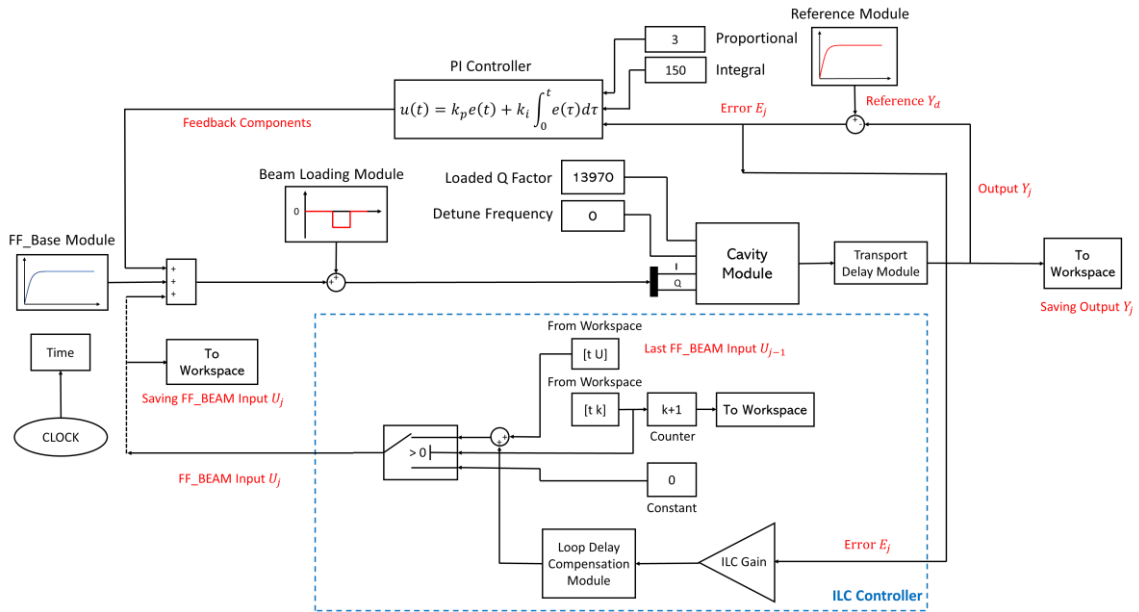


Figure 5.5. Block diagram of ILC simulation scheme.

The design of ILC controller follow the update equation of P-type ILC algorithm (Eq. 15). In the ILC controller, firstly, the error signal is multiplied by the ILC gain, then passing through the loop delay compensation module to adjust the time shift of error,

which value is  $\Delta t_{in-out}$ . The sum of current processed error signals and the last feedforward data saved in the FF\_BEAM table is the next output of ILC controller. At each iteration, feedforward value in the FF\_BEAM table will be saved into workspace. The switch in the ILC controller connect to a counter to ensure the timing is correct.

## 5.2 Analysis of Simulation Results

In the ILC control, there are three important components which will affect the results of experiment: ILC gain, the time shift of error (loop delay compensation module) and Q filter. In this simulation, due to the noise from the output signals was basically filtered out by the cavity itself, so no Q filter was added in the front of switch here.

### 5.2.1 ILC Parameters: Time Shift of Error

Among these three parameters, the most important one is the time shift of error. If there is no compensation, the position of the feedforward may fail to align the deformation part caused by the beam loading. In the J-PARC LINAC, the system loop delay  $T_{loop}$  is usually several microseconds. In the delay module, the loop delay  $T_{loop}$  is a positive value. To counteract the effect of loop delay, the value of time shift of error  $\Delta t_{in-out}$  is set to a negative value. The sum of loop delay  $T_{loop}$  and the time shift of error  $\Delta t_{in-out}$  can be given by

$$\Delta t = T_{loop} + \Delta t_{in-out} \quad (5.3)$$

The value of  $\Delta t$  can reflects the degree of alignment of feedforward and deformation of waveform.

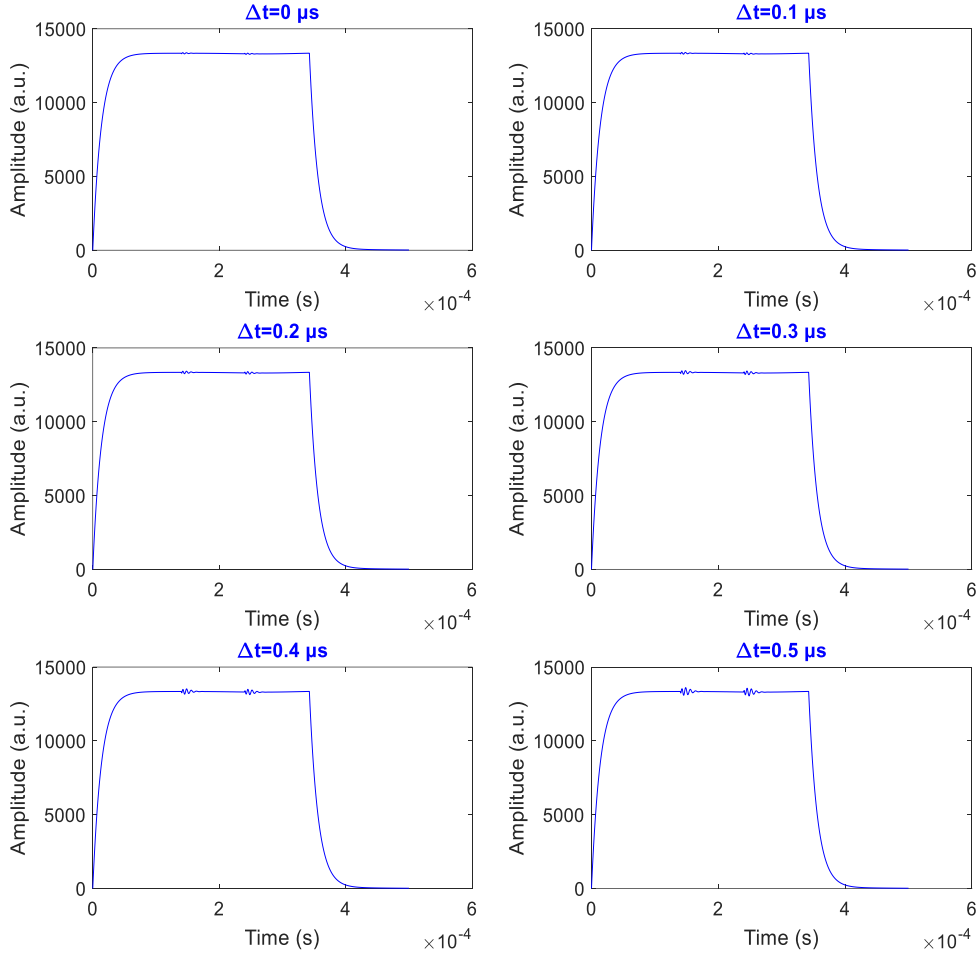


Figure 5.6. Effect of time shift of error to the final cavity output waveform.

Figure 5.6 shows the effect of time shift of error to the final cavity output waveform. Here the iteration run 50 times. In order to shorten the compensation process, the ILC gain was set to 0.9. When  $\Delta t = 0 \mu s$ , the loop delay is well compensated. When  $\Delta t$  is gradually increased, the gap between the feedforward and the deformation of waveform is getting wider and wider, the oscillation at the flat top of the waveform becomes more and more obvious.



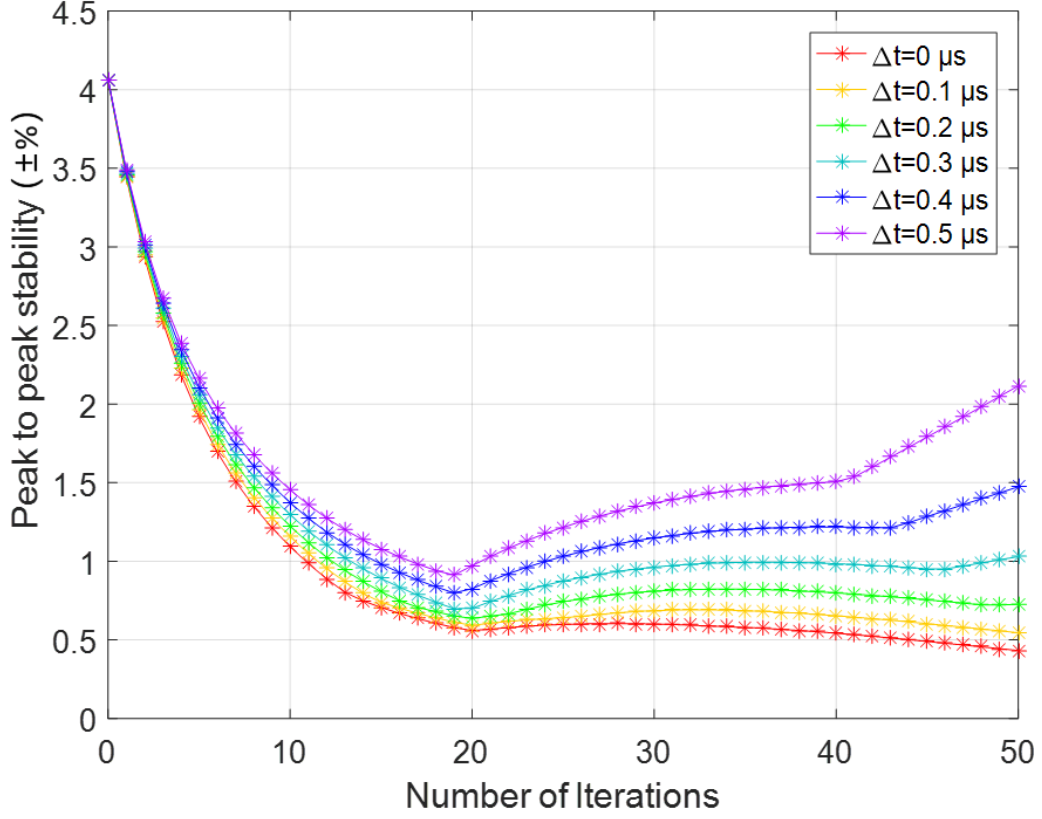


Figure 5.7. Effect of time shift of error to the results.

The effect of time shift of error to the amplitude peak to peak stability during 50 iterations is shown in the Fig. 5.7. When  $\Delta t = 0 \mu s$ , the peak to peak stability is gradually convergence during 50 iterations. When  $\Delta t = 0.1 \mu s$ , the stability curve is at its critical point. When  $\Delta t$  is equal to or larger than  $0.3 \mu s$ , obvious divergence curves can be observed, which will greatly affect the long-term operation of the accelerator. To achieve the required peak to peak stability of RF field, it is very important to choose an appropriate time shift of error  $\Delta t_{in-out}$  to minimize the value of  $\Delta t$  before conducting ILC.

### 5.2.2 ILC Parameters: ILC Gain

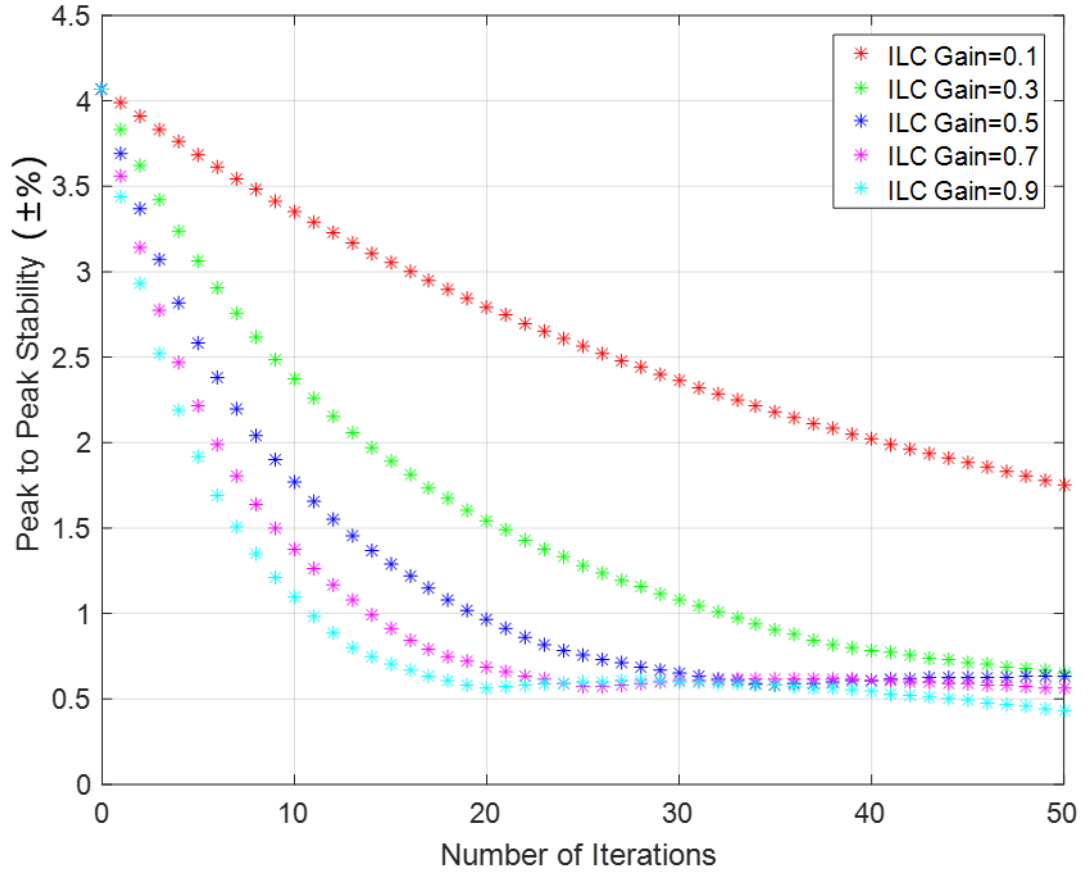


Figure 5.8. Effect of ILC gain to the amplitude peak to peak stability.

Figure 5.8 shows the effect of ILC Gain to the amplitude peak to peak stability during 50 iterations. Here, in order to get the best performance,  $\Delta t$  was set to 0. In the P-type ILC algorithm, ILC gain is a proportional parameter which range is larger than 0 and less than 1. During 50 iterations, compared to the smaller gain such as 0.1, choosing the larger gain, like 0.9, can help to achieve better peak to peak stability. And obviously, it also helps shorten the time required to complete the compensation process.

### 5.2.3 Simulation Results

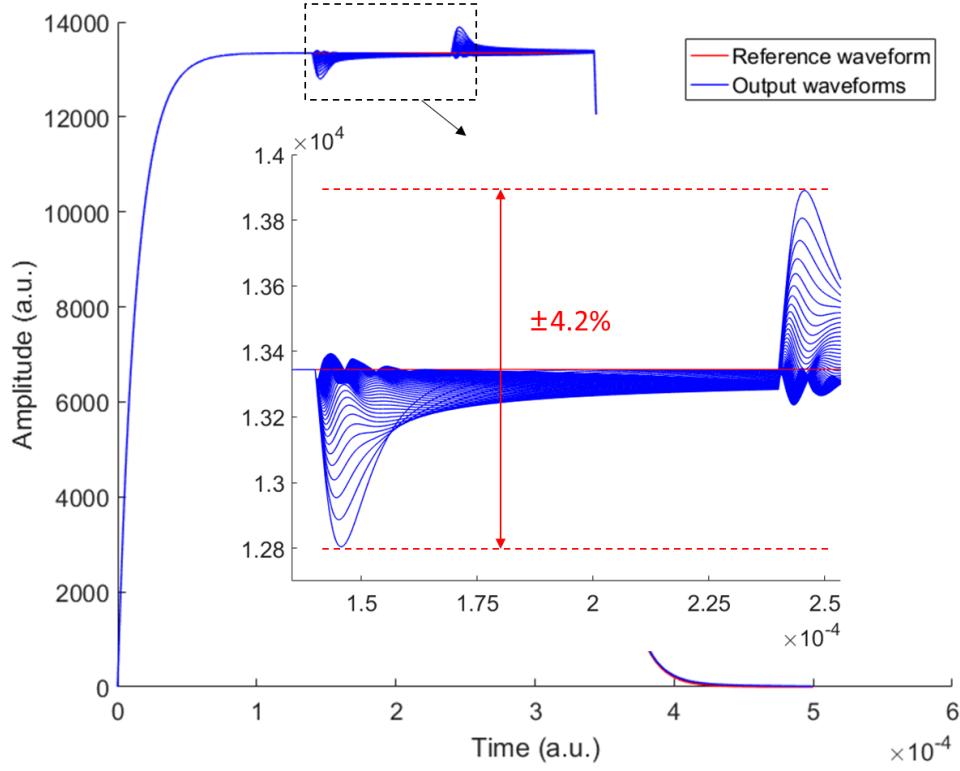


Figure 5.9. Cavity output amplitude waveforms during 50 iterations.

Figure 5.9 shows all the cavity output waveforms during 50 iterations. The ILC gain is set to 0.9. The loop delay is well compensated by the time shift of error. When there is only feedback works, the peak to peak stability of amplitude is  $\pm 4.2\%$ . As the increasing of the number of iterations, the deformation of the output waveform was gradually suppressed.

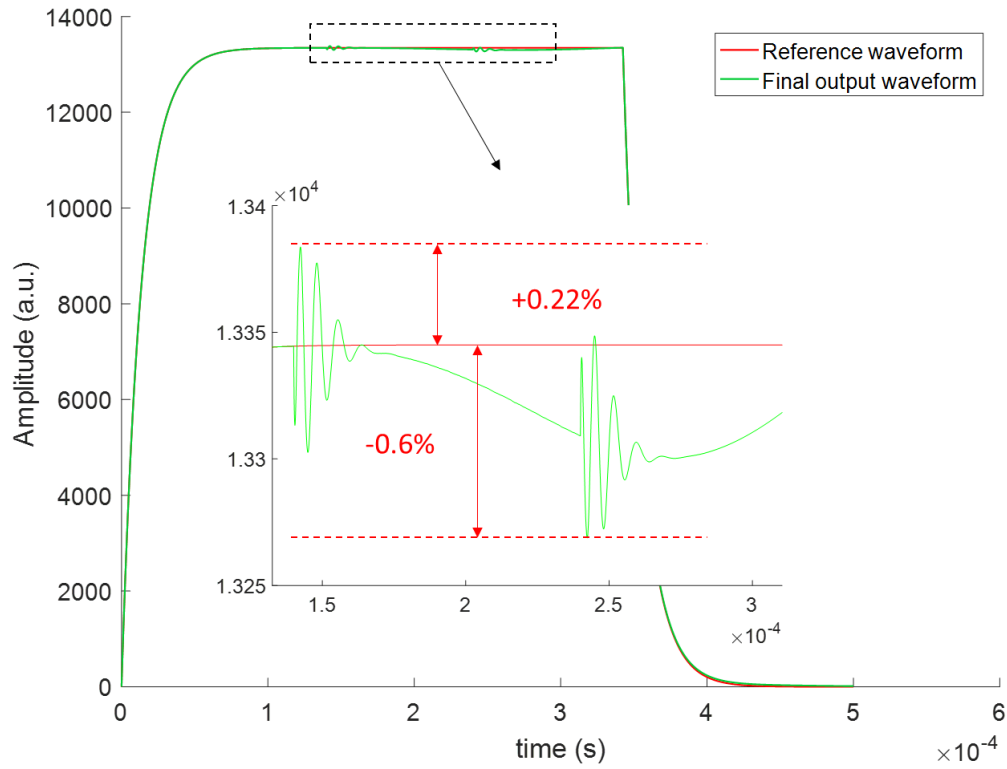


Figure 5.10. Final cavity output amplitude waveform after 50 iterations.

Figure 5.10 shows the final cavity output waveform after 50 iteration, namely, the final waveform in the figure 31. The red line is the reference waveform. The beam range is from 140  $\mu\text{s}$  to 240  $\mu\text{s}$ . After 50 iterations, the peak to peak stability of amplitude improves from  $\pm 4.2\%$  to  $-0.6\%$  to  $+0.22\%$ .

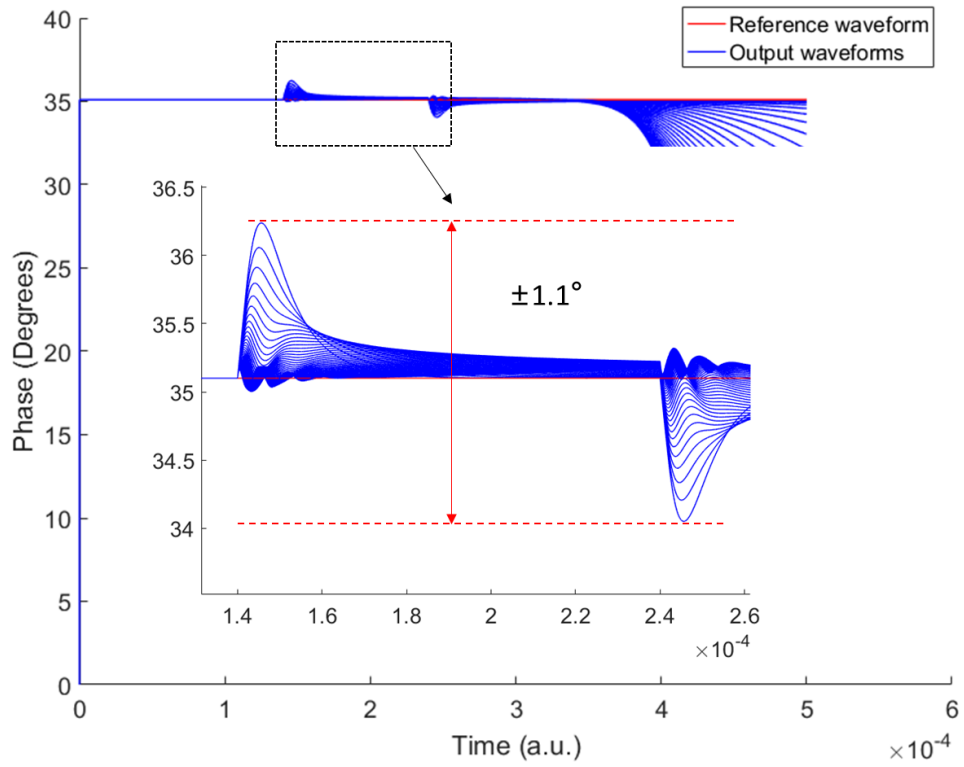


Figure 5.11. Cavity output phase waveform during 50 iterations.

All the phase waveform of cavity output signals during 50 iterations are shown in the Fig 5.11. Before the ILC start, the peak to peak stability of phase is  $\pm 1.1^\circ$ . During the iterations, the deformation of phase waveform at the beam range was gradually suppressed.

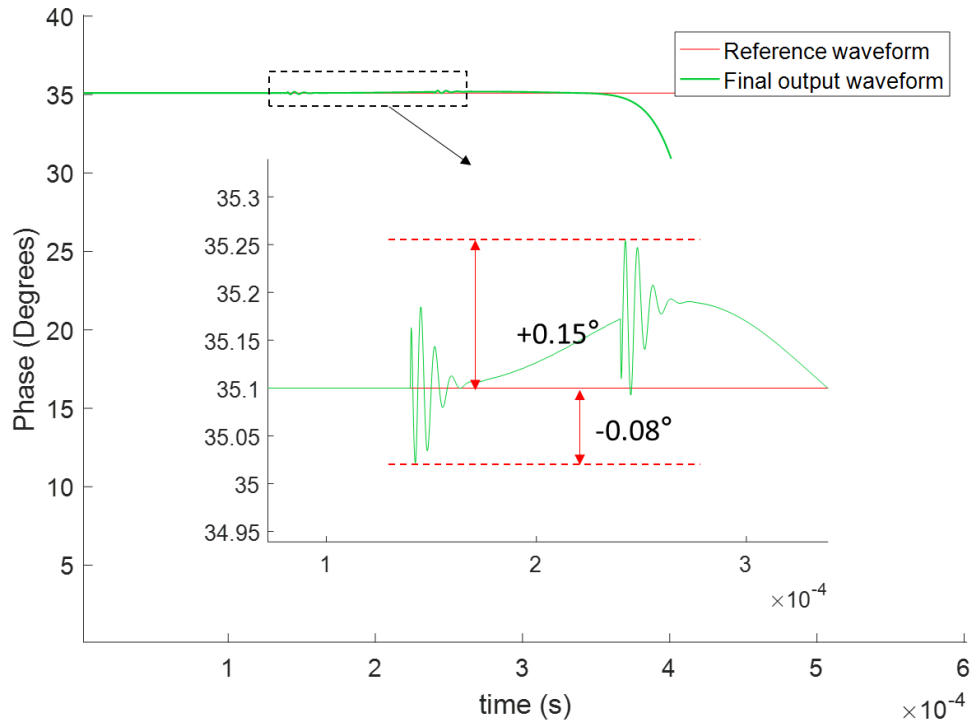


Figure 5.12. Final cavity output phase waveform after 50 iterations.

Figure 5.12 shows the final phase waveform of cavity output signal after 50 iterations. After 50 iterations, compare to the case of only feedback works, the inclusion of ILC controller improves the peak to peak stability from  $\pm 1.1^\circ$  to  $+0.15^\circ$  to  $-0.08^\circ$ .

### 5.3 Conclusion for ILC Simulation

To verify the effectiveness of ILC scheme. An ILC based LLRF system simulation model was built in the Simulink environment. All the simulation parameters are got from the real case of J-PARC LINAC system. The function of two significant parameters, ILC gain and the time shift of error were illustrated, which provides a theoretical basis for subsequent actual experiments. The simulation performances show that compared to the case that only feedback control works, after the inclusion of ILC controller, the peak to peak stability of amplitude was increased from  $\pm 4.2\%$  to  $-0.6\%$  to  $+0.22\%$ , phase stability was increased from  $\pm 1.1^\circ$  to  $+0.15^\circ$  to  $-0.08^\circ$ . The

simulation results show that ILC is a powerful control tool for the beam loading compensation.

## Chapter 6

# The Hardware and Software Setup for Beam Loading Compensation Experiment

### 6.1 Introduction of ILC Based Beam Loading

#### Compensation Experiment

The relationship between the feedback loop and the ILC loop of LLRF system is shown in the [Fig 6.1](#). Feedback control is accomplished in FPGA, while ILC is accomplished in computer through EPICS. As we mentioned before, there are two feed-forward input table in our system. The goal of FF\_BASE is to build a basic accelerating field and FF\_BEAM is to compensate the deformation of basic accelerating field caused by the beam loading. When the system is in an open loop state, the input of the system is the sum of the two. In order to ensure the stability of the field, the data in FF\_BASE is usually fixed. For the current system, due to the deformation caused by the beam is very similar to the rectangle, the data in FF\_BEAM is a fixed rectangular waveform. For the new system, the ILC method is used to compensate the beam loading, during ILC running, the data in FF\_BEAM will be constantly updated with the iterative process and finally approaching the ideal value. The contents in the red dotted line frame show the EPICS communication process of ILC. The signal in the FPGA is sampled by 96 MHz clock signal in real time and saved as PV in the IOC of EPICS. As a CA Client, there is an ILC controller which is designed by the Python programming language in computer. The data of these PVs can be acquired and changed by using this ILC controller. According to the update rule of P-type ILC, the data of current FF\_BEAM input  $U_j$  and system error  $E_j$  will be sent to ILC controller. After calculation, the ILC controller will replace the current FF\_BEAM data with the new data as the next FF\_BEAM input. This process is called completing an iteration. In order to achieve better experimental results, we improved the ILC controller on the



basis of the update rule of classical P-type ILC in the actual experiment process. Its structure is described in detail below.

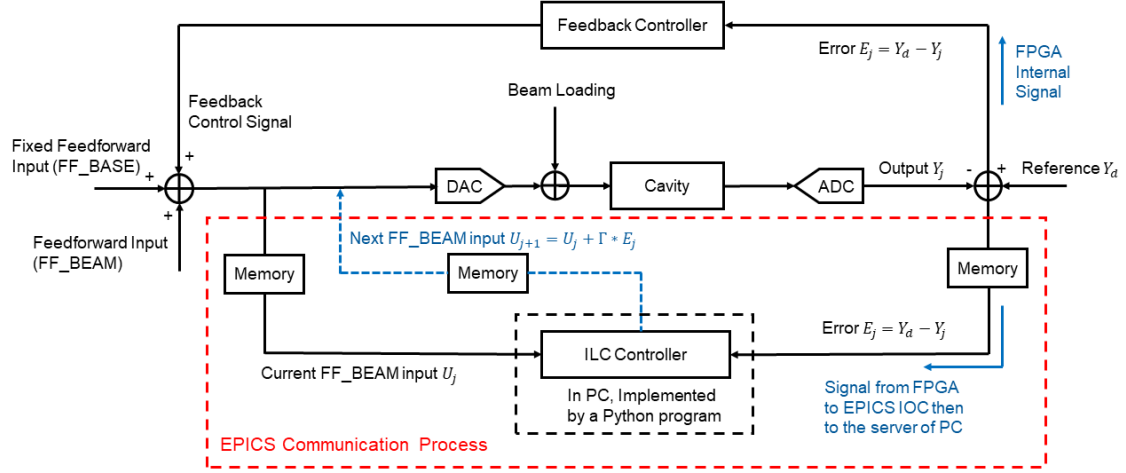


Figure 6.1. Architecture of feedback loop and ILC loop.

## 6.2 Software Setup

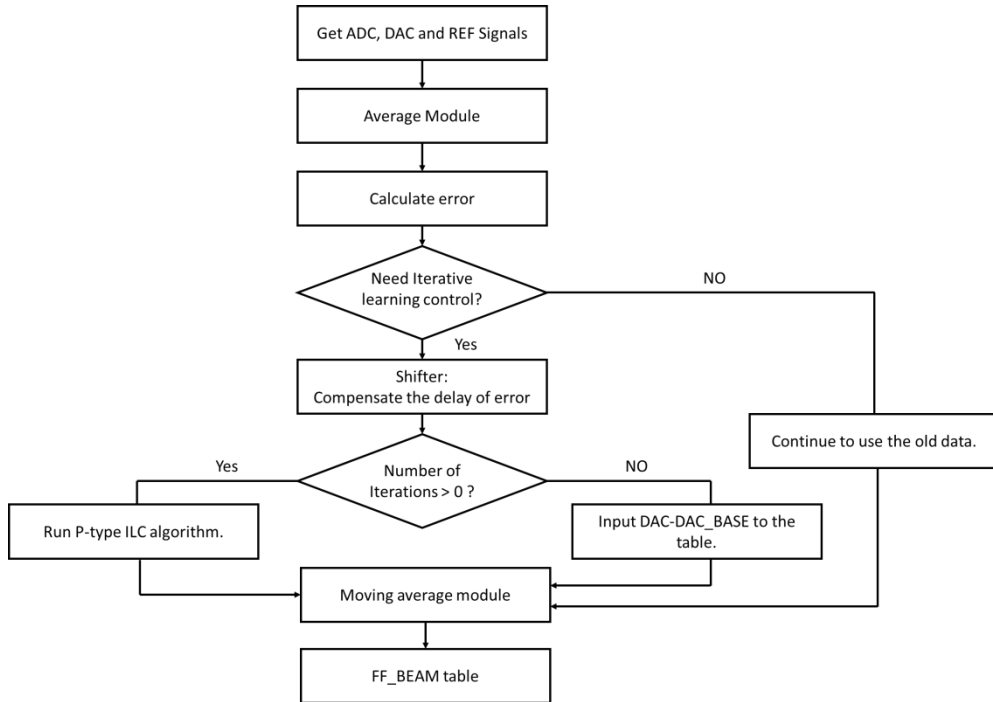


Figure 6.2. Program flowchart in ILC controller

Figure 6.2 shows the program flowchart in ILC controller. To reduce white noise in the ADC signal, an average filter was designed in the program. However, in the actual experiment, we found that because the sampling frequency of the system (96 MHz) is much higher than the frequency of the beam (2.5 Hz), the ADC signals under the same beam condition is sampled many times. The eight sets of ADC data input to the average filter to be identical. This makes the average filter unable to perform its proper function. In order to acquire different ADC signals each time, we add a comparator in front of the average filter. Only when the current sampled signal is different from the previous one, then this signal will be sent to the accumulator as one of the inputs of the average filter. After sampling eight different ADC signals, we can get an output of the average filter. Then by making a difference with the reference signal, we can get the system error. Since ILC is to compensate for the waveform deformation caused by the beam loading, we are mainly concerned with the error information at the flat top of the waveform. We take two sets of data with the same data length  $N$ , *flattop\_adcavg* and *flattop\_ref*, at the same position on the flat top of ADC waveform and reference waveform, respectively. The Root Mean Square Error (RMSE) of the system can be obtained by

$$\text{rmse} = \sqrt{\frac{\sum_{i=2}^N (\text{flattop\_ref} - \text{flattop\_adcavg})^2}{N}}. \quad (6.1)$$

And the Peak to Peak error of the system can be obtained from

$$\text{ppe} = \max(\text{flattop\_adcavg}) - \min(\text{flattop\_adcavg}) \quad (6.2)$$

where the function of  $\max(\cdot)$  is to return the item with the highest value and  $\min(\cdot)$  is to return the item with the lowest value. All the data in the list of *flattop\_ref* is the same constant value, if we define this constant value as *refamp* which represents the amplitude at the flat top of reference waveform, then we can get  $\text{RMS stability} = \text{rmse} / \text{refamp}$  and  $\text{Peak to Peak stability} = \text{ppe} / \text{refamp}$ . The value of RMS stability and Peak to Peak stability were used as criteria for judging whether ILC is executed or not.

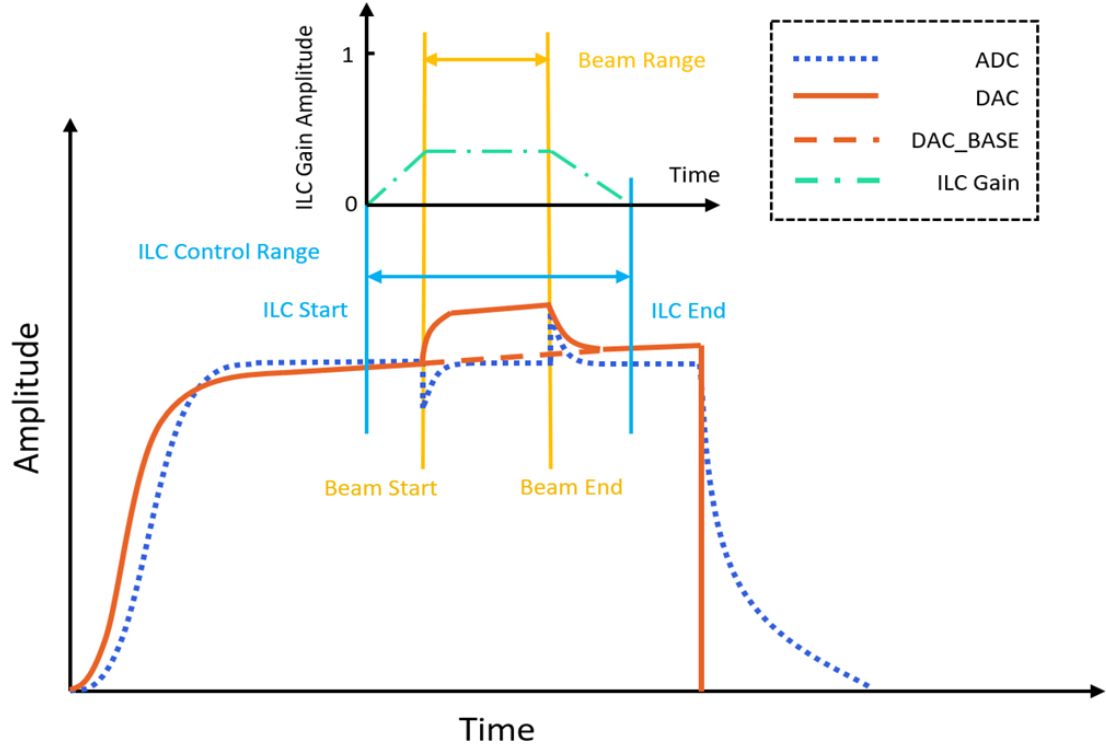


Figure 6.3. Schematic diagram of ADC, DAC and DAC\_BASE waveforms under feedback control in J-PARC LINAC

When the stability does not meet the requirements, the ILC switch is turned on. In our case, the beam current in J-PARC LINAC is 50 mA. The heavy beam loading makes the depression on the waveform very deep. In the case of only ILC, it usually takes many iterations to complete the compensation process, which is very time consuming. In order to reduce the depth of this depression, an initial feedforward data needs to be added to the system input. Figure 6.3 shows the schematic diagram of ADC, DAC and DAC\_BASE waveforms under feedback control in J-PARC LINAC. Among them, ADC and DAC are the waveforms with beam, and DAC\_BASE is the DAC waveform without beam. Because the power supply of J-PARC LINAC uses capacitor banks, there is a voltage drop on the ADC waveform when feedback control is off. When the feedback switch is turned on, to compensate this voltage drop, as the input, the DAC waveform becomes the waveform shown in the figure. Similarly, in order to compensate for the deformation caused by the beam loading, under the feedback control, there is a rising portion at the flat top of the DAC waveform. The feedforward we mentioned

above can be obtained by subtracting DAC\_BASE from DAC. What's more, in order to ensure the stability of ILC, we need to compensate for the ILC loop delay for the error signal by using a shifter.

After completing these two preparations, we can start updating the feedforward table. In the first iteration, we add the prepared initial feedforward and an error-related compensation data, which is the product of ILC gain and error, into the FF\_BEAM table. In subsequent each iteration, according to the P-type ILC update rule, the next FF\_BEAM input equals to the sum of current FF\_BEAM and the product of the ILC gain and the current error. In addition, to reduce the influence of ILC on the output waveform outside the beam range, the ILC gain value outside the beam range should gradually decrease.

## 6.3 Hardware Setup

The experiment site is the SDTL01 station in the 324 MHz low- $\beta$  section. [Figure 6.4](#) shows the system hardware setup for the beam loading compensation experiment. Due to the ILC control loop was mainly realized in the digitizer, the current LLRF system need to connect to it firstly. The system architecture is consistent with Fig. 3.1. Current LLRF system provides reference signal, LO (local oscillator) signal, clock signal and various gate signals. All the control processes were completed in the digitizer. And all the feedback and ILC control parameters can be adjusted in real-time by using the computer.

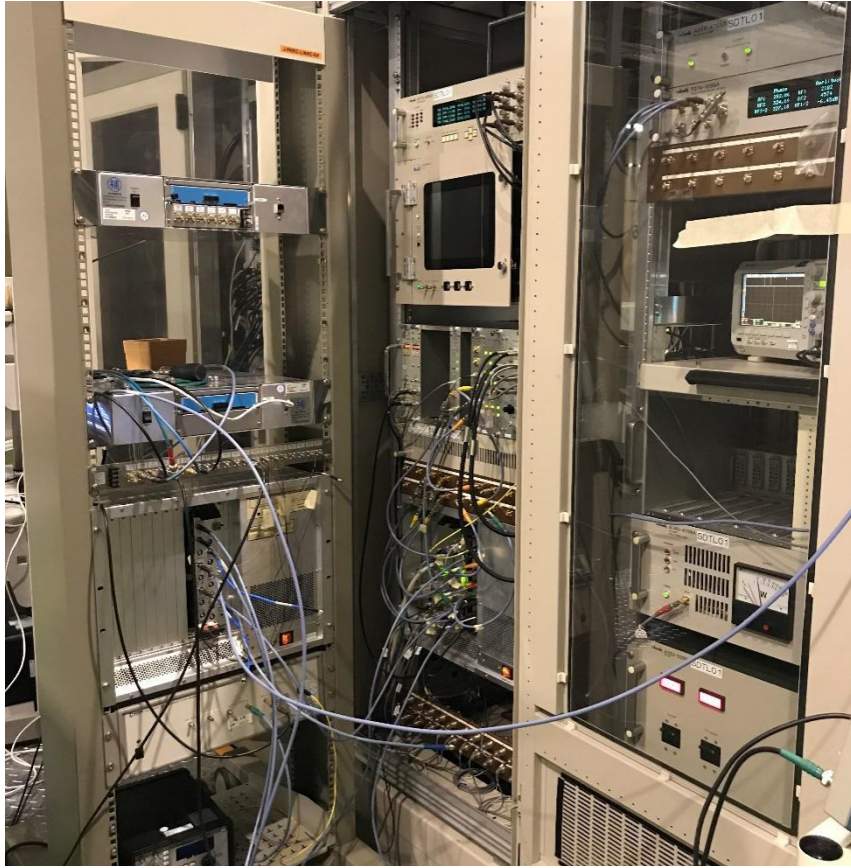


Figure 6.4. LLRF system setup for beam loading compensation experiment.

## Chapter 7.

# Experimental Results for Beam Loading Compensation

### 7.1 Experimental Results in SDTL01 Station

The experiment was conducted in the SDTL01 station [14]. The beam current was 50 mA. The beam pulse length is 100  $\mu$ s. For reducing the beam losses in the RCS, there is an RF chopper between the RFQ (Radio Frequency Quadrupole) and the DTL (Drift-Tube Linac) in J-PARC LINAC. Figure 7.1 shows the time structure of the linac beam pulse. The chopping ratio is about 56% and the chopping frequency is 1.23 MHz in accordance with the RF frequency of the RCS [15]. For the reason of this chopped beam noise, the RF waveform at the beam position becomes similar to the sawtooth wave. In the first test, for safety, the ILC gain  $k_p$  is set to 0.5. The time shift of error  $\Delta t_{in-out}$  is 4.16  $\mu$ s. The alignment position of SMA algorithm is center and window length equals to 3. The average number is 8.

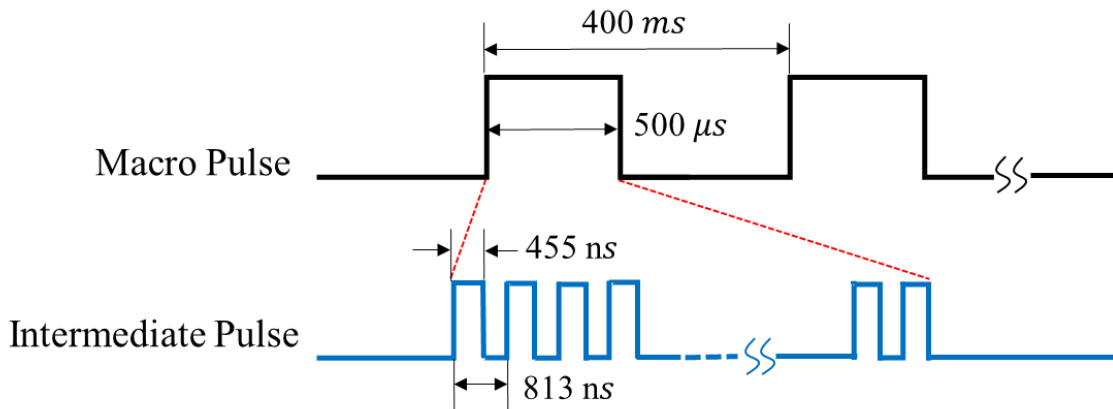


Figure 7.1. The time structure of the linac beam pulse.

After compensating for the loop delay well, the iteration was run 50 times. Figure 7.2 shows the ADC amplitude waveforms during 50 iterations. The initial waveform corresponds to the case of only feedback control. As the number of iterations increasing, the waveform became flattening gradually. Compared to the first and last results, the amplitude peak to peak stability was improved from  $\pm 4.1\%$  to  $\pm 0.37\%$ .

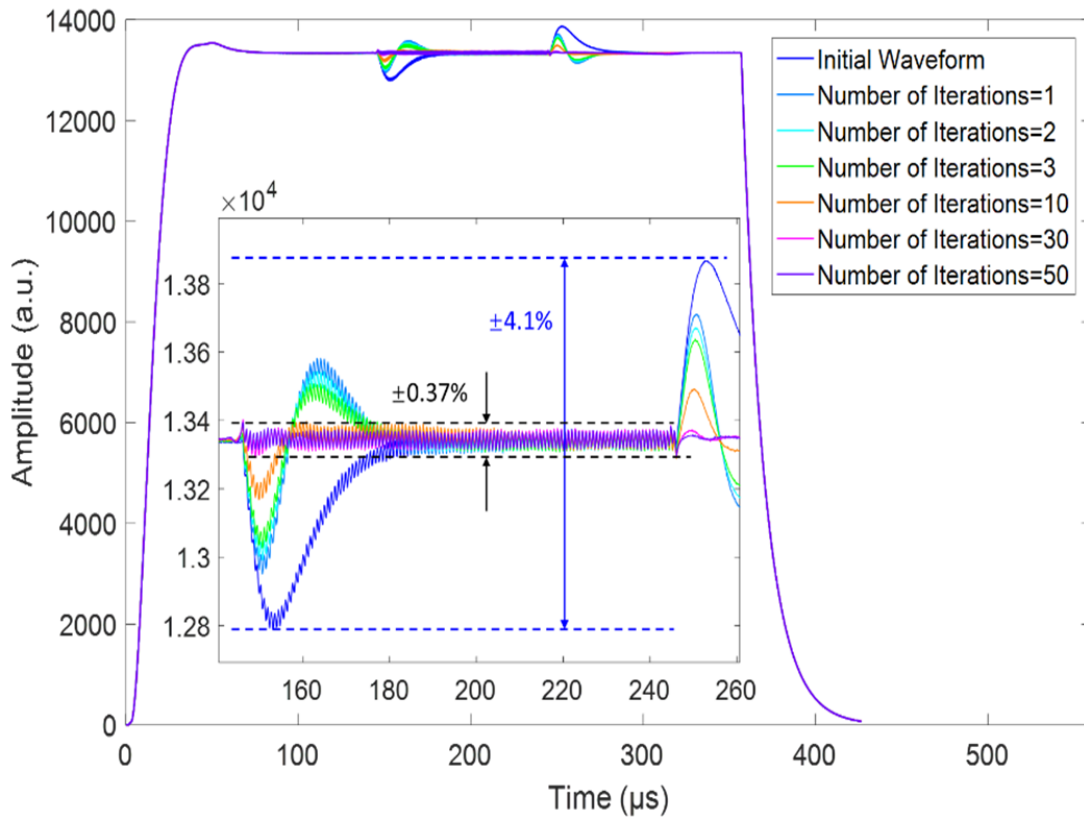


Figure 7.2. ADC amplitude waveforms during 50 iterations.

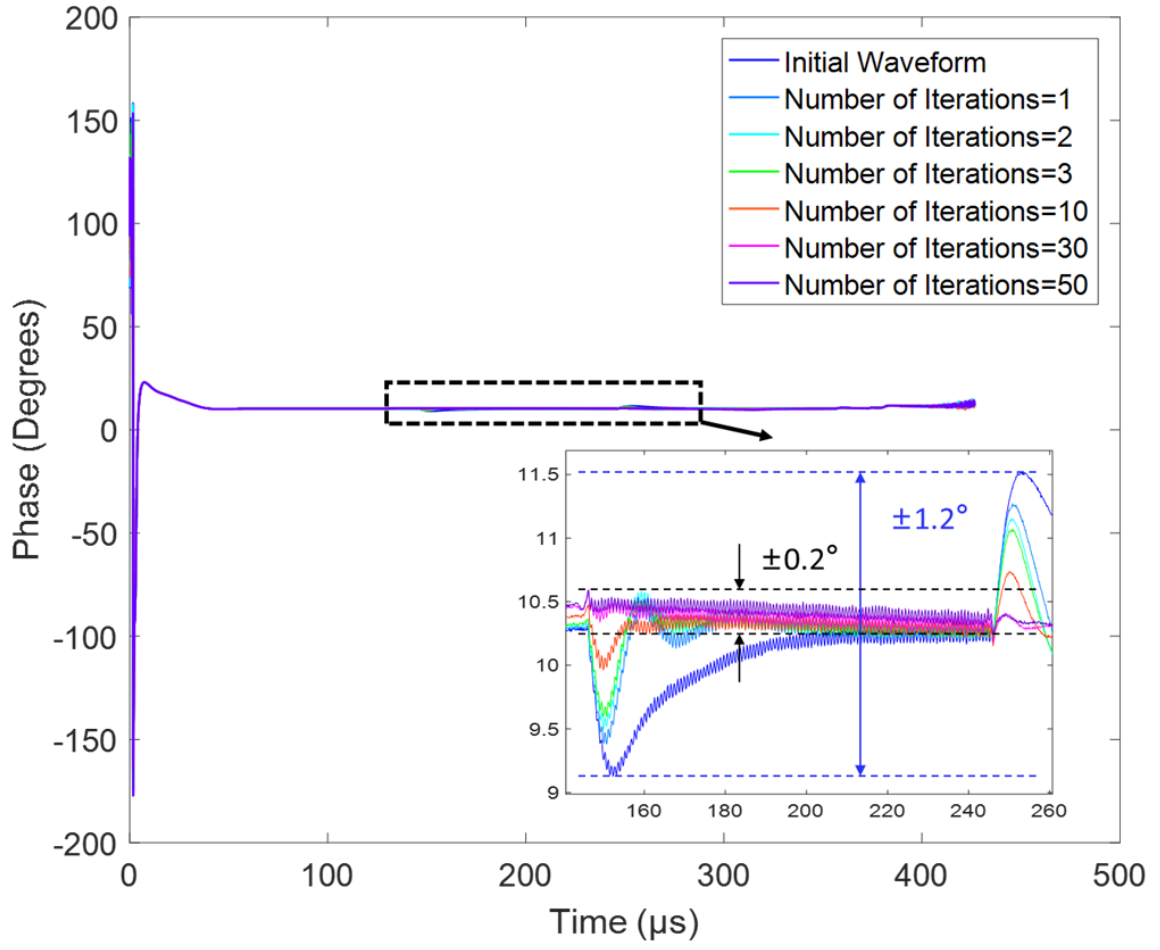


Figure 7.3. ADC phase waveforms during 50 iterations.

Figure 7.3 shows the ADC phase waveform. The experiment condition is the same as figure 7.2. As the number of iterations increasing, the phase peak to peak stability was improved from  $\pm 1.2^\circ$  to  $\pm 0.2^\circ$ . After using the ILC based adaptive feedforward method, both the amplitude and phase peak to peak stability have met the requirements, which is  $\pm 0.5\%$  in amplitude and  $\pm 0.5^\circ$  in phase.



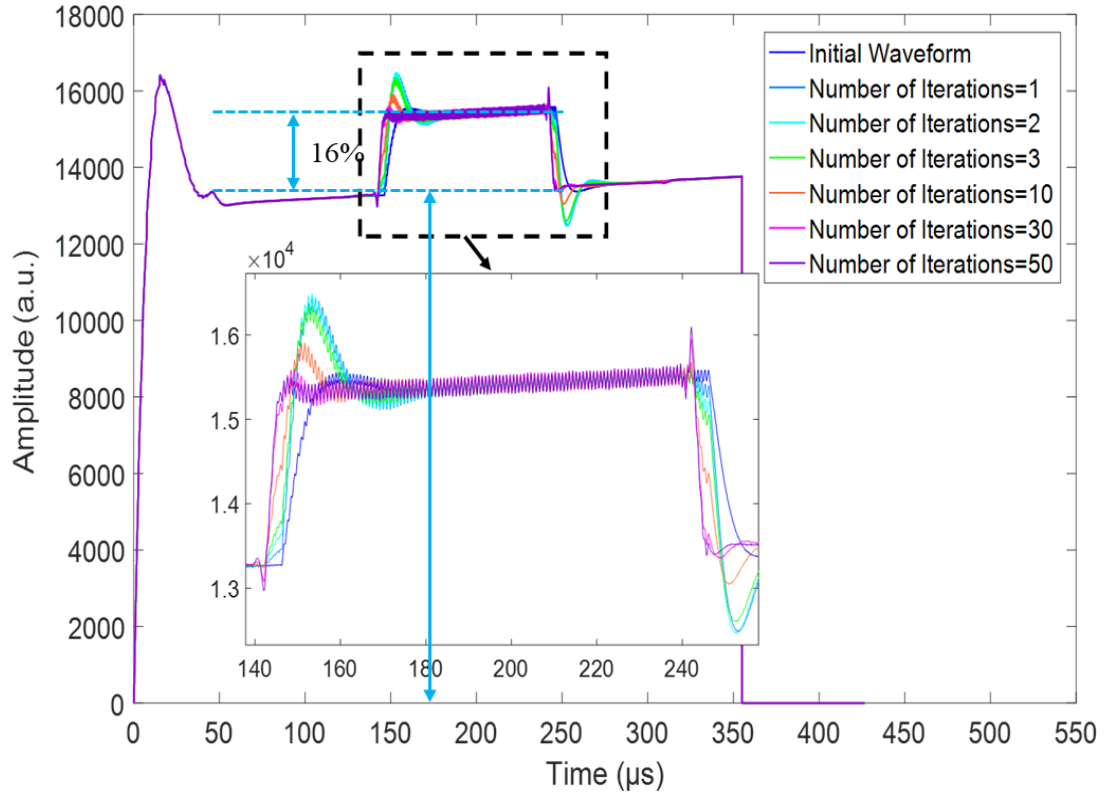


Figure 7.4. DAC amplitude waveforms during 50 iterations.

DAC amplitude waveforms are shown in the Fig 7.4. Compared to the current beam loading compensation in chopper mode, the amplitude ratio of the raised portion and the flat top improved from 45% to 16%. The excessive DAC amplitude may exceed the full-scale value, trigger interlock protection. Results shows that ILC helps to decrease the amplitude ratio of the raised portion and the flat top greatly. After 50 iterations, the transient overshoot around 150  $\mu\text{s}$  is suppressed. With respect to the time axis, owing to the time shift of the error, the raised portion is gradually moved to the left to compensate for the deformation caused by the beam head.

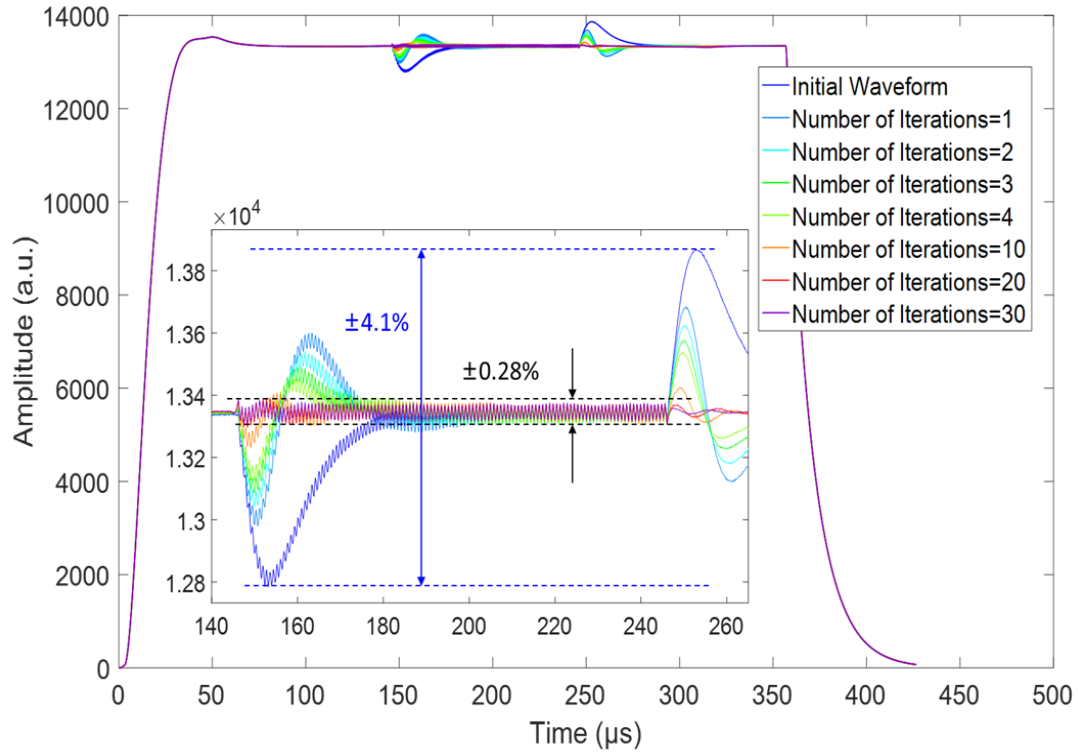


Figure 7.5. ADC amplitude waveforms during 30 iterations.

To get the best system performance in a short time. In the second test, the ILC gain is set to 0.9. The time shift of error is set to  $3.43 \mu\text{s}$ . Alignment of moving average is center. The window of moving average is 3. Average number still choose 8. [Figure 7.5](#) shows the ADC amplitude waveform during 30 iterations under above conditions. This time, the peak to peak stability of amplitude improves from  $\pm 4.1\%$  to  $\pm 0.28\%$ .

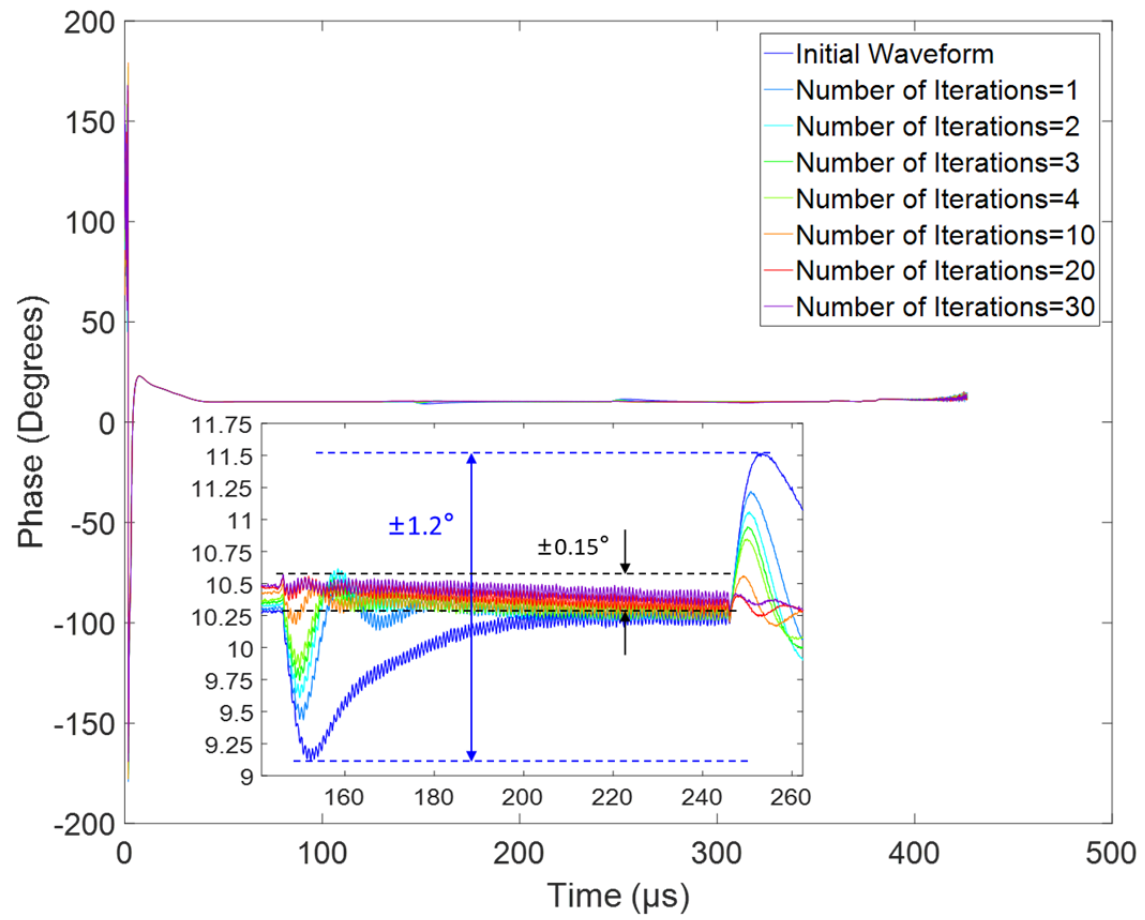


Figure 7.6. ADC phase waveforms during 30 iterations.

Figure 7.6 shows the ADC phase waveforms during 30 iterations which condition is the same as figure 43. Although only 30 iterations were performed, under better time shift of error and larger ILC gain, the peak to peak stability of phase was improved to  $\pm 0.15^\circ$ , which is better than the result  $\pm 0.2^\circ$  in the Fig 7.3.

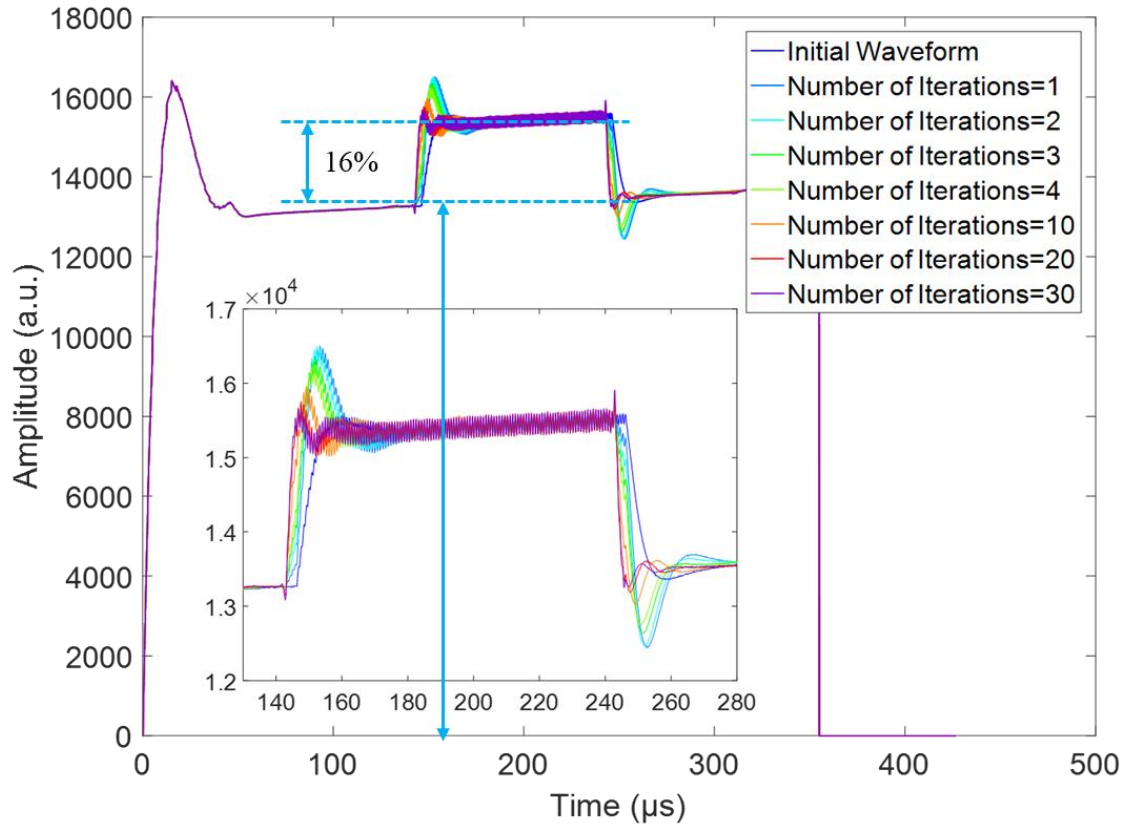
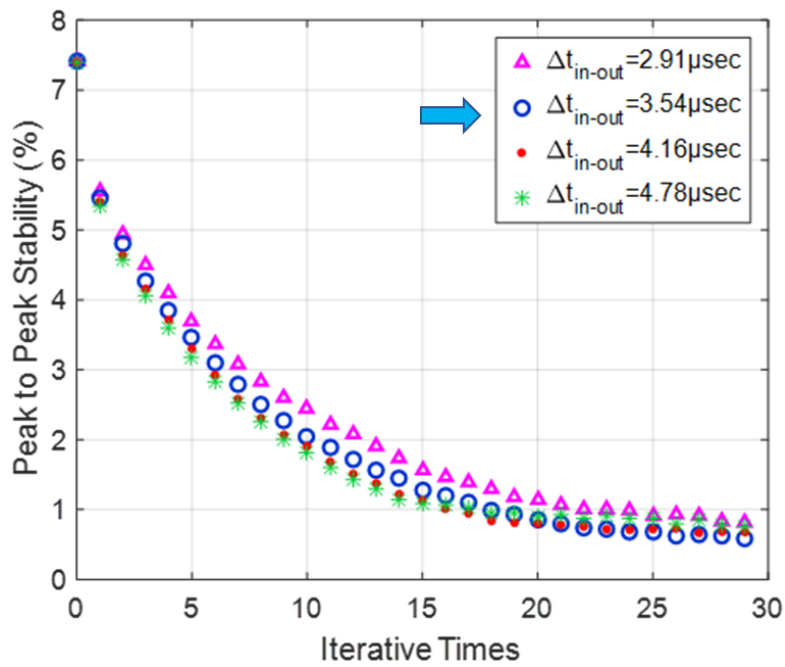


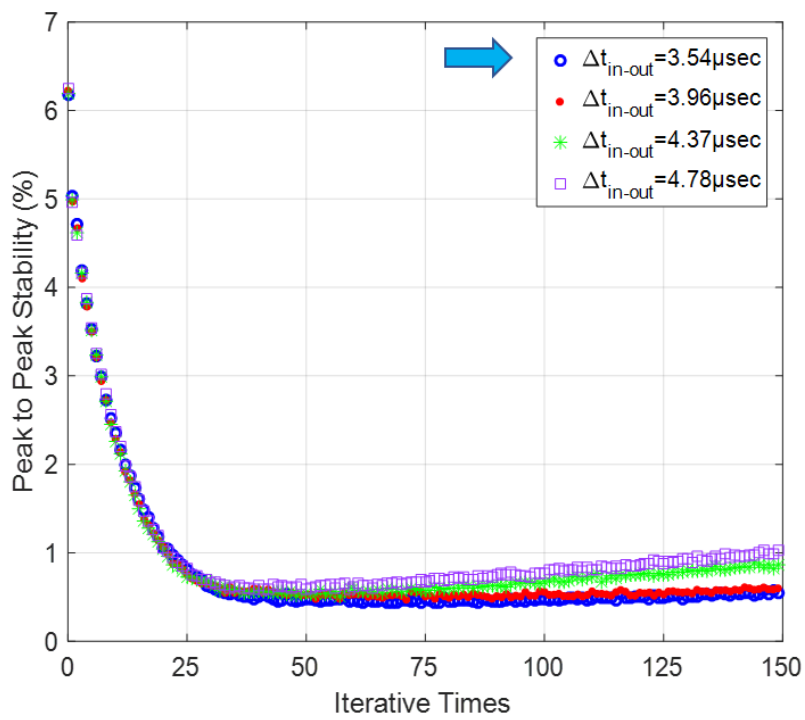
Figure 7.7. DAC amplitude waveforms during 30 iterations.

Figure 7.7 shows the DAC amplitude waveforms during 30 iterations when the ILC gain is set to 0.9 and the time shift of error is set to  $3.43 \mu\text{s}$ . After changing the parameters, the DAC amplitude ratio of the raised portion and the flat top still improved from 45% to 16%, which is the same with the results of Fig. 7.4.

# 7.2 Effect of Time Shift of Error



(a)



(b)

Figure 7.8. Effect of  $\Delta t_{in-out}$  on the experimental results during 29 iterations (a) and 149 iterations (b).

To align the feedforward signal and the deformation of the RF field, it is important to determine a suitable time shift value of the tracking error. Fig. 46 shows the relationship between the peak-to-peak stability of amplitude and number of iterations under different time shifts of the error  $\Delta t_{in-out}$ .

. Zero number of iterations represents the situation where only feedback control exists. When  $\Delta t_{in-out}$  is set to 3.54  $\mu\text{s}$ , the best peak-to-peak stability is obtained, and the time difference between the feedforward signal and the deformation part of the ADC signal is well compensated by adjusting the shift. In the Fig. 7.8 (a), the system performs 29 iterations to complete the beam compensation process. The peak-to-peak stability data from the last few iterations illustrate that when the set value of  $\Delta t_{in-out}$  deviates from the optimum value, which is 3.54  $\mu\text{s}$  here, the peak-to-peak stability begins to deteriorate, regardless of the sign of the difference value. In the Fig. 7.8 (b), 149 iterations were executed. With an increasing number of iterations, the inappropriate set value not only makes the system fail to run at its best performance but also drastically affects the system stability. When the value of  $\Delta t_{in-out}$  is selected to be 4.37  $\mu\text{s}$  and 4.78  $\mu\text{s}$ , two obvious divergence curves can be observed.

### 7.3 Effect of ILC Gain

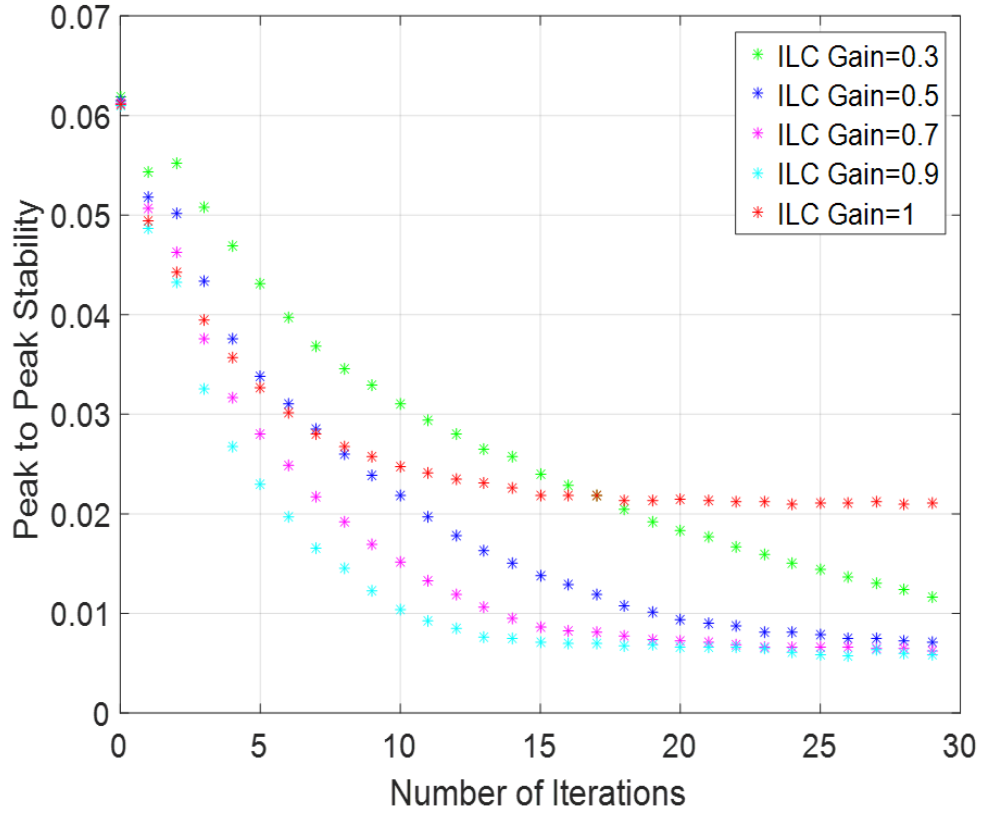
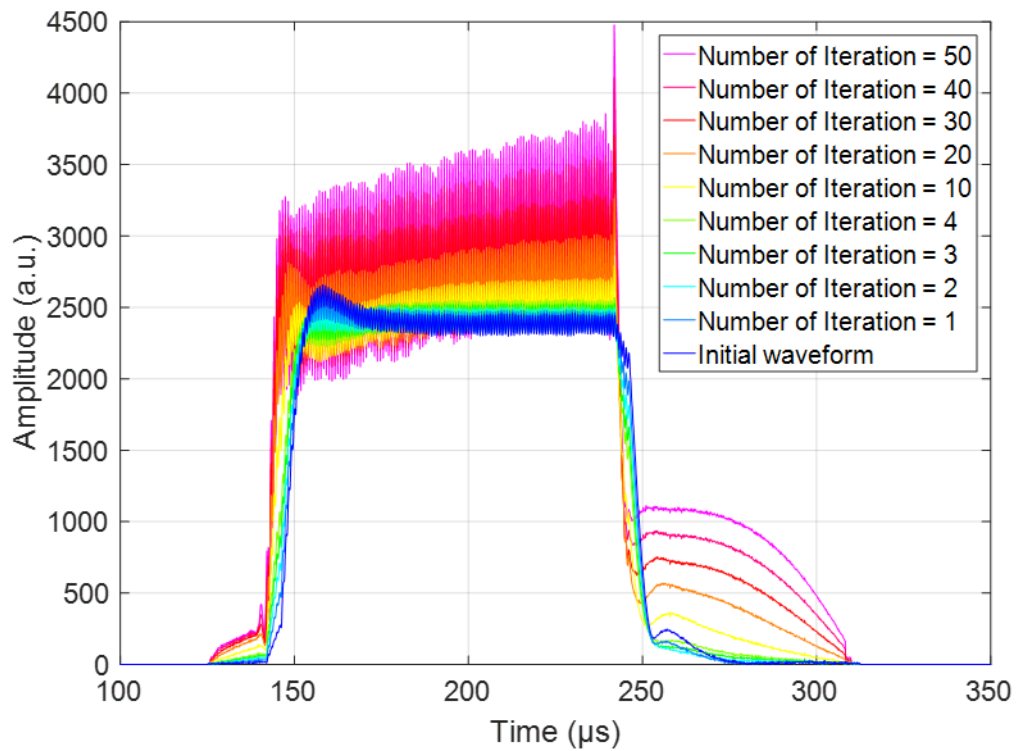


Figure 7.9. Effect of ILC gain to the amplitude peak to peak stability during 30 iterations.

Figure 7.9 shows the effect of ILC gain to the amplitude peak to peak stability during 30 iterations. The experiment results show the similar conclusion of simulation results, namely, larger gain helps ILC complete the iterative convergence process in less time. In the case of ILC gain equals to 1, the peak to peak stability curve still convergence, but the final result is very worse. It shows that 1 is the critical point of ILC gain. When the ILC gain was 0.5, the number of iterations becomes 30. For smaller ILC gains, such as 0.1, it usually takes 100–200 iterations to complete the compensation process. In the J-PARC LINAC, when the repetition rate of the beam is 25 Hz, it takes 0.32 s to complete an iteration; thus, if the ILC gain is set to 0.9, it takes approximately 6.4 s to complete the convergence process. For the case where the ILC gain is 0.5 and 0.1, the corresponding time required to complete convergence is approximately 9.6 s and 32 s, respectively. Compared with static feedforward control, which requires the operator to determine the optimal compensation value manually, adaptive

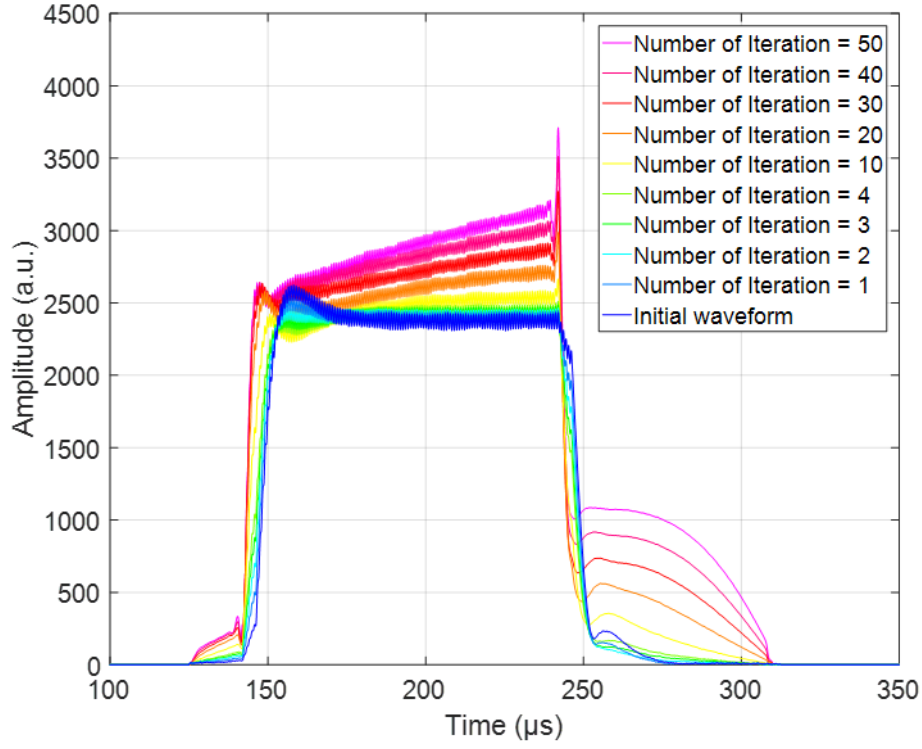
feedforward control can automatically complete the compensation process well in a very short time. For the J-PARC LINAC with dozens of RF stations that require feedforward compensation, the ILC controller helps improve the working efficiency significantly.

## 7.4 Effect of Moving Average



(a)





(b)

Figure 7.10. FF\_BEAM waveforms during 50 iterations without (a) and with (b) moving average filtering.

Figure 7.10 show the effect of moving average to the feedforward waveform (FF\_BEAM). The ILC gain was set to 0.5. The time shift of error is  $4.16 \mu\text{s}$ . Alignment of moving average is center. The window of moving average is 3. Average number still choose 8. In the Fig 7.10 (a), there is no Q-filter (moving average) in the ILC controller, the high frequency noise from the cavity output signals were added to the next feedforward signals. This causes the amplitude of the feedforward signal to be larger and larger due to the continuous accumulation of noise during the iterations. This will have a very bad impact on the stability of the system especially for the long-term operation. In the Fig 7.10 (b), after adding the Q-filter, the high-frequency noise in the feedforward signals were significantly suppressed. In the actual situation, if the ILC is used for long-term operation, then the Q-filter, in our case moving average module, it is a necessary component.

## Chapter 8

# Mathematical Analysis of LLRF System with an ILC Based Feedforward

In this chapter, the mathematical model of the LLRF system with an ILC based feedforward function will be built. The stability and convergence of this system will be discussed.

### 8.1 Mathematical Model of the LLRF System with an ILC based Feedforward Function

The ILC algorithm can be given by

$$u_{j+1}(k) = Q(q)[u_j(k) + L(q)e_j(k+1)] + C(q)e_{j+1}(k) \quad (8.1)$$

where  $k$  is the time index,  $j$  is the iteration index,  $q$  is the forward time-shift operator  $qx(k) \equiv x(k+1)$ ,  $u_j$  is the system input,  $e_j$  is the error,  $C(q)$ ,  $Q(q)$  and  $L(q)$  are defined as the feedback controller,  $Q$ -filter and learning function, respectively. And Eq. (17) can be separated into two components, feedforward and feedback which are the output of ILC controller and feedback controller respectively, so we have

$$u_{j+1}(k) = w_{j+1}(k) + C(q)e_{j+1}(k) \quad (8.2)$$

where feedforward component

$$w_{j+1}(k) = Q(q)[u_j(k) + L(q)e_j(k+1)] \quad (8.3)$$

## 8.2 Stability and Convergence Analysis

In the frequency domain, the ILC learning mechanism is given by

$$U_F^{j+1} = Q(U_F^j + LE^j) \quad (8.4)$$

where  $Q$  and  $L$  denote the Laplace transform of  $Q$  filter and learning function, respectively.  $U_F^j$  is the Laplace transform of the feedforward signal in run  $j$  and  $E^j$  is the Laplace transform of the system tracking error. Learning converges, if the feedback loop stable and the following condition holds.

$$\forall \omega \in \mathbb{R}, \|U_F^{j+2}(j\omega) - U_F^{j+1}(j\omega)\|_\infty < \|U_F^{j+1}(j\omega) - U_F^j(j\omega)\|_\infty \quad (8.5)$$

According to the transfer function of system, the system output can be given by

$$Y^j = \frac{CP}{1+CP} Y^d + \frac{P}{1+CP} U_F^j \quad (8.6)$$

where  $P$  denotes the Laplace transform of the plant,  $Y^j$  is the Laplace transform of the system output in run  $j$  and  $Y^d$  is the Laplace transform of the reference. Then the system error is given by

$$E^j = Y^d - Y^j = Y^d - \frac{CP}{1+CP} Y^d - \frac{P}{1+CP} U_F^j = \frac{1}{1+CP} Y^d - \frac{P}{1+CP} U_F^j \quad (8.7)$$

the left-hand side of Eq. (2.19) can be written as

$$\begin{aligned} \|U_F^{j+2} - U_F^{j+1}\|_\infty &= \|Q(U_F^{j+1} + LE^{j+1}) - Q(U_F^j + LE^j)\|_\infty \\ &= \left\| Q\left(U_F^{j+1} - U_F^j - \frac{LP}{1+CP}(U_F^{j+1} - U_F^j)\right) \right\|_\infty = \left\| Q\left(1 - \frac{LP}{1+CP}\right)(U_F^{j+1} - U_F^j) \right\|_\infty \\ &\leq \left\| Q\left(1 - \frac{LP}{1+CP}\right) \right\|_\infty \|U_F^{j+1} - U_F^j\|_\infty \end{aligned} \quad (8.8)$$

Therefore, learning converges if

$$\left\| Q\left(1 - \frac{LP}{1+CP}\right) \right\|_\infty < 1 \quad (8.9)$$

And the Q-filter is usually a low-pass filter, which means for high-frequency signal  $Q \approx 0$ , but for low-frequency signal  $Q \approx 1$ . Thus, for the low-frequency signal, the learning converges is given by

$$\left\| 1 - \frac{LP}{1+CP} \right\|_{\infty} < 1 \quad (8.10)$$

As we mentioned before, in the first-order P-type ILC, the learning function  $L$  is a proportional constant  $\gamma$ . In order to ensure the stability of the system,  $\gamma$  is often set to the value close to the reciprocal of  $P/1+CP$ .

# Chapter 9

## Conclusion and Future plan

All the work in the dissertation is summarized and the future prospects will be given here.

### 9.1 Conclusion

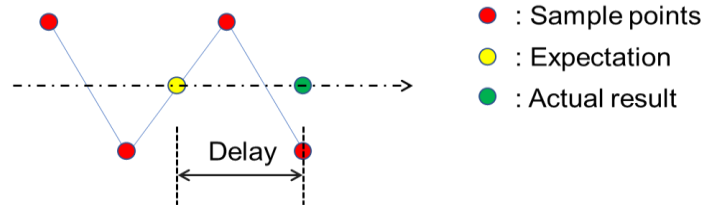
To deal with the heavy beam loading effect, an Iterative Learning Control scheme was studied and successfully implemented in the J-PARC LINAC. Before putting into use, to verify the effectiveness of this method, an ILC simulation model for LLRF control system was built in the Simulink environment. The simulation results show that after using the iterative learning control, the beam loading effect is well suppressed. The simulation model reveals the characteristics of ILC and provides a theoretical basis for subsequent experiments. The ILC controller was implemented with the Python program on a computer. The beam loading compensation experimental results show that, compared to current beam loading control, the inclusion of ILC controller improved the peak to peak stability of amplitude from  $\pm 1\%$  to  $\pm 0.28\%$ , phase from  $\pm 1^\circ$  to  $\pm 0.15^\circ$ , both of them satisfied the requirement of the J-PARC LINAC. In addition, due to ILC can automatically complete the entire compensation process in a short time. For a large accelerator such as the J-PARC LINAC, which has dozens of RF stations that require feedforward compensation, ILC greatly reduces the time consumption and workload, thus improves the work efficiency significantly.

## 9.2 Future Plan

In order to ensure long-term stable operation of ILC controller, the python program will be further optimized and then the test with an increased number of iterations will be performed. In addition, to verify the effectiveness of ILC controller in the 972 MHz high  $\beta$  section, the beam loading compensation test will be conducted in the ACS (Annular Coupled Structure) 01 station in the future.

# Appendix A

## 1. Normal sma



## 2. Mid-value sma

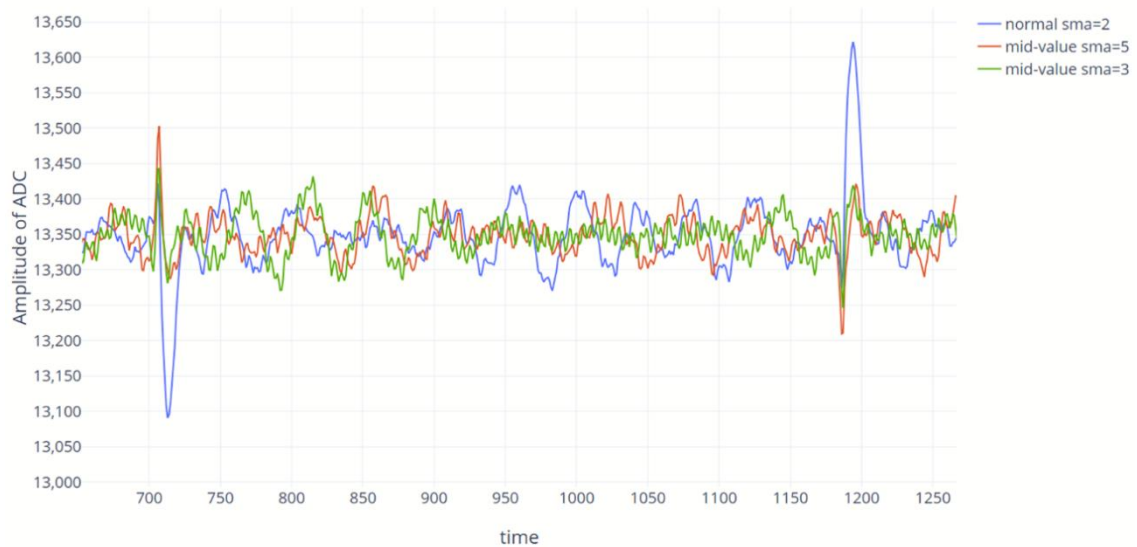
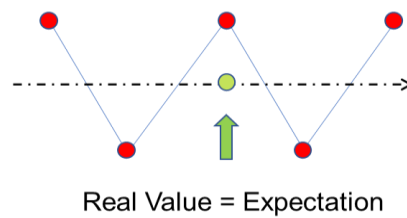


Figure. Effect of simple moving average to the ADC amplitude waveform under different window and alignment.

# Abbreviations

ACS: Annular Coupled Structure  
ADC: Analog to Digital Converter  
AMC: Advanced Mezzanine Card  
BLC: Beam Loading Compensation  
CA: Channel Access  
CW: Continuous Waves  
DAC: Digital to Analog Converter  
DTL: Drift Tube Linacs  
EPICS: Experimental Physics Industry Control System  
ES: Extremum Seeking  
FEL: Free Electron Laser  
FPGA: Field Programming Gate Array  
FX: Fast Extraction  
HD: Hadron Experimental facility  
ILC: Iterative Learning Control  
IOC: Input Output Controller  
IQ: In-phase Quadrature  
J-PARC: Japan Proton Accelerator Complex  
LANSC: Los Alamos Neutron Science Center  
LLRF: Low-Level Radio Frequency  
LINAC: linear accelerator  
MaRIE: Matter Radiation Interactions in Extremes  
MLF: Materials and Life science experimental Facility  
MR: Main Ring  
MTCA: Micro Telecom Communication Architecture  
NOILC: Norm-Optimal Iterative Learning Control  
PLC: Programming Logic Controller  
PV: Process Variable  
RCS: Rapid Cycling Synchrotron  
RMS: Root Mean Square  
RTM: Rear Transition Module  
RF: Radio Frequency  
RFQ: Radio Frequency Quadruple



SDTL: Separated Drift Tube Linacs

SMA: Simple Moving Average

T2K: Tokai-to-Kamioka

# Symbol

$A_w$	The detune frequency
$e_j$	Error at jth iteration
$I$	The driving current
$j$	The iteration index
$k$	The time index
$R_l$	The equivalent resistance of the cavity
$Q_l$	The loaded quality factor
$T_{loop}$	The loop delay of feedback loop
$u_j$	The cavity input at jth iteration
$v_c$	cavity voltage
$v_{cr}$	real part of cavity voltage
$v_{ci}$	Imaginary part of cavity voltage
$w_v$	The resonanc angnlar frequency
$w_j$	The ILC controller output at jth iteration
$w_{y2}$	Half band width
$x_{sma}$	The input of Q filter
$y_{sma}$	The output of Q filter

# List of Figures

Figure 1.1. A layout of J-PARC facilities.

Figure 1.2. Configuration and Main parameter of the J-PARC linac

Figure 1.3. Outline of RF Stations and RF Cavities in 324-MHz low  $\beta$  accelerator section.

Figure 1.4. Outline of RF Stations and RF Cavities in 972-MHz high  $\beta$  accelerator section.

Figure 1.5. ADC amplitude waveform at the flat top in SDTL01 station.

Figure 1.6. ADC phase waveform in SDTL01 station.

Figure 1.7. Two static feedforward compensation modes in the J-PARC LINAC.

Figure 1.8. DAC amplitude waveform in SDTL01 station.

Figure 1.9. Extreme case of amplitude waveform in the SDTL01 station.

Figure 1.10. Extreme case of phase waveform in the SDTL01 station.

Figure 2.1. XFEL accelerator overview.

Figure 2.2. Simplified block diagram of the LLRF system installed at one RF station in European-XFEL.

Figure 2.3 Beam loading compensation and cavity gradient.

Figure 2.4 Block diagram of Beam Loading Compensation module.

Figure 2.5. Cavity gradient with BLC enabled and disabled for beam with 50 bunches with 0.25 nC @1MHz repetition rate.

Figure 2.6. Cavity gradient with BLC enabled and disabled for beam with 300 bunches with 0.25 nC @4.5MHz repetition rate.

Figure 3.1. The block diagram of control system.

Figure 3.2. Block diagram of LLRF control system.

Figure 3.3. Block diagram of new LLRF control system.

Figure 3.4. Prototype system for new J-PARC LINAC LLRF system.

Figure 3.5. Digitizer Board.

Figure 4.1. Overall of ILC scheme for J-PARC LINAC.

Figure 5.1. Block diagram of LLRF system model.

Figure 5.2. The architecture of cavity model.

Figure 5.3. Amplitude & Phase Waveform of the simulation system output with beam loading when feedback is off (a) and on (b).

Figure 5.4. Block diagram of ILC loop.

Figure 5.5. Block diagram of ILC simulation scheme.

Figure 5.6. Effect of time shift of error to the final cavity output waveform.

Figure 5.7. Effect of time shift of error to the results.

Figure 5.8. Effect of ILC gain to the amplitude peak to peak stability.

Figure 5.9. Cavity output amplitude waveforms during 50 iterations.

Figure 5.10. Final cavity output amplitude waveform after 50 iterations.

Figure 5.11. Cavity output phase waveform during 50 iterations.

Figure 5.12. Final cavity output phase waveform after 50 iterations.

Figure 6.1. Architecture of feedback loop and ILC loop.

Figure 6.2. Program flowchart in ILC controller.

Figure 6.3. Schematic diagram of ADC, DAC and DAC\_BASE waveforms under feedback control in J-PARC LINAC.

Figure 6.4. LLRF system setup for beam loading compensation experiment.

Figure 7.1. The time structure of the linac beam pulse.

Figure 7.2. ADC amplitude waveforms during 50 iterations.

Figure 7.3. ADC phase waveforms during 50 iterations.

Figure 7.4. DAC amplitude waveforms during 50 iterations.

Figure 7.5. ADC amplitude waveforms during 30 iterations.

Figure 7.6. ADC phase waveforms during 30 iterations.

Figure 7.7. DAC amplitude waveforms during 30 iterations.

Figure 7.8. Effect of  $\Delta t_{(in-out)}$  on the experimental results during 29 iterations (a) and 149 iterations (b).

Figure 7.9. Effect of ILC gain to the amplitude peak to peak stability during 30 iterations.

Figure 7.10. FF\_BEAM waveforms during 50 iterations without (a) and with (b) moving average filtering.

# List of Tables

Table 1: ES performance during beam turn on transient

Table 2: Control Algorithm F-NOILC

Table 3: Available and required computation time for different levels

# Bibliography

- [1] J-PARC, <http://www.j-parc.jp>
- [2] Z. Fang, K. Futatsukawa, Y. Fukui, T. Kobayashi, S. Michizono, F. Sato, S. Shinozaki, E. Chishiro, Improvements of low level RF control systems for J-PARC LINAC 400-MeV upgrade, in: Proceedings of the 2nd International Symposium on Science at J-PARC, vol. 8, 011001-1-011001-6, September 2015.
- [3] Z. Fang, T. Kobayashi, Y. Fukui, K. Futatsukawa, S. Michizono, S. Yamaguchi, S. Anami, H. Suzuki, F. Sato, S. Shinozaki, E. Chishiro, Auto-tuning systems for J-PARC LINAC RF cavities, Nuclear Instruments and Methods in Physics Research A (NIM. A), 767 (2014) 135-145.
- [4] H. Oguri, Approaches to high power operation of J-PARC accelerator, in: Proceeding of LINAC 2018, China, September 2018, pp. 29-34.
- [5] K. Futatsukawa, Z. Fang, Y. Fukui, S. Shinozaki, Y. Sato, Development of new LLRF system at the J-PARC LINAC, in: Proceeding of LINAC 2018, China, September 2018, pp. 233-235.
- [6] Butkowski L, Branlard J, Omet M, et al. Implementation of the Beam Loading Compensation Algorithm in the LLRF System of the European XFEL, Linear Accelerator Conf.(LINAC'18), Beijing, China, 16-21 September 2018. JACOW Publishing, Geneva, Switzerland, 2018: 594-597.
- [7] Scheinker, Alexander. "Iterative Extremum Seeking for feedforward compensation of beam loading in particle accelerator RF cavities." 2017 American Control Conference (ACC). IEEE, 2017.
- [8] Rogers E, Owens D H, Werner H, et al. Norm optimal iterative learning control with application to problems in accelerator based free electron lasers and rehabilitation robotics[J]. European Journal of Control, 2010, 16(5): 497-524.

- [9] M. Newville, pyepics: EPICS Channel Access for Python, CARS, University of Chicago, 2010-2016, available at <http://cars9.uchicago.edu/software/python/pyepics3/index.html>.
- [10] Ahn H S, Chen Y Q, Moore K L. Iterative learning control: Brief survey and categorization[J]. IEEE Transactions on Systems, Man, and Cybernetics, Part C (Applications and Reviews), 2007, 37(6): 1099-1121.
- [11] D.A. Bristow, M. Tharayil, A.G. Alleyne, A survey of iterative learning control, IEEE Control Systems Magazine, 26 (2006) 96-114.
- [12] Owens D H. NOILC: Natural Extensions[M]//Iterative Learning Control. Springer, London, 2016: 277-321.
- [13] Wangler, Thomas P. RF Linear accelerators. John Wiley & Sons, 2008.
- [14] S. Li, Z. Fang, K. Futatsukawa, et al. Iterative learning control-based adaptive beam loading compensation implementations in the J-PARC LINAC, Nuclear Inst. and Methods in Physics Research, A, vol.945(2019).
- [15] Kato T, Ikegami M, Wang S, et al. Beam Study with RF Choppers in the MEBT of the J-PARC Proton Linac[C]//Proceedings of the 2003 Particle Accelerator Conference. IEEE, 2003, 3: 1455-1457.

# Acknowledgment

I would like to express my gratitude to all those who helped me during the process of writing of this thesis and during my study years.

My deepest gratitude goes first and foremost to Professor Fang Zhigao, my supervisor, for his helpful guidance, valuable suggestions and constant encouragement both in my study and in my life. His relentless pursuit of knowledge, and meticulous attitude towards research manifest the personalities and qualities that I should cultivate as a qualified researcher.

Also, I would like to express my sincere gratitude to Professor Matsumoto and Professor Miura. During these three years, I learned a lot under their guidance and valuable advices that greatly broadened my horizon and enriched my knowledge in my study.

Besides, I want to express my heartfelt thanks to Professor Futatsukawa and Professor Qiu who have provided very constructive guidance to my study at both technical and theoretical levels.

I am particularly grateful to Professor Michizono. Thanks very much for the direction and willing to give me a chance to graduate in time.

And I would like to extend my gratefulness to my colleagues, Shinozaki-san, Sato-san, Mizobata-san, Fukui-san and Hirane-san. I'm very happy to work with them during these years. I would also like to extend my deep gratefulness to my friends, Liu Na, Du Baiting, Xu Xiuqing, Tan Zhijian, Mukesh and Ersin. Thank you very much for your encouragement and help. Because of you, my research career full of colors.

Finally, my thanks would go to my beloved family for their loving consideration and great confidence all through these years. Their love is always the source of my strength.



# Declaration

I declare that I wrote this preliminary Ph.D.-thesis independently and without any other references and resources than those stated in the bibliography.

Tokai, May 2019